POPULATION STATISTICS OF GALAXY CLUSTER HALOS IN COSMOLOGICAL SIMULATIONS

by

Rebecca M. Stanek

A dissertation submitted in partial fulfillment
of the requirements for the degree of
Doctor of Philosophy
(Astronomy and Astrophysics)
in The University of Michigan
2009

Doctoral Committee:

Professor August E. Evrard, Chair
Professor Joel N. Bregman
Professor Timothy A. McKay
Assistant Professor Mateusz Ruszkowski

To my two favorite doctors

ACKNOWLEDGMENTS

This work would not have been possible without the support and guidance of my advisor, Gus Evrard, and the past and current members of my committee: Tim McKay, Joel Bregman, Rebecca Bernstein, and Mateusz Ruszkowski. I'd also like to thank Fred Adams, Elena Rasia, Michael Busha, Brian Nord, and Anbo Chen for their input during research group meetings.

Hans Böhringer and the late Peter Schuecker provided me with the REFLEX survey data before it was public, which was used in Chapter 3. Frazer Pearce and Lorena Gazzola provided me with the raw simulation data for the Millennium Gas Simulations, which was used in Chapters 4 and 5. Doug Rudd provided reduced simulation data for Chapter 5. Most of my data analysis was run on `opus`, which was built and maintained by Michael Busha, and on `legato`, which was built and maintained by LSAIT and Marlin Whitaker.

Chapter 3 was previously published as Stanek et al. (2006), with co-authors August E. Evrard, Hans Böhringer, Peter Schuecker, and Brian Nord. Kerby Shedden gave us valuable input on the handling of the observed flux errors. Chapter 5 was previously published as Stanek et al. (2009), with co-authors Douglas Rudd and August E. Evrard. Daisuke Nagai and Jeremy Tinker gave us insightful comments on the manuscript. I will soon be submitting Chapter 4 to ApJ, with co-authors Elena Rasia, August E. Evrard, Frazer Pearce, and Lorena Gazzola.

I'd like to thank Gus Evrard, Michael Busha, Sarah Ragan, and Eli Rykoff for useful advice on the thesis document as a whole. I formatted the thesis with a LaTeX template that has been floating around the physics department, with the most recent modifications by Eli Rykoff.

On a personal note, I'd like to thank the entire Department of Astronomy for all

the advice, friendship, and beer throughout the years. Finishing remotely would not have been possible without logistical support from Gus Evrard, Sarah Lloyd, Jess Werk, Kayhan Gultekin, Matt Crites, and Sarah Ragan. I would like to thank my friends and family for their unwavering support, especially my parents, Dave and Ginger Stanek, and my two favorite doctors, Eli and Doc.

CONTENTS

LIST OF FIGURES

Figure

LIST OF TABLES

Table

ABSTRACT

The number of massive structures in the universe is determined by a small set of cosmological parameters characterizing its content, geometry, and expansion rate. Survey counts of massive clusters of galaxies can constrain these parameters, but require a statistical model relating total cluster mass to relevant, observable signals, such X-ray luminosity, X-ray temperature, and galaxy count. I present empirical and computational efforts to improve estimates of this statistical relationship, with an emphasis on measures of the hot intracluster gas. First, I present my work calibrating the relationship between galaxy cluster mass and X-ray luminosity. This work compared observed cluster counts from the REFLEX survey to expectations for ΛCDM cosmologies derived from a halo mass function. In this comparison, I obtained the first measurement of the scatter and discuss possible systematic biases in parameter estimates due to the scatter. I extended my work on mass selection functions to a full suite of X-ray and Sunyaev-Zeldovich (SZ) signals in the Millennium Gas Simulations (MGS). The MGS are hydrodynamic simulations in a $500\,h^{-1}$ Mpc box, with two treatments of the gas physics: a model with only shock-heating and gravity (`GO`) and a simple preheating model (`PH`). From the MGS, I present scaling relations among multiple signals, including a covariance matrix, for about ~ 4000 massive halos. Finally, I investigate the total halo mass function with two pairs of simulations: the MGS and a pair of high-resolution simulations which include a `GO` model and a refined treatment including cooling, star formation, and supernova feedback (`CSF`). The `CSF` and `PH` models have baryon fractions which differ from the `GO` models, and therefore systematic shifts in halo mass at fixed number density. These mass shifts result in a $\sim 30\%$ deviation in number density at fixed mass from a halo mass function calibrated with only dark matter, significantly higher than the 5% statistical

uncertainty halo mass function.

CHAPTER 1

Introduction

1.1 Our Place in the Universe

Our understanding of the content of the universe, and our place in it, has changed drastically over the last four hundred years. Until the time of Copernicus and Galileo, philosophers placed the Earth at the center of the universe, which consisted of the solar system and a celestial sphere of stars. From the heliocentric model, Herschel (1785) placed our solar system near the center of the Milky Way galaxy. Only in the 20^{th} century was it determined that there were stellar systems separate from the Milky Way (Crommelin, 1918; Hubble, 1925). Hubble also revolutionized modern astronomy with his discovery that the universe was expanding (Hubble, 1929). In this section I will discuss the expansion of the universe, as well as the matter and energy content of the universe

1.1.1 Expansion of the Universe

The discovery of the expansion of the universe, along with the observation that the universe was isotropic and homogenous on large scales, led to the development of the big bang theory. The big bang theory postulated that the universe began as a hot, dense singularity, and has been cooling and expanding ever since. The big bang theory explained why the recessional velocity of galaxies was proportional to their distance:

$$\vec{v} = H\vec{r} \tag{1.1}$$

where $\vec{r}$ is the distance to the galaxy, $\vec{v}$ is its recessional velocity, and H is Hubble's constant. Alpher et al. (1948) predicted that the hot, dense beginning of the universe

was ideal for the formation of deuterium, helium, and lithium, known as Big Bang Nucleosynthesis (BBN). The big bang theory also predicted that the universe should be filled with background radiation from the big bang, redshifted with the expansion of the universe to the radio waveband. Penzias & Wilson (1965) discovered this cosmic microwave background (CMB) serendipitously, while testing a new radio telescope. This discovery cemented the big bang theory as the prevailing theory for the origin and evolution of the universe.

Following the derivation laid out in many texts, including Peacock (1999), I will now discuss the Friedmann equation, which governs the expansion of the universe within the framework of general relativity. To explain the expansion of the universe, I will use a fixed comoving coordinate r, which is independent of time. This allows us to describe some region of space having a comoving distance of $r = 3$ Mpc as it expands with the universe. Computer simulations of the expansion of the universe are defined by comoving volumes. To get to a physical distance we need to use a scale factor $R(t)$. Hubble's Law can now be redefined as

$$H = \frac{\dot{R}}{R}. \tag{1.2}$$

Hubble's constant at the present day is referred to as H_0, and I will use the common shorthand $h = \frac{H_0}{100 \mathrm{km\,s^{-1}\,Mpc^{-1}}}$. Throughout this thesis I use several values of h. With these definitions in hand, the Friedmann equation is defined as

$$\dot{R}^2 - \frac{8\pi G}{3}\rho R^2 = -kc^2. \tag{1.3}$$

It is important to note that the density term, ρ, denotes the total density of all matter, radiation, and vacuum energy components of the universe. In this equation, k is a dimensionless quantity which denotes the curvature of the universe: $k < 0$ is a negatively curved universe, $k > 0$ a positively curved universe, and $k = 0$ a flat

universe. Cosmologists have defined a "critical density" that yields a flat universe:

$$\rho_c = \frac{3H^2}{8\pi G}, \tag{1.4}$$

where ρ_c includes contributions from the matter, radiation, and vacuum energy. From the critical density, the cosmological density parameters have been defined such that

$$\Omega_m = \frac{\rho_m}{\rho_c}, \tag{1.5}$$

$$\Omega_r = \frac{\rho_r}{\rho_c}, \tag{1.6}$$

and

$$\Omega_\Lambda = \frac{\rho_\Lambda}{\rho_c}. \tag{1.7}$$

In these equations, ρ_m, ρ_r, and ρ_Λ denote the cosmic densities of the matter, radiation, and vacuum energy, respectively. In a flat universe, $\Omega = \Omega_m + \Omega_r + \Omega_\Lambda = 1$. The vacuum energy equation of state is also defined as $w = \frac{p_\Lambda}{\rho_\Lambda}$, where p_Λ is the pressure from the vacuum energy. In the next section I will talk about the progress in determining the values of these cosmological parameters.

1.1.2 Content of the Universe

Zwicky (1937) measured the velocity dispersion of galaxies in the Coma cluster, and noticed that the measured mass from velocity dispersions was greater than the assumed mass from the total stellar content. This work remained a curiosity until Rubin & Ford (1970) measured rotation curves of individual galaxies. As most of the stellar content of a galaxy is near the center, the rotation speed of a galaxy was expected to decrease at higher radii. Instead, Rubin & Ford (1970) found that galaxies had flat rotation curves: there must be some mass in galaxies that does not emit radiation of any sort. This matter was termed "dark matter".

There are several strong indications that dark matter is not baryonic in nature. Current observations of galaxy clusters indicate that only about $\sim 15\%$ of the matter in the universe is baryonic, and the rest is dark matter. This is supported by mea-

surements of deuterium in the universe, which is highly sensitive to the early ratio of baryons to photons (Pettini et al., 2008). Few properties of dark matter are known, although lensing measurements of merging clusters have shown that it is dynamically collisionless (Clowe et al., 2006). The dark matter must be non-relativistic to drive hierarchical structure formation, so Cold Dark Matter (CDM) is the term used to describe successful models of the universe which include dark matter.

While a value of $\Omega = 1$ is aesthetically pleasing, observations of galaxy clusters have established that $\Omega_m < 1$ (White et al., 1993; Carlberg et al., 1997; Donahue et al., 1998; Bahcall et al., 2000). Furthermore, large scale structures in simulations of a universe with $\Omega_m = 1$ do not match the observed universe (Evrard et al., 2002). Meanwhile, observations of the CMB indicate that the geometry of the universe is flat, requiring $\Omega = 1$ (Smoot et al., 1992; Lange et al., 2001). Efstathiou et al. (1990) suggested a non-zero value of Ω_Λ, such that $\Omega = \Omega_m + \Omega_\Lambda = 1$. A non-zero value of the vacuum energy density of the universe, ρ_Λ, leads to an acceleration of the expansion of the universe. Observations of distant supernovae by Riess et al. (1998) confirmed the acceleration of the expansion of the universe. A significantly non-zero value of Ω_Λ agrees with recent observations of galaxy cluster counts (Eisenstein et al., 2005; Cole et al., 2005) and the CMB (Spergel et al., 2006). The source of ρ_Λ is currently unknown, and referred to as "dark energy". Cosmological models which include dark energy are commonly referred to as ΛCDM models. Finally, simulations of the universe which include a cosmological constant match the observed large scale structure of the universe quite well (Evrard et al., 2002; Springel et al., 2005). In the next section I discuss in more detail the contributions of galaxy cluster observations to cosmology.

1.2 Galaxy Clusters

Galaxy clusters are the largest gravitationally-bound objects in the universe. Although first detected in the optical band, galaxies make up only a small fraction of the cluster mass. Approximately 85% of the cluster mass is dark matter, and 15% of the cluster mass is hot gas. In massive clusters, most of the baryons are in the

form of ionizied gas at temperatures above 10^7 K. At these temperatures, the spatially extended emission from the gas is dominated by *bremsstralung* emission, which is observable in X-rays. Galaxy clusters have been detected in the X-ray out to a redshift of $z \sim 1.45$ (Stanford et al., 2006). Galaxies in clusters are observable in the optical band out to a redshift of at least $z \sim 1.46$ (Hilton et al., 2009), and are also useful tracers of dark matter halos. Kaiser (1986) used dimensional arguments and the assumption of self-similarity to analytically predict the simple scaling of X-ray luminosity and temperature with mass. Although the observed relations differ from the self-similar predictions, these X-ray properties of clusters do scale as power laws with mass (Reiprich & Böhringer, 2002). Signals in other bands, such as the Sunyaev-Zeldovich (SZ) effect, measured in the sub-mm, and the number of galaxies brighter than some characteristic brightness, measured in the optical, also scale with total cluster mass as power laws (Bonamente et al., 2008; Johnston et al., 2007; Sheldon et al., 2007, e.g.).

Dark matter-only N-body simulations predict the distribution of matter in the universe to high precision for a given set of cosmological parameters (Evrard et al., 2002; Springel et al., 2005). Simulations including dark matter and gas hydrodynamics have probed a wide range of mass scales in the universe. The dark matter density profiles in different simulations agree to 5% (Heitmann et al., 2005), and the velocity dispersion of dark matter particles agrees very well among a wide range of simulations (Evrard et al., 2008). The gas properties from adiabatic simulations vary to a higher degree; they depend on the resolution and the choice of an Eulerian or Lagrangian treatment of the gas (Frenk et al., 1999; Kravtsov et al., 2005). Adiabatic simulations do not reproduce the observed scaling relations of bulk cluster properties, particularly the scaling of luminosity with mass (Arnaud & Evrard, 1999). Modeling more astrophysical processes in the gas simulations improves the agreement with observations, as I will discuss in Chapters 4 and 5. However, there is still significant variation in bulk properties between simulations. The addition of gas physics affects the distribution of the gas, and thus has a small affect on the potential well felt by the dark matter. Rudd et al. (2008) show how the gas physics affects the total mass

power spectrum measured in a cosmological volume. As cosmology with cluster surveys requires a good knowledge of the theoretically predicted mass function, in the era of "precision cosmology", we must understand these biases to the order of a few percent.

1.2.1 Cluster Observations

X-ray Observations

Once extended X-ray sources were detected from galaxy clusters, Cavaliere & Fusco-Femiano (1976) confirmed that Bremsstrahlung emission from the ICM produced an isothermal gas distribution. Reiprich & Böhringer (2002) calculated total cluster masses from X-ray observations by assuming hydrostatic equilibrum (HSE) and spherical symmetry, using a β-model (Gorenstein et al., 1978) to fit the cluster X-ray surface brightness profile. Simulations by Rasia et al. (2006) show that nonthermal pressure support in clusters – even if they have a "relaxed" appearance – results in a systematic underestimate of cluster masses with the HSE method, particularly when using a β-model.

The Sunyaev-Zeldovich Effect

Sunyaev & Zeldovich (1970) initially discussed the source of small-scale perturbations in the cosmological microwave background (CMB) from free electrons along the line of sight. After the first X-ray detections from the Coma cluster, Sunyaev & Zeldovich (1972) derived the Thermal Sunyaev-Zeldovich Effect (SZE). The thermal SZE is the measured shift in the background radiation temperature due to inverse-Compton scattering of background photons by free electrons in the hot intracluster gas. The thermal SZE depends on only three bulk cluster properties, the temperature, the electron number density, and the integrated pressure: $\frac{\Delta T_{\rm CMB}}{T_{\rm CMB}} \propto \int n_e T_e dl$.

Including relativistic effects and the frequency dependence of the SZE, the full spectral distortion of the CMB due to the SZE is

$$\frac{\Delta T_{\rm SZE}}{T_{\rm CMB}} = f(x) \int n_e \frac{k_B T_e}{m_e c^2} \sigma_T dl \tag{1.8}$$

where the frequency dependence is

$$f(x) = \left(x \frac{e^x + 1}{x^x - 1} - 4 \right) (1 + \delta_{\rm SZE}(x, T_e)). \tag{1.9}$$

This frequency dependence is a function of a frequency term $x = \frac{h\nu}{k_B T_{\rm CMB}}$, and the relativistic correction is included in the $\delta_{\rm SZE}(X, T_E)$ term.

For a cluster with some electron number density n_e and temperature T_e, the spectral shift of the CMB due to the SZE, $\frac{\Delta T_{\rm SZE}}{T_{\rm CMB}}$ does not depend on redshift. The total integrated signal over the solid angle of the cluster, sometimes noted as Y, is related to cluster properties as

$$Y \propto \frac{N_e \langle T_e \rangle}{d_A^2} \propto \frac{M \langle T_e \rangle}{d_A^2}, \tag{1.10}$$

where d_A is the angular diameter distance to the cluster, N_e is the electron column density, and M is the cluster mass. (Carlstrom et al., 2002). As the angular diameter distance $d_A(z)$ is fairly flat above redshift $z \sim 1$, the total integrated SZE signal Y mostly depends on mass. This makes the SZE ideal for determining cosmological parameters from cluster surveys, as at some fixed detection limit a survey can probe a fixed mass limit to a high redshift.

1.2.2 Galaxy Cluster Surveys

Astronomical sky surveys have been popular since the earliest days of the science. Surveys provide a methodology for cataloging stars, nebulae, galaxies, and other astronomical objects, as well as monitoring variable objects. While the entire sky has been surveyed in every waveband, from gamma rays to radio waves, each individual survey must strike a balance between depth and sky coverage. In this section I discuss how galaxy cluster surveys are used for cosmology, and point out recent contributions from surveys with optical, X-ray, and SZE measurements.

Cosmology with Cluster Surveys

Cosmological parameters determine the current cluster mass function of the universe. The high mass end of the cluster mass function is particularly sensitive to the cosmological parameters, leading to the design of many surveys of galaxy clusters. The power spectrum of the universe can be measured, and the normalization scale commonly used is σ_8, the variance of matter density within a sphere of $8\,h^{-1}$ Mpc. As the matter density of the universe, Ω_m, and σ_8 are degenerate when only counting clusters, constraints from supernovae observations and the cosmic microwave background (CMB) must be included when determining the best set of cosmological parameters (Evrard et al., 2002). Determining the cosmological parameters from the observations requires calculating the volume of the survey given the sky area ($d\Omega$) and depth (Peebles, 1996). The depth of a survey in redshift depends on the selection criteria, including the flux limit of the survey. Given a flux lumit, the mass-signal relationship, including the scatter, must be known to get the mass selection function of the survey. I discuss this in the context of X-ray surveys in Chapter 3. Finally, calculating cosmological parameters from cluster surveys requires a well-calibrated theoretical total halo mass function. In Section 1.4, I discuss the agreement among dark matter simulations, and in Chapter 5, the potential systematic bias in the calculated halo mass function due to baryonic physics.

Optical Surveys

A mere 10 years after nebulae were verified as extragalactic objects (Hubble, 1929), Zwicky (1937) noticed that galaxies were clustered on large scales. Shapley (1933) produced a list of 25 known galaxy groups. Abell (1958) produced the first large catalog of galaxy clusters, with over two thousand clusters discovered in a sky survey covering the sky from declinations $-27°$ to $+90°$. To limit the effects of projection, Abell (1958) included strict richness and size criteria in his selection function. After applying the strict criteria – fifty galaxies within two magnitudes of the third brightest member, within a radial distance of 1 Mpc – the catalog included 1682 clusters in the statistical sample.

The Sloan Digital Sky Survey (SDSS) has provided an unprecedented amount of astronomical optical data, surveying a sky area of π sr in five optical bands to a limit of $\sim$ 23 mag (York et al., 2000), with spectroscopic follow-up of about 10^6 bright objects. The data from SDSS has been used to study the universe at all scales, from the structure of the Milky Way (Jurić et al., 2008), to high-redshift $z \sim 6$ quasars (Fan et al., 2006). I will focus on the contributions of SDSS to cluster cosmology. Koester et al. (2007a) created a catalog of over 13,000 clusters from the SDSS using a red-sequence cluster finder known as maxBCG (Koester et al., 2007b). At the bright end of the galaxy luminosity function for cluster members, most galaxies are in a narrow region of color-magnitude space that is characterized by bright, red, early-type galaxies. These galaxies are known as E/S0 ridgeline galaxies, based on their color, or as red-sequence galaxies. The maxBCG method builds clusters from a likely brightest central galaxy (BCG) using these red sequence properties. In the volume-limited redshift range $0.1 < z < 0.3$, Koester et al. (2007a) found over 13,000 clusters with at least ten bright members. This corresponds to a minimum mass of about $> 2 \times 10^{14}\, h^{-1} M_{\odot}$.

The maxBCG cluster catalog has many astrophysical and cosmological applications, and Rozo et al. (2009) has provided cosmological constraints with the catalog.

X-ray Surveys

The *ROSAT* All-Sky Survey (RASS) used the good spatial resolution of the *ROSAT* satellite to perform the first all-sky survey in the X-ray band (Trümper, 1984). RASS detected hundreds of galaxy clusters, providing fresh data on clusters which had been studied in the optical (Ebeling et al., 1993; Pierre et al., 1994). The *ROSAT* ESO Flux-Limited X-ray Survey (REFLEX) branched off of the RASS. Using *ROSAT*, it covered 4.24 *str* of the sky to a flux limit of $f > 3 \times 10^{-12} \mathrm{ergs}^{-1}\mathrm{cm}^{-2}$. REFLEX identified 447 clusters which had optical counterparts in the COSMOS survey (Böhringer et al., 2001). ESO was used for spectroscopic follow-up for redshift determination. The redshift range of the survey extended to $z \sim 0.5$, although most of the clusters were within $z = 0.3$ (Böhringer et al., 2001). Schuecker et al. (2003) combined

cluster counts from the REFLEX survey with clustering of large scale structure to break the $\Omega_m - \sigma_8$ degeneracy. Assuming a flat geometry and no evolution, Schuecker et al. (2003) found $\Omega_m = 0.341^{+0.087}_{-0.071}$ and $\sigma_8 = 0.711^{+0.120}_{-0.162}$. These values are significantly different from those found by WMAP (Spergel et al., 2006). Schuecker et al. (2003) consider several systematic effects biasing the results, including scatter in the mass-luminosity relationship, which I address in Chapter 3.

The Chandra Cluster Cosmology Project (CCCP) is a sample of 37 clusters with a mean redshift of $z = 0.55$, detected by *ROSAT* and followed-up with Chandra (Vikhlinin et al., 2008). The high-redshift clusters in the sample have been selected to have a temperature $T > 5$ keV. For measuring cosmological parameters, the sample also includes 49 nearby clusters, with a mean redshift of $z = 0.05$, detected by RASS (Vikhlinin et al., 2009). By sampling these two redshifts, studying the redshift evolution of the cluster mass function can provide constraints on cosmological parameters. From the CCCP, cluster counts alone constrain the dark energy parameter to $w = -1.14 \pm 0.21$, which is consistent with other observations. Combining cluster counts with data from supernovae and the CMB results in a measure of $w = -0.991 \pm 0.045$ (Vikhlinin et al., 2009).

Romer et al. (2001) proposed a serendipitous X-ray survey using data from the XMM satellite over the course of the 10 year lifetime of XMM. The 10 year projection for sky coverage is $800\,\mathrm{deg}^2$, which is significant, especially considering the sensitivity of XMM. Assuming a flat universe, Sahlén et al. (2008) project constraining Ω_m and σ_8 at the $\sim 10\%$ level.

SZE Surveys

As the integrated signal measured by the SZE is only weakly dependent on redshift, the SZE is an excellent candidate for detecting galaxy clusters to high redshift in cluster surveys (Battye & Weller, 2003a).

The next decade should be an exciting one for SZE surveys. Ground-based SZE surveys require a high altitude, as the atmosphere is not fully transparent to radio waves in the 100 to 300 GHz range, where the integrated SZE signal is strongest.

The Atacama Pathfinder EXperiment (APEX-SZ) (Schwan et al., 2003), a bolometer array, will survey up to 200 square degrees, detecting up to 500 clusters beyond redshift $z > 1$. The Atacama plateau, at elevation 16,500 ft, is ideal for the wavebands of 150 and 217 GHz used by APEX-SZ, due to the high altitude and dry conditions (Schwan et al., 2003). The Atacama Cosmology Telescope (ACT) (Kosowsky, 2003) is another bolometer array at the Atacama plateau. Observing at 145 GHz, 255 GHz, and 265 GHz, ACT should detect about a thousand clusters over a mass limit of $3 \times 10^{14} M_{\odot}$ with 90% completeness in the survey field of 100 square degrees (Sehgal et al., 2007), given a value of $\sigma_8 = 0.9$. As the value of σ_8 is likely much lower (Spergel et al., 2006), these predicted counts are likely optimistic.

The South Pole has long been an excellent location for CMB studies (Lange et al., 1995), and the South Pole Telescope (SPT) (Ruhl et al., 2004) is the latest bolometer array at the NSF South Pole research station site. Although it will measure all sources of small-scale CMB anisotropy, its first mission is a 4000-square degree SZE survey, with narrow bands at 95, 150, 220, 270, and 350 GHz. On the satellite site, the soon-to-be-launched Planck satellite will image the full sky to a sensitivity of $\Delta T/T \sim 2 \times 10^{-6}$, covering a broad frequency range of 25-1000 GHz (Tauber, 2004). Depending on cosmology, Planck will detect up to $\sim 10^4$ clusters out to a redshift of $z \sim 1$ (Bartlett et al., 2008) Furthermore, Planck will be able to detect low-mass (less than $\sim 10^{14} h^{-1} M_{\odot}$) in the local universe, $z < 0.1$ (Malte Schäfer & Bartelmann, 2007).

1.3 Galaxy Cluster Simulations

A system of two particles can be solved analytically, and a system of three particles can be solved analytically in a few specific cases. Systems with more than three particles must be solved numerically. Numerically, in an N-body simulation, the gravitational force on each particle due to every other particle is calculated. Given this force, and thus the acceleration, the equations of motion are then integrated to find the new position of each particle. If each of these forces is calculated individually, the computing time for the simulation is $\sim O(N^2)$. As the number of particles

per simulation grew, more efficient algorithms for approximating the gravitational forces from distant particles were developed. Since the first numerical simulations, the number of particles in simulations has increased exponentially, roughly following Moore's Law, currently maxing out at 10^{10} particles in the Millennium Simulation (Springel et al., 2005). In this section I discuss the history and methodology of N-body simulations, paying particular attention to the inclusion of gas dynamics and simulations of cosmological volumes.

1.3.1 N-Body Simulations

History of N-Body Simulations

The first true N-body simulation was performed by Holmberg (1941), who used a set of 37 lightbulbs and 37 photoreceptors to investigate galaxy-galaxy encounters in two dimensions. As flux and the force of gravity both drop off with distance as $\sim 1/r^2$, lightbulbs were ideal for mimicking gravitational effects. Even with only $N = 74$, Holmberg (1941) measured the tidal tails produced during a galaxy-galaxy encounter. Peebles (1970) used $N = 300$ particles for studying the collapse of a galaxy cluster, such as the Coma cluster.

N-Body Algorithms

The first N-body simulations, including Peebles (1970), calculated the total gravitational force on each particle via direct summation of all the individual forces. As particle number increased past $N \sim 1000$, this quickly became unfeasible, even with faster computer processors. While investigating the galaxy correlation function, Efstathiou & Eastwood (1981) introduced a Particle Particle/Particle Mesh (P^3M) algorithm for calculating gravitational forces. In the P^3M scheme, a fixed lattice is constructed in the computational volume, with a mass assigned to each mesh point. The fixed lattice, and thus fixed spatial density, makes the P^3M method an example of an Eulerian algorithm. The mesh potential is then quickly calculated in Fourier space for distant particles. Within some radius, however, the gravitational forces on a particle are calculated via direct summation. The total force due to neighboring par-

ticles can change in a very short time period, but the mesh contribution to the force is only slowly varying. For N particles, the computational time is $\sim O(N \log N)$. This approach allowed Efstathiou & Eastwood (1981) to use up to 20,000 particles when investigating large scale structure. Introduction of an adaptive mesh at small scales improved the performance for heavily clustered regions (Couchman, 1991).

Barnes & Hut (1986) introduced a tree structure for calculating forces in N-body simulations. With a hierarchical tree structure, at each timestep the simulation volume is recursively divided into cells and subcells until each cubical subcell has only one particle. The computational time to construct the tree scales as $O(N \log N)$. When calculating the gravitational force, the nearby cells are resolved into their subcells, effectively calculating the force via direct summation. The contribution from distant cells is based on the mass and center-of-mass of their total contents. The force calculation at each time step also scales as $O(N \log N)$, resulting in the total computational time scaling as $O(N \log N)$. This is known as a Lagrangian approach, as the resolution of the simulation is set by mass, rather than a fixed spatial grid. The Lagrangian approach of the hierarchical tree algorithm makes it insensitive to underlying properties of the simulation, such as the degree of clustering of particles (Warren et al., 1992). Furthermore, a Lagrangian approach is best for a simulation with a wide dynamic range, including simulations of cosmological expansion (Springel, 2005a). Warren et al. (1992) improved the performance of the treecode by introducing variable timesteps. Variable timesteps permit shorter integration times in dense regions, such as cluster cores, and thus a smaller gravitational softening length can be used in dense regions (Warren et al., 1992).

Xu (1995) developed a Tree Particle Mesh (TPM) algorithm that combines the strengths of the P^3M and tree algorithms. The long range forces are calculated with a particle mesh, but the short range forces with a tree algorithm. This reduces the inherent inefficiency of P^3M algorithms in heavily clustered regions. The TPM is used in most dark matter simulations today, including the Millennium Simulation (Springel, 2005a).

In addition to improvements in the algorithms, advances in computer architecture

improved the efficiency of computer simulations. Vectorization improved tree code performance by a factor of $3-5$ (Hernquist, 1987; Suginohara et al., 1991). The tree code is also efficiently parallelized: Warren et al. (1992) found only a 15% overhead from the parallelization. As tree codes can identify many regions in the simulation which are isolated from each other, Xu (1995) found that assigning each tree to a different processor is efficient until the number of processors exceeds the number of trees. The scaling breaks down at that point, due to the difficulty in splitting one tree over multiple processors. The mesh in a P^3M code is also easily distributed among processors (Xu, 1995).

Consistency Between N-Body Algorithms

Today there is good agreement between different N-Body algorithms for a range of astrophysical problems. Heitmann et al. (2005) compared the performance of several algorithms for the following three problems: a Zeldovich pancake, the structure of an individual galaxy cluster, and the large scale structure statistics from a cosmological volume. Particle mesh codes reproduced the Zeldovich pancakes better than the other algorithms, but there was excellent agreement for the other situations. When looking at only dark matter, Heitmann et al. (2005) found a better agreement in a cluster density profile than in Frenk et al. (1999), which compared cluster density profiles in hydrodynamic simulations. Notably, the algorithms agreed at the percent level on the radius r_{200} of the simulated cluster. Other structural properties of individual halos and ensembles of halos agree between simulations. Evrard et al. (2008) found that the virial relation of dark matter halos agreed between simulations at the 1% level, for halos with a mass $M > 10^{14}\, h^{-1}\, \mathrm{M}_\odot$ and with $N > 1000$ particles.

When simulating a large volume, Heitmann et al. (2005) found excellent agreement in the power spectrum and in halo statistics between the simulations. This result was confirmed by Tinker et al. (2008), who found a 5% agreement in the halo mass function between a range of cosmological simulations. However, further refinements may be necessary if future galaxy cluster lensing surveys measure the mass function at the 1% level (Huterer & Takada, 2005). With calibration of the dark matter halo

function at the 5% level, the systematic effect of baryons must be considered, as I discuss in Chapter 5.

1.3.2 Gas Dynamic Simulations

Unlike simulations of dark matter, which only need to solve Poisson's equation, hydrodynamic simulations must solve the set of hydrodynamic equations. The two most common algorithms for the treatment of gas in computer simulations are known as Smoothed Particle Hydrodynamics (SPH) and Adaptive Mesh Refinement (AMR). SPH is a Lagrangian treatment of the gas particles, originally invented to investigate non-axisymmetric events in stars (Gingold & Monaghan, 1977). Although the SPH algorithm has discrete particles, fluid quantities are described by a kernel that has been smoothed over some number of particles (Monaghan, 1992). As a result, each particle is sampling the local fluid properties. The smoothing length varies per particle, and is often chosen so that each kernel has the same number of particles, or, in the case of Gadget-2, so that each kernel has the same mass given the local density of the gas (Springel, 2005a). The smoothing kernel results in a variable spatial resolution, but a fixed mass resolution. As in dark matter simulations, the Lagrangian approach of SPH makes it ideal for simulations with a large dynamic range, such as simulations of cosmological volumes.

AMR algorithms for gas dynamics branched off of Eulerian treatments of dark matter particles, which used a fixed grid with several levels of spatial resolution (Kravtsov et al., 1997). Truelove et al. (1998) presented an AMR algorithm for gas dynamics for studying star formation. The hydrodynamic equations are solved at the grid points, for several levels of grid coarseness. An adaptive grid can reach very high levels of spatial resolution, particularly in regions with a low mass density. This is an advantage over the SPH simulations, which by nature have poor spatial resolution in regions of low mass density. This leads to better resolution of shocks in AMR simulations than in the SPH simulations (Truelove et al., 1998; Springel, 2005a). In general, AMR and other Eulerian treatments of the gas are ideal if the local gas density is changing rapidly (Tasker et al., 2008).

The agreement between SPH and AMR algorithms is not as good as that between various N-body algorithms for dark matter simulations. In what is known as the Santa Barbara cluster, several codes were used to study halo structure and the X-ray properties of a single cluster (Frenk et al., 1999). Although cluster temperature and baryon fraction agreed at the 10% level, the X-ray luminosities varied by a factor of two. This disagreement was limited to the gas properties of the halo, as Heitmann et al. (2005) found excellent agreement in the dark matter properties. Kravtsov et al. (2005) found a systematic bias in cluster baryon fraction between SPH and AMR algorithms, with AMR algorithms having a slightly higher baryon fraction. Mitchell et al. (2008) found that SPH codes suppress eddies and vortices in the gas more than AMR codes, particularly after a merger event. With more turbulence, and therefore more mixing in the AMR codes, low entropy gas is removed from the simulation. This effect on the entropy profile of halos, particularly in the core, explains the difference in cluster luminosity between AMR and SPH codes, even with only a small systematic bias in baryon fraction (Mitchell et al., 2008).

1.3.3 Cosmological Volumes

Simulations of very large volumes are necessary for measuring large-scale structure statistics, such as the halo mass function, the correlation function, and the power spectrum. Constructing the simulation requires a delicate balance between simulation volume, halo resolution, and mass range of resolved halos. No simulation can be all things, but they are useful complements to each other for calibrating properties of the large-scale structure of the universe.

As discussed in Chapter 2, the Hubble Volume simulation emphasized volume, simulating a periodic box with $L = 2\,h^{-1}$ Gpc in a ΛCDM universe (Evrard et al., 2002). Although halos of mass $5\times10^{13}h^{-1}\,\mathrm{M}_{\odot}$ were resolved with only 22 particles, the statistics at the high end of the mass function were excellent, allowing a calibration of the halo mass function that included the high mass end (Jenkins et al., 2001). The Millennium Simulation took the opposite approach: simulate a smaller volume, $L = 500\,h^{-1}$ Mpc, but with 10^{10} particles the mass resolution was much higher than

in the Hubble Volume. With a high mass resolution, Springel et al. (2005) could measure halo properties for a wide range of halo mass.

Computer processors are now fast enough to run hydrodynamic simulations of cosmological volumes in a reasonable amount of time. These simulations have only a simple treatment of the gas – gravity, shock-heating, and simple preheating – but can provide good statistics on the observed properties of galaxy clusters. I discuss the Millennium Gas Simulations (MGS) in more detail in Chapter 2, which have 10^9 total particles in a volume of $L = 500\,h^{-1}$ Mpc. The MGS are run with Gadget-2, which has an SPH treatment of the hydrodynamics, and include a model with simple preheating of the gas. The MareNostrum simulation also simulates a $500\,h^{-1}$ Mpc box, but with 2×10^9 total particles (Gottlöber & Yepes, 2007). Although the MareNostrum simulations consider two different treatments of the hydrodynamics – SPH and AMR – in both cases only an adiabatic treatment of the gas is used (Gottlöber & Yepes, 2007).

1.4 Bridging Simulations and Observations

In Section 1.2.2, I discussed the observational pieces required to obtain cosmological parameters from cluster surveys. In this section I discuss the theoretical contributions to obtaining cosmological parameters, such as halo mass functions and calibration of the selection function.

The mass selection function of an observed cluster survey depends on the scatter of the mass-signal relation. In Chapter 3 I present a value for the scatter in cluster mass and X-ray luminosity, which is necessary for calibrating flux-limited X-ray surveys. With multi-waveband surveys in progress, the covariance among observed signals at fixed mass is also necessary for calibrating the mass selection function, as well as interpreting the observed scaling relations (Nord et al., 2008). In Chapter 4 I present the covariance matrix from a pair of hydrodynamic simulations of a cosmological volume. I investigate the stability of covariance factors of pairs of signals to the underlying physics, and identify pairs of signals which will minimize the scatter in mass.

A calibration of the total halo mass function as a function of cosmology is necessary for determining cosmological parameters from cluster counts. Starting with a Gaussian random field in an expanding universe, Press & Schechter (1974) analytically derived the formation of structure and the distribution of galaxy masses. The analytic form was supported by simulations with $N = 1000$ particles. Assuming a constant mass-to-luminosity ratio, Press & Schechter (1974) matched the observed luminosity function of galaxies in the Coma cluster. Sheth & Tormen (1999a) used dark matter simulations to adapt the Press-Schechter formula to better match the mass functions in a range of cosmologies. Although the clustering bias does not affect the mass function in very large volumes, Sheth & Tormen (1999a) use simulations to calibrate the bias function.

Other work on the total halo mass function has focused on finding a fitting formula that can be easily adapted for different cosmologies and halo-finding techniques (Jenkins et al., 2001). The Jenkins Mass Function (JMF) was derived from the Hubble Volume simulation (Evrard et al., 2002), which I discuss in more detail in Chapter 2. Using a suite of cosmological simulations, Tinker et al. (2008) presented a fitting formula to the total halo mass function for a wide range of halo overdensities.

Most of the work on the total halo mass function to date has focused on dark matter only. However, as future cluster surveys will have cluster counts accurate at the $\sim 1\%$ level (Huterer & Takada, 2005), small systematic biases from baryonic physics cannot be ignored. In Chapter 5 I present a range of likely mass functions from simulations with different treatments of the astrophysics. Although my results are for extreme treatments of the heating and cooling of clusters, and thus likely bracket the true range, the $5 - 10\%$ systematic effect from baryons cannot be ignored.

CHAPTER 2

Simulations of Cosmological Volumes

2.1 Introduction

In this thesis, I have used data from several simulations of cosmological volumes, with periodic cubes with lengths $L \geq 500\,h^{-1}$ Mpc. As discussed in Chapter 1, N-body simulations are necessary for calibrating the total halo mass function for a given cosmology. Furthermore, a large volume produces a statistically significant sample of halos above some resolution threshold, usually on the order of $\sim 10^2$ particles.

2.1.1 Dark Matter Simulations

Cosmological simulations of dark matter particles are used for studying large-scale structure, calibrating the halo mass function, and studying individual halo structures. In this thesis I have used results related to two major dark matter simulations. The Hubble Volume simulations, used in Chapter 3, model a periodic cube of length $L = 2\,h^{-1}$ Gpc in a ΛCDM cosmology (Evrard et al., 2002). Although a halo mass of $5 \times 10^{13}\,h^{-1}\,\mathrm{M}_\odot$ only corresponds to 22 particles, the extremely large volume provides excellent statistics on large-scale structure, and on the high-mass end of the mass function. Due to the steepness of the mass function, such large volumes are necessary for meaningful statistics on halo properties over a mass cut of $M > 10^{15}\,h^{-1}\,\mathrm{M}_\odot$.

The Millennium Simulation models 10^{10} particles in a periodic cube of length $L = 500\,h^{-1}$ Mpc (Springel et al., 2005). The smaller volume leads to fewer high-mass halos; however, halos of mass $5 \times 10^{13}\,h^{-1}\,\mathrm{M}_\odot$ are resolved with approximately 5×10^4 particles. Having detailed halo structures across a range of masses is a good complement to the very large volume of the Hubble Volume simulations. The

Millennium Gas Simulations, which I use in Chapters 4 and 5, have the same initial conditions as the Millennium Simulation, but with a mass resolution about twenty times lower.

2.1.2 Hydrodynamic Simulations

Most hydrodynamic simulations of galaxy clusters have focused on a detailed, physical treatment of a few halos in a small volume. These simulations usually include the effects of AGN activity, star formation, and supernovae (Borgani et al., 2006; Kravtsov et al., 2006). In a cosmological volume, simulated in a periodic cube with $L \gtrsim 500\,h^{-1}$ Mpc, directly simulating these astrophysical processes is not feasible with the current state of computing. Instead, hydrodynamic simulations of these volumes are usually limited to an adiabatic treatment of the gas, where only gravity and shock heating occur (Gottlöber & Yepes, 2007). Other simulations model the effects of further astrophysical processes, such as the heating of the intracluster medium (Pearce, 2007). This approach produces a large sample of halos with measurable X-ray and SZ properties. Although these simulations do not have a detailed treatment of the astrophysical processes, they provide a useful complement to the detailed simulations of small volumes. In Chapters 4 and 5, I used the Millennium Gas Simulations, which are a pair of simulations of a periodic cube with $L = 500\,h^{-1}$ Mpc.

2.2 Hubble Volume Simulations

I use key results from the Hubble Volume Simulations in Chapter3, particularly the halo mass function (Jenkins et al., 2001) and the halo catalog from the simulation lightcones. In this section I discuss the fundamental properties of the Hubble Volume simulations, the creation of the lightcones, and the derivation of the total halo mass function.

2.2.1 Simulation Details

The Hubble Volume simulations are a pair of N-body simulations of 10^9 particles each in a ΛCDM cosmology ($\Omega_m = 1 - \Omega_\Lambda = 0.3$) and in a τCDM cosmology ($\Omega = \Omega_m = 1$).

The simulations are tuned to resolve the Coma cluster, of $M_{\rm COMA} = 1.1 \times 10^{15} h^{-1} {\rm M}_{\odot}$, with 500 particles, leading to particle masses of $2.2 \times 10^{12}\ h^{-1}\ {\rm M}_{\odot}$ in each model (Evrard et al., 2002). With one billion particles of equal mass in each simulation, but different mean densities, the two simulations have different volumes. The models are simulated in periodic cubes of length L, where $L = 3\,h^{-1}$ Gpc in the ΛCDM model and $L = 2\,h^{-1}$ Gpc in the τCDM model.

2.2.2 Lightcone Surveys

The Hubble Volume simulations included the construction of simulated lightcones, to more closely mimic the observed results from galaxy cluster surveys. These lightcones include two spheres of depth $L/2$, which corresponds to a depth of $z = 0.57$ in the ΛCDM model and a depth of $z = 0.42$ in the τCDM model. The octant surveys, which have an angular size of $\sim 10,000\,{\rm deg}^2$, have a depth of the full cubelength L, which corresponds to a dept of $z = 1.46$ in the ΛCDM model and $z = 1.25$ in the τCDM model. One sphere is centered at the center of the simulation volume, while the second sphere and the octant surveys are centered at the origin of the (periodic) simulation volume. I used the spherical surveys in Chapter 3 of this thesis, for comparison to observations which extended to redshift $z \sim 0.5$. Above a mass limit of $5 \times 10^{13}\ h^{-1}\ {\rm M}_{\odot}$, or 22 particles, the spherical surveys have approximately 565,000 halos (Evrard et al., 2002).

2.2.3 Halo Mass Function

From the Hubble Volume simulations, Jenkins et al. (2001) derived a functional form of the halo mass function, using $\ln \sigma^{-1}(M)$ as the mass variable. In this form, $\sigma^2(M)$ is the variance of the density field after smoothing with a spherical kernel at the mean density of mass M. The mass fraction is then defined as:

$$f(\ln \sigma^{-1}(M)) = \frac{M}{\bar{\rho}_m(z)} \frac{dn(<M,z)}{d \ln \sigma^{-1}}, \tag{2.1}$$

where $\bar{\rho}_m(z)$ is the mean density of the universe at the given epoch z, and $n(<M,z)$ is the cumulative number density of halos below mass M at epoch z. From this, the

differential number function of halos is given as

$$n(M,z) = \frac{\bar{\rho}_m(z)}{M} \frac{d\ln\sigma^{-1}(M)}{d\ln M} f(\ln\sigma^{-1}(M)). \tag{2.2}$$

Jenkins et al. (2001) describe $f(\ln\sigma^{-1}(M))$ with the functional form

$$f(\ln\sigma^{-1}) = A\exp(-|\ln\sigma^{-1} + B|^{\epsilon}). \tag{2.3}$$

The fit parameters A, B, and ϵ depend on the cosmology, and have a slight dependence on the type of groupfinder used: friends-of-friends or spherical overdensity. In Chapter 3 I used the Jenkins Mass Function, with parameters for spherical overdensity groupfinding, for generating cluster counts in flux and redshift.

2.3 Millennium Gas Simulations

I used the Millennium Gas Simulations (hereafter MGS) in Chapters 4 and 5. In this section I discuss the fundamental properties of the MGS, creation of the halo catalog, and some initial results from the simulations.

2.3.1 Simulation Details

The MGS are a pair of resimulations of the original Millennium Simulation (Springel et al., 2005). The Millennium Simulation consists of 10^{10} dark matter particles in a cube of length $500\,h^{-1}$ Mpc. Each particle has mass $8.6\times10^8\,h^{-1}\,\mathrm{M}_\odot$, such that a small galaxy group of $M = 5\times10^{13}\,h^{-1}\,\mathrm{M}_\odot$ is resolved with $\sim 5\times10^4$ particles. The simulation has a spatial resolution of $5\,h^{-1}$ kpc. The cosmological parameters of the Millennium Simulation are $\Omega_m = \Omega_{dm} + \Omega_b = 0.25$, $\Omega_b = 0.045$, $\Omega_\Lambda = 1 - \Omega_m = 0.75$, $n = 1$, and $\sigma_8 = 0.9$. These parameters agree with the cosmological parameters measured from the first year of observations from WMAP (Spergel et al., 2003).

The MGS are simulated in the same volume as the original Millennium Simulation, with the same cosmology and initial conditions, but both the mass and spatial resolution are significantly coarser. The MGS consists of 5×10^8 dark matter particles, each of mass $1.422\times10^{10}\,h^{-1}\,\mathrm{M}_\odot$, and 5×10^8 gas particles, each of mass $3.12\times10^9\,h^{-1}\,\mathrm{M}_\odot$.

The spatial resolution of the MGS is $25\,h^{-1}$ kpc (Pearce, 2007). The simulations were run with a standard implementation of Gadget-2, which uses a smoothed particle hydrodynamic (SPH) treatment of the gas and a TreePM treatment of the dark matter particles (Springel, 2005a).

The MGS include two models of the gas treatment. One model is adiabatic, including only gravitational effects and shock-heating. Throughout this thesis, I refer to this model as "gravity-only", or the `GO` model. The second model includes preheating and cooling, and was tuned to match the observations of clusters at redshift zero (Hartley et al., 2008). The preheating, meant to model the effects of star formation and AGN activity, is simulated with an entropy boost of all gas particles to $S = 200\,\mathrm{keV\,cm^{-2}}$ at redshift $z = 4$. The cooling comes from the cooling function of Sutherland & Dopita (1993), and is for a fixed gas metallicity of 0.3 solar. In practicality, the preheating at redshift $z = 4$ ends the influence of the cooling in the simulation. I refer to this model as the `PH` model.

With coarser mass and spatial resolution, we do not expect the halos in MGS to exactly match those in the original Millennium Simulation. However, with a friends-of-friends (FOF) halo finder, the positions of halos in the MGS match the original halos within $50\ h^{-1}$ kpc. This agreement allows for one-to-one matching of halos between simulations.

2.3.2 Initial Results

Hartley et al. (2008) used the `PH` model to investigate the luminosity-temperature ($L-T$) relation. When using emission-weighted temperatures, the agreement in slope and normalization with a range of local observations is quite good (Hartley et al., 2008). The strong preheating in the `PH` model does not reproduce the strong cores observed in galaxy clusters, and thus the simulated $L-T$ relation has a lower scatter than the observed scatter. With such a large sample of massive ($M > 5\times10^{13}h^{-1}\mathrm{M}_{\odot}$) halos, Hartley et al. (2008) was able to measure a deviation from a simple power law for the $L-T$ relation at the high mass end of the relation. Hartley et al. (2008) also tracked merger histories for the halos, finding that merger events significantly boost

both the luminosity and temperature of a halo. Without taking merger events into account, this could lead to over-counting high-mass halos.

2.3.3 Halo Catalog

For Chapters 4 and 5, I created a halo catalog in both the `PH` and the `GO` models using the spherical overdensity approach to groupfinding. With this approach, I have a catalog of halos which enclose a mean density of $\Delta\rho_c(z)$, where $\rho_c(z)$ is the critical density of the universe at epoch z. For most of my work, I used $\Delta = 200$ for the identification of halos. The radius of a halo which encloses a mean density of some Δ is denoted as r_Δ. As observers frequently measure X-ray cluster properties within some radius defined by an overdensity, the spherical overdensity approach is ideal for producing a halo catalog for comparison with observations.

The first step in creating the halo catalog is identifying potential halo centers. I identified local density peaks with an $N^{th} - nearest - neighbor$ approach, which finds the distance of each dark matter particle to its N^{th} closest particle. Particles with lower values of that distance are in a denser region, and thus are more likely to be the center of a halo. I chose $N = 32$: higher values of N increased the computational time but did not significantly change the results.

From the $N^{th} - nearest - neighbor$ calculation, I had a list of dark matter particles ranked by local density. I then did spherical overdensity groupfinding in an iterative fashion: I started with the densest dark matter particle and worked outwards in both dark matter and gas particles until the halo enclosed a spherical region with mean density of $\rho = \Delta\rho_c(z)$. I then moved on to the next densest dark matter particle that was not already in a halo, and so on until all halos with more than 100 particles were found. Particles were permitted to be in multiple halos, but the center of a new halo could not be in another halo. I also removed halos whose center-of-mass was in another halo. These removed halos were not true halos, but filaments and dense regions living just outside the radius of a massive halo.

At redshift zero, in the `PH` simulation there are approximately 220,000 halos with at least 100 particles, and 370,000 over this particle cut in the `GO` simulation. I use a

mass cut of $5 \times 10^{13}\, h^{-1}\, \mathrm{M}_{\odot}$ for most of the analysis in this thesis, and over this mass cut there are 4474 halos at redshift zero in the PH simulation and 5612 halos in the GO simulation. I discuss the difference in number of halos over a fixed mass between the two models in Chapter 5. Once I have this sample of halos over the mass cut, I identify each halo as a primary or a satellite. As the groupfinder permits overlapping halos, any halo which overlaps with a halo more massive than itself is designated as a "satellite" halo. Halos which either do not overlap with another halo, or whose overlapping neighbors are less massive than itself, are designated as "primary" halos. At redshift zero, both simulations have a satellite fraction of $\sim 2\%$. The satellites are not included in the discussion of bulk halo properties in Chapter 4, but are included in the analysis when presenting the mass function in Chapter 5. In both cases, the decision about treatment of the satellites was based on matching observed samples as closely as possible.

CHAPTER 3

X-Ray Luminosity-Mass Relation for Local Clusters of Galaxies

3.1 Introduction

The counts, spatial clustering and bulk properties of the most massive halos in the universe offer a means to test cosmological physics (Wang & Steinhardt, 1998; Haiman et al., 2001; Carlstrom et al., 2002; Majumdar & Mohr, 2003; Battye & Weller, 2003b; Wang et al., 2004). Although only a handful of high redshift ($z \gtrsim 1$) clusters are currently known, the number will grow considerably in the next five years, as a result of improved search techniques using multi-band optical (Gladders & Yee, 2005a) combined with infrared (Stanford et al., 2005) or X-ray (Rosati et al., 1998; Romer et al., 2000; Mullis et al., 2005) imaging. Sunyaev-Zel'dovich (SZ) surveys, based on interferometric (Holder et al., 2000; Loh et al., 2005), or bolometric (Schwan et al., 2003; Kosowsky, 2003; Ruhl et al., 2004) approaches, will ultimately extend the reach of the cluster population to $z \sim 3$.

Since observational surveys do not select directly on halo mass, interpreting the data requires a model that relates observable bulk features, such as temperature, Sunyaev-Zel'dovich decrement, or X-ray luminosity, to mass. Given sufficiently rich cluster samples, one can solve for parameters describing the mass-observable relation along with cosmological parameters in a simultaneous fashion (Levine et al., 2002; Majumdar & Mohr, 2003; Lima & Hu, 2004a). Power-law relationships between bulk properties are expected on dimensional grounds (Kaiser, 1986), but the scatter about mean mass-observable relationships, a crucial element of self-calibration exercises (Levine et al., 2002; Lima & Hu, 2005a), is presently poorly understood.

In this paper, we use counts and scaling relations of low redshift clusters in the HIFLUGCS survey (Reiprich & Böhringer, 2002) to investigate the statistical relationship between X-ray luminosity and total halo mass. The method relies on numerical simulations for calibration of the space density of massive halos (Sheth & Tormen, 1999b; Reed et al., 2003; Jenkins et al., 2001; Warren et al., 2005) and for an estimate of the covariance of X-ray temperature and luminosity at fixed mass.

For a set of structurally identical, spherical halos with mass M_Δ, radius R_Δ (here Δ is a threshold defining the halo edge relative to the critical density) and with intracluster gas fraction $f_{\rm ICM} = M_{\rm ICM}/M_\Delta$, one expects the bolometric luminosity to scale as (Arnaud & Evrard, 1999)

$$L_{\rm bol}(M,z) \;=\; C\,Q_L\,f_{\rm ICM}^2\;\rho_c^{7/6}(z)\;M_\Delta^{4/3}, \tag{3.1}$$

where C is a constant, $\rho_c(z)$ is the critical density, and $Q_L = (3/4\pi)\int d^3y g^2(y)$ is a structure function that is sensitive to the second moment of the normalized gas density profile

$$\rho_{\rm ICM}(r) = f_{\rm ICM}\Delta\rho_c(z)\,g(r/R_\Delta). \tag{3.2}$$

If the ensemble average gas fraction or radial structure function vary with mass and epoch, then the power law exponents will generally differ from the basic expectation. This is the case for a "preheated" ICM, with $L \propto M^{11/6}$, invoked by Evrard & Henry (1991) to reproduce the X-ray luminosity function in an $\Omega_m = 1$ cold dark matter cosmology. Observations of the $L - T$ relation find a steeper slope, $L \propto T^3$, than expected from self-similarity (Mushotzky & Scharf, 1997; Fairley et al., 2000; Novicki et al., 2002). Models incorporating angular momentum in halos have been able to reproduce the steeper relations (Del Popolo et al., 2005).

In general, deviations from spherical symmetry and differences in formation history and dynamical state will produce variations in $f_{\rm ICM}$ and $g(y)$ among halos of fixed mass, leading naturally to some distribution $p(L|M,z)$ of soft band luminosity L. We employ here a log-normal conditional likelihood, with fixed dispersion $\sigma_{\ln L}$,

centered on a power-law scaling relation

$$L \;=\; L_{15,0}\;\rho_c^s(z)\;M^p. \tag{3.3}$$

It is important to note that this equation characterizes the log mean behavior of a mass-limited population. Surveys that are incomplete in mass may differ from this.

For a given choice of model parameters, cluster counts in flux and redshift are generated by convolving $p(L|M,z)$ with the halo mass function of Jenkins et al. (2001) and applying a mean fractional flux error correction. Comparing to REFLEX survey counts (Böhringer et al., 2004) determines most likely parameters. Since the REFLEX survey is relatively shallow, we choose not to solve for general redshift evolution. Instead, we simply compare cases of self-similar ($s=7/6$) and no ($s=0$) evolution. For soft X-ray luminosities, the expected mass and redshift scalings are somewhat weaker than the bolometric case of equation (3.1), $L \propto M\rho_c(z)$, but we employ $s=7/6$ as a slightly extreme variant.

Our analysis is therefore focused on the slope p, present-epoch intercept, $L_{15,0}$, at $10^{15}\,h^{-1}\,\mathrm{M}_\odot$, and the dispersion $\sigma_{\ln L}$, which we express in terms of the equivalent dispersion in mass $\sigma_{\ln M}=\sigma_{\ln L}/p$.

A more direct approach to the problem of relating luminosity to mass involves using individual cluster mass estimates derived under the assumption of strict hydrostatic and/or virial equilibrium. Reiprich & Böhringer (2002) (hereafter RB02) perform this analysis with 63 clusters from the flux-limited HIFLUGCS survey, finding consistency with the power-law expectation, equation (3.3), with a slope slightly steeper than self-similar and with a few tens of percent intrinsic scatter in mass at fixed luminosity. A promising future approach to this problem is to use weak lensing mass estimates of stacked cluster samples (Johnston, 2005).

In §3.2, we explain the model and our approach to analyzing the REFLEX survey counts. In §3.3, parameter constraints that result from matching the counts are presented and found to be strongly degenerate. We therefore apply a pair of additional constraints, one based on the clustering of REFLEX clusters and the other on the

observed scatter in the temperature-luminosity relation. The latter exercise requires input from cosmological simulations of clusters.

We compare to results of RB02 and discuss implications for cluster selection and hydrostatic mass estimates in §3.4. A summary and conclusions are given in §3.5. Except in §3.4, our calculations assume a concordance ΛCDM cosmology with $\Omega_m = 0.3$, $\Omega_\Lambda = 0.7$, $\mathrm{H}_0 = 100h\,\mathrm{km\,s^{-1}\,Mpc^{-1}}$, and $\sigma_8 = 0.9$.

Throughout the paper, L is the X-ray luminosity in the rest-frame, soft ROSAT passband ($0.1 - 2.4$ keV) in units of 10^{44} erg s^{-1} assuming $h = 0.7$. The mass M is taken to be M_{200}, the mass contained within a sphere whose mean interior density is $200\rho_c(z)$, expressed in units of $10^{15}\,h^{-1}\,\mathrm{M}_\odot$. The reader is hereby notified that we employ different Hubble constant conventions when presenting values for luminosity and mass.

3.2 Modeling the Luminosity Function

After briefly introducing the REFLEX cluster sample used in the analysis, this section details our approach to modeling cluster counts in flux and redshift, including evolutionary corrections.

3.2.1 The REFLEX Survey

We use cluster counts from the REFLEX (ROSAT-ESO-Flux-Limited-X-ray) Cluster Survey, which covers an area of 4.24 str and includes 447 identified galaxy clusters down to a flux limit of 3×10^{-12} ergs s^{-1} cm^{-2} in the (0.1 to 2.4 keV) ROSAT band (Böhringer et al., 2004). The X-ray clusters have been correlated with optical data from the COSMOS data base with a relatively low threshold to define a highly complete cluster candidate catalogue. Cluster validation and redshift determinations were achieved by an intense spectroscopic follow-up observing program at the European Southern Observatory, supplemented by available literature.

Luminosity determinations and the first REFLEX sample release are described in Böhringer et al. (2001). Determination of the survey selection function is described in Böhringer et al. (2002) and references therein. We do not incorporate selection

function uncertainties directly into our analysis. This simplification is unlikely to significantly affect our conclusions, since at the high flux-limit of the REFLEX survey the sample is well understood. Böhringer et al. (2001) estimate a loss under 5% of clusters in low exposure regions, and tests presented in that work (*cf.,* Figure 25) show that this changes the derived luminosity function by less than 2%.

The redshifts and luminosities of the REFLEX clusters are shown in Figure 3.1. The solid lines are lines of constant flux: 4, 10, and 25 $\times$ 10^{-12} ergs s^{-1} cm^{-2} in the [0.1-2.4 keV] band. In the following section, we perform a likelihood analysis on this count distribution in flux and redshift.

We must account for several survey effects when computing model expectations. Our basic model predicts the total flux while the REFLEX data are based on flux detected within the fixed angular aperture. We correct the data for this aperture effect by using the extrapolated fluxes calculated by Böhringer et al. (2001). This correction results in an 8% average increase in luminosity, but for a few bright nearby clusters the correction is larger.

We also include a K-correction in our model. The luminosity L in our mass-luminosity relation is the emissivity integrated over the rest-frame, 0.1-2.4 keV band, whereas the REFLEX data are derived from the emissivity over a band redshifted by a factor $(1 + z)$. We find that the K-correction used for the REFLEX survey construction, listed in Table 3 of (Böhringer et al., 2004), is well fit by the form

$$K(z, T) \;=\; \Big(1 + (1 + \log_{10}[T/5\,\mathrm{keV}]\; z)\Big)^{1/2} \tag{3.4}$$

where $L_{\rm obs} = K(z, T)\; L_{\rm rest}$. We assign temperatures to halos in a manner described below.

3.2.2 Theoretical Model

The space density of dark matter halos is now accurately calibrated for the case of hierarchical clustering from an initially Gaussian random density field. We use parameters derived for the mass scale M_{200} by Evrard et al. (2002), based on the

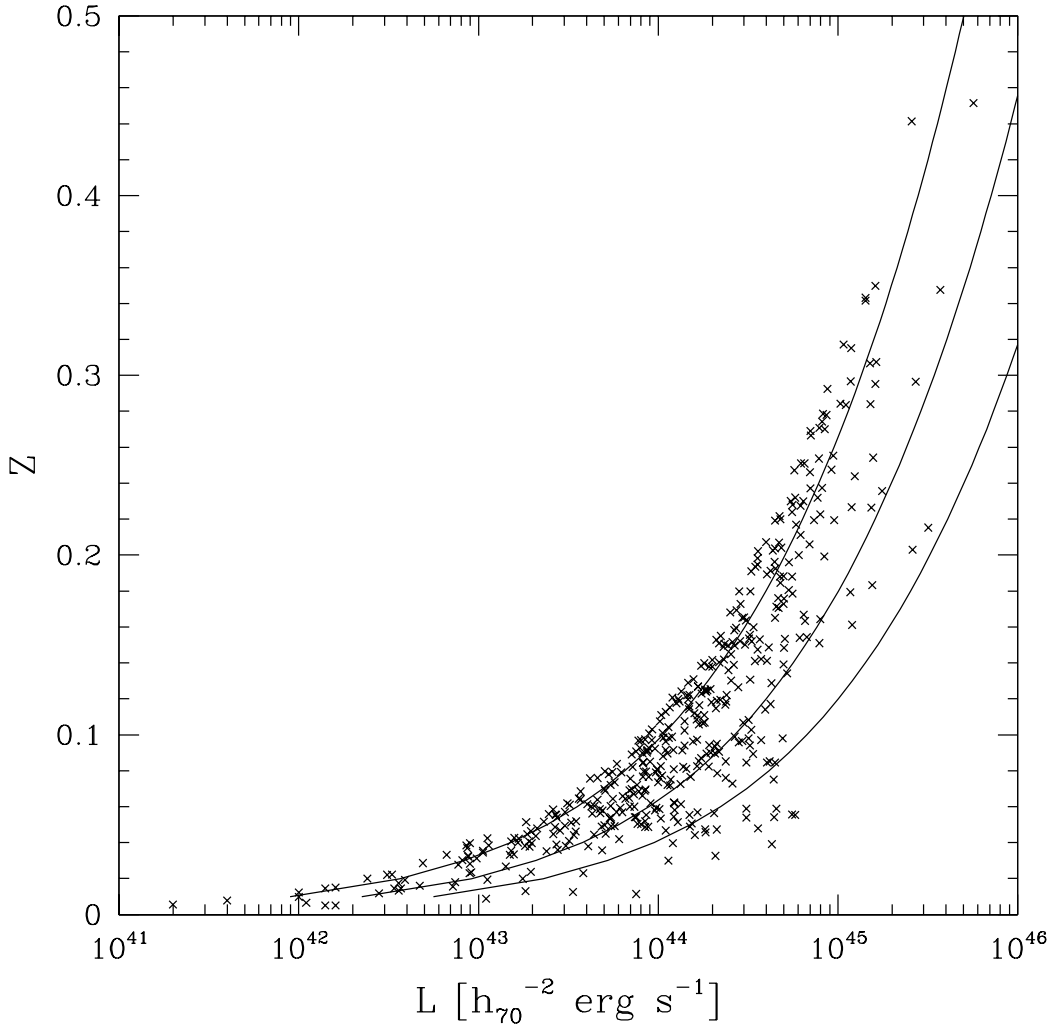

Figure 3.1. Redshifts and observed luminosities of 447 clusters in the full REFLEX survey. The solid lines are lines of constant flux: 4, 10, and 25 $\times$ 10^{-12} ergs s^{-1} cm^{-2} in the observed (0.1 to 2.4 keV) ROSAT band.

Ω_m	s_0	s_1	s_2	A	B	ϵ
0.24	0.468	0.267	0.0123	0.216	0.737	3.86
0.30	0.549	0.281	0.0123	0.220	0.730	3.86
0.36	0.608	0.287	0.0123	0.224	0.723	3.86

Table 3.1. Filtered Power Spectrum and JMF Parameters

Jenkins mass function (hereafter JMF, Jenkins et al. (2001)) form determined from a suite of cosmological simulations.

The JMF is described by a similarity variable $\sigma(M,z)$, where σ^2 is the variance in the linear density field after top-hat filtering fluctuations on mass scale M. The function $\sigma(M,z)$ is a monotonic decreasing function of mass for bottom-up models of structure formation and its inverse is well fit in the log by a quadratic relation, $\ln\sigma^{-1}(M,0) = s_0 + s_1 \ln M + s_2 (\ln M)^2$. Fit parameters for specific models we employ are listed in Table 3.1. Jenkins et al. (2001) show that the mass fraction in halos of mass M at redshift z

$$f(M) \equiv \frac{M}{\rho_m(z)} \frac{\mathrm{d}n(M,z)}{d\ln\sigma^{-1}}, \tag{3.5}$$

is well fit by

$$f(M) = A \ \exp(-|\ln\sigma^{-1} + B|^{\epsilon}). \tag{3.6}$$

When evaluating the mass function, we use the fact that $\sigma(M,z)$ scales with the linear growth factor of density fluctuations $D(z)$. In addition, the parameters A, B vary linearly with Ω_m as described in Evrard et al. (2002). The $z=0$ values are listed in Table 3.1.

In a small comoving volume element dV at redshift z, we write the probability dp of finding a cluster of mass M and luminosity L as

$$dp \ = \ p(L|M,z)\, n(M,z) d\ln M d\ln L\, dV \tag{3.7}$$

We assume a log-normal conditional probability

$$p(L|M,z) \ = \ \frac{1}{\sqrt{2\pi}\sigma_{\ln L}} \exp\left[-\frac{(\ln L - \overline{\ln L})^2}{2{\sigma_{\ln L}}^2} \right] \tag{3.8}$$

with constant dispersion $\sigma_{\ln L}$ and a log-mean (or median) luminosity that follows

$$\overline{\ln L}(M,z) \;=\; \ln L_{15}(z) + p\,\ln M \tag{3.9}$$

where the normalization

$$\ln L_{15}(z) = \ln L_{15,0} + s\,\ln\left[\rho_c(z)/\rho_c(0)\right] \tag{3.10}$$

sets the luminosity of a cluster with mass $10^{15}\,h^{-1}M_\odot$ at redshift z.

In principle, the dispersion $\sigma_{\ln L}$ could be variable in mass or redshift, but we assume it to be constant, at least over the range of masses ($\gtrsim 3\times10^{13}\,h^{-1}\ \mathrm{M}_\odot$) and redshifts ($z\lesssim 0.3$) probed by the REFLEX sample. The same is true for the slope parameter p.

The luminosity function at any epoch is the conditional probability convolved with the JMF

$$dn(L,z) = \int d\ln M\ n(M,z)\,p(L|M,z)\,d\ln L. \tag{3.11}$$

The number counts of clusters at redshift z with observed flux greater than f is

$$\frac{dN(>f,z)}{dz} = \frac{dV}{dz}\int_{L_{\min}(z)}^{\infty} dn(L,z) \tag{3.12}$$

where $L_{\min}(z)=4\pi d_L^2(z)f/K(z,T)$, with $d_L(z)$ the luminosity distance and $K(z,T)$ the K-correction fit of equation (3.4). We use the analytic luminosity distance approximation presented in Pen (1999). To calculate halo temperatures, we use the relation of Evrard et al. (2002) that reproduces the local temperature function in a concordance model

$$kT \;=\; 6.5\ (h(z)M)^{2/3}\ \sigma_8^{-5/3}\,\mathrm{keV}, \tag{3.13}$$

with $h(z)=h(0)\Big(\rho_c(z)/\rho_c(0)\Big)^{1/2}$ the Hubble parameter at redshift z. For our choice of normalization, the $z=0$ intercept at $10^{15}\,h^{-1}\ \mathrm{M}_\odot$ is 7.7 keV.

With the log-normal assumption, equation (3.8), the flux-limited counts simply weight the mass function with a complementary error function giving the fraction of

halos that satisfy the flux limit at each redshift

$$\frac{dN(>f,z)}{dz} = \frac{1}{2}\frac{dV}{dz}\int d\ln M\ n(M,z)\,\mathrm{erfc}\,(\mathrm{y_{min}(M,z)}). \tag{3.14}$$

with $y_{\rm min}(M,z) = [\ln L_{\rm min}(z) - \overline{\ln L}(M,z)]/\sqrt{2}\sigma_{\ln L}$.

Our likelihood analysis is based on differential counts in flux and redshift

$$\frac{d^2N(f,z)}{dz\,d\ln f} \;=\; \frac{dV}{dz}\int d\ln M\ n(M,z)\,p(L|M,z) \tag{3.15}$$

with $L = 4\pi d_L^2(z) f/K(z,T)$.

3.2.3 Flux Errors

We must incorporate flux uncertainties in the REFLEX survey into our analysis. The mean fractional error in cluster flux is not large, $\langle \delta f/f \rangle = 0.17$, but the individual errors tend to increase at lower flux levels. Approximating the flux errors as constant, we modify the theoretical predictions by convolving the raw predicted counts with a Gaussian in $\ln f$ of fixed width $\sigma = 0.17$. This fractional scatter adds in quadrature to the intrinsic model scatter.

To avoid clusters with flux errors substantially larger than the mean, we use a flux limit 4×10^{-12} erg s^{-1} cm^{-2} in the likelihood analysis, a few flux error sigma higher than the formal REFLEX flux limit 3×10^{-12} erg s^{-1} cm^{-2}. This reduces the sample size to 299 clusters but, because of the strong influence of the scatter constraint discussed in §3.3.3 below, the uncertainties in our final parameter estimates are not strongly affected by the reduced counts.

As a check on this approach to incorporating flux errors, we have used an alternative that compares the uncorrected theoretical counts to a Monte Carlo ensemble of REFLEX realizations created using the set of measured flux errors. The mean likelihood of the ensemble, using flux limit 4×10^{-12} erg s^{-1} cm^{-2}, produces parameter constraints that lie within 1σ of the results obtained using the convolution approach. We present our results using the latter method.

3.2.4 Redshift Evolution

Ideally, we would include the evolution parameter s of equation (3.1) as a free parameter, along with $L_{15,0}$, p and $\sigma_{\ln M}$, in our analysis. But because of the relatively shallow sample, and the lack of uniform luminosity and redshift coverage (see Figure 3.1), we defer this exercise to future, deeper samples.

Instead, we limit our investigation to two distinct, and likely extreme, cases: the self-similar (SS) model of eq'n (3.1) and a no evolution (NE) model with $L_{15}(z) = L_{15,0}$. Self-similar evolution is supported by recent work of Maughan et al. (2005), who investigate the redshift behavior of the luminosity–temperature relation in a sample of eleven clusters to redshift $z \sim 1$. However, Ettori et al. (2004) do not see strong evolution to $z = 1.3$ in the luminosity–mass relation with a sample of 28 clusters.

3.2.5 Parameter Degeneracies

The convolution of the mass function is affected slightly differently by the three model parameters. An increase in $L_{15,0}$ simply shifts the luminosity scale to brighter values while the slope p controls the local slope of the luminosity function, with lower p being steeper. Changing $\sigma_{\ln M}$ produces a combination of the above effects, affecting both the shape and normalization. Over a finite range of luminosity, changes induced by varying one parameter can thus be offset by appropriate variations of the other two. One therefore anticipates degeneracies among the model parameters when fitting to counts alone.

For the case of a pure power law mass function $n(M) \propto M^{-\gamma}$, we show in the Appendix that the degeneracy is exact and takes the form

$$C \;=\; \ln L_{15,0} + (\gamma p/2)\sigma_{\ln M}{}^2, \tag{3.16}$$

where C is the quantity that is constrained by the data.

3.3 Results

After first presenting parameter constraints that result from matching the REFLEX survey flux-limited counts, we extend the analysis to include clustering bias and scatter in the luminosity-temperature relation. We then compare our model results to those of RB02, and discuss the important role of flux-limited selection.

3.3.1 Constraints from REFLEX counts

We calculate likelihoods based on the expected survey counts in narrow flux and redshift bins, following the Poisson approach described in Pierpaoli et al. (2001). We define confidence intervals relative to the best fit model using $\ln\left(\frac{\mathcal{L}}{\mathcal{L}_{\max}}\right) = -\chi^2/2$, where $\mathcal{L}_{\max}$ is the maximum likelihood of all the models examined.

Figure 3.2 shows 68 and 99% confidence contours for the model parameters that result from matching the REFLEX survey counts. Each panel shows likelihoods marginalized over the missing parameter. Solid lines assume self-similar evolution of the luminosity while dashed lines assume no redshift evolution. Due to the degeneracy between the three parameters discussed in section 3.2.5, the observed counts are reproduced at 99% confidence over a fairly broad swath of parameter space. For the SS case, the slope can take values $1.55 < p < 1.85$, intercepts lie in the range $1.25 < L_{15,0} < 1.85$, and the scatter is bounded by $\sigma_{\ln M} < 0.42$. Zero scatter in the mass-luminosity relation, a seemingly unphysical solution given that cluster-sized halos are frequently dynamically active, is actually the most likely model, with slope $p = 1.70$ and $\ln L_{15,0} = 1.70$.

The NE model is shifted to a brighter intercept and steeper slope. The brighter intercept is needed to produce sufficient numbers of high luminosity clusters at moderate redshifts, while the steeper slope avoids overproducing counts at low luminosities and redshifts.

Figure 3.3 shows that the best fit SS and NE models provide good matches to the observed REFLEX counts in flux and redshift. Also plotted are discrete counts derived from the Hubble Volume (HV) mock sky catalogs (Evrard et al., 2002). For each halo, we assign a luminosity using parameters of the best-fit SS model, along

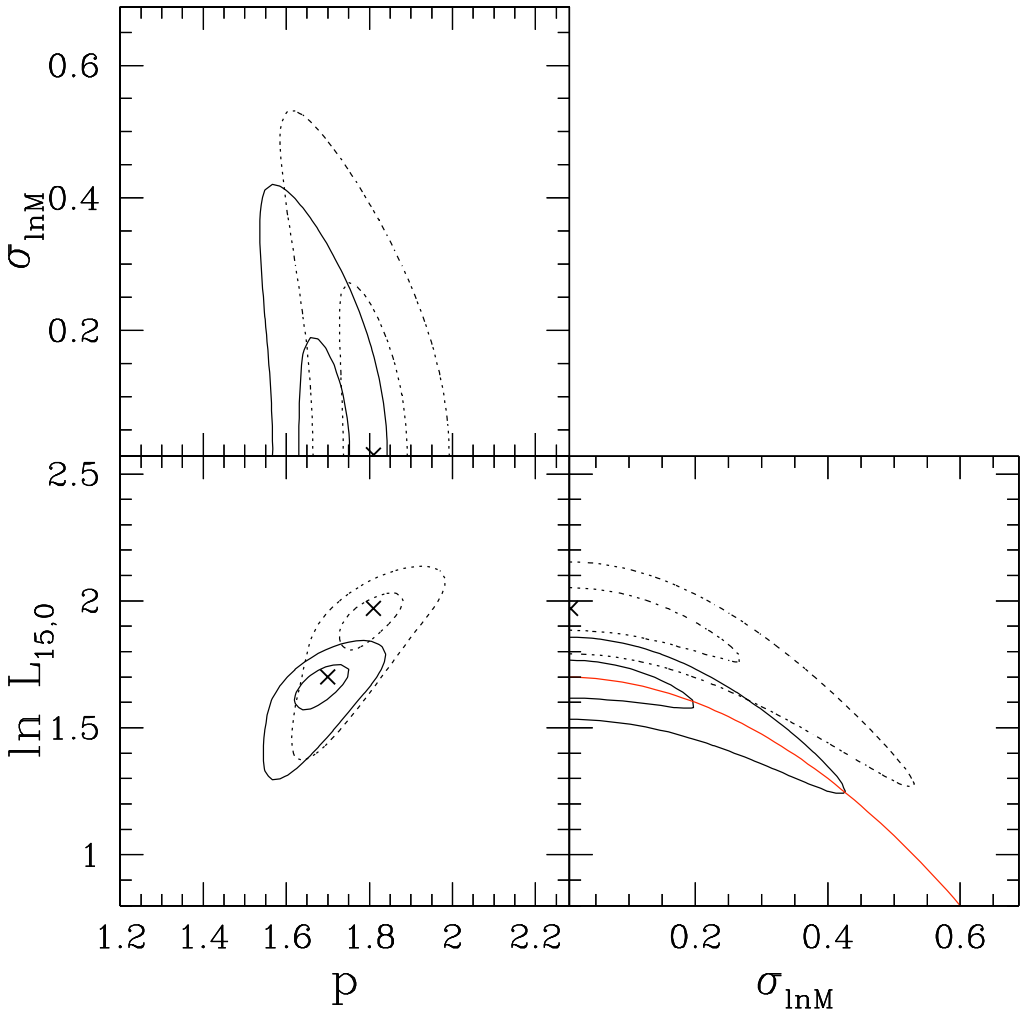

Figure 3.2. Contours of the 68 and 99% marginalized likelihoods of the model parameters that result from matching the REFLEX counts are plotted for self-similar (solid) and no evolution (dashed) assumptions. Crosses mark the maximum likelihood of the three-parameter model. The added curve in the lower right-hand panel plots the degeneracy between $\sigma_{\ln M}$ and $\ln L_{15,0}$ expected for a power-law number function, equation (3.16).

with a temperature using equation (3.13). The K-corrected flux is then calculated and used to determine counts in mock surveys with REFLEX angular sky coverage. The lines in Figure 3.3 result from different random assignment of luminosities to halos using the best fit final parameter discussed in § 3.3.4.

To improve these parameter constraints we must include additional information from related observations or from theoretical priors derived, for example, from numerical simulations. We follow a largely empirical approach, and move on in the following sections to add constraints from the effective bias of the REFLEX survey and from the scatter in the observed temperature–luminosity relation. As explained below, interpreting the T-L scatter requires input from cosmological simulations.

3.3.2 Clustering Bias

Massive halos display stronger spatial clustering than the density field in general (Kaiser 1984). The halo–halo power spectrum $P_{\rm hh}(k)$ for mass-limited samples exhibits a nearly constant, mass-dependent bias $b(M) = \sqrt{P_{\rm hh}/P}$ on large scales. We use the form for this bias derived by Sheth & Tormen (1999b),

$$b(M) = 1 + \frac{1}{\delta_c}\left[\frac{a_s\delta_c^2}{\sigma^2} - 1 + \frac{2p_s}{1+(a_s\delta_c^2/\sigma^2)^{p_s}}\right] \tag{3.17}$$

with parameter values $\delta_c = 1.68$, $a_s = 0.75$ and $p_s = 0.3$ from Hu & Kravtsov (2003a). The effective bias of a volume-limited sample centered at (low) redshift z is then

$$b_{\rm eff} = \frac{\int d{\rm ln}M\, w(M,z)\, n(M,z)\, b(M)}{\int d{\rm ln}M\, w(M,z)\, n(M,z)} \tag{3.18}$$

where $w(M,z)$ is a weight function that gives the fraction of halos of mass M that lie above the minimum luminosity L_{min} of the sample at redshift z. We calculate the bias appropriate for the volume-limited sample L050 in Schuecker et al. (2001), with $L_{min} = 2.55 \times 10^{43} {\rm h}_{70}^{-2} erg\ s^{-1}$ and mean redshift $z = 0.04$. We do not take into account any redshift dependence of the bias, which will be small for this sample.

Figure 3.4 plots contours of $b_{\rm eff}$ for slices within the model parameter space centered on the best-fit location of the SS model in Figure 3.2. As p increases, the

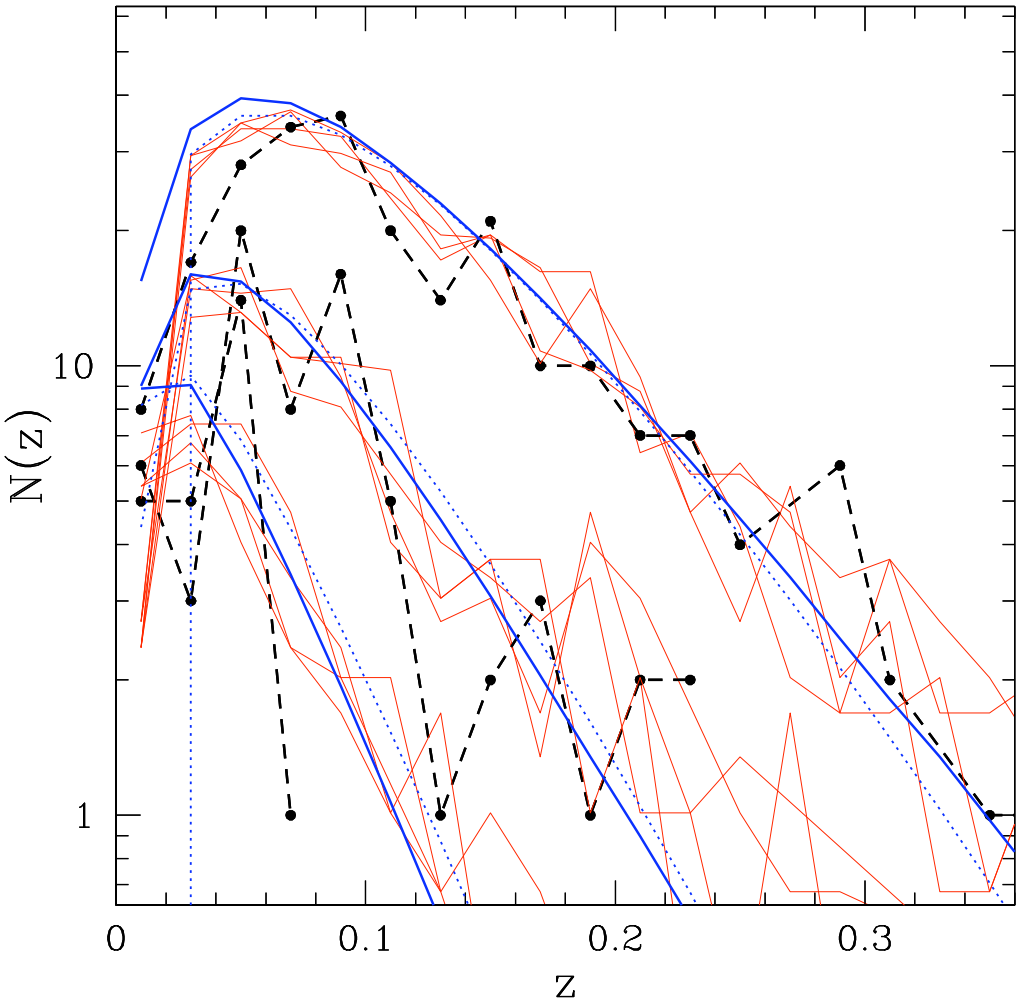

Figure 3.3. Differential counts in redshift for three flux ranges (from upper to lower): $4 \leq f < 10$, $10 \leq f < 25$, and $f \geq 25 \times 10^{-12}$ erg s^{-1} cm^{-2}. The REFLEX data are plotted as filled circles, while the counts expected from the best-fit SS (solid) and NE (dotted) models are shown as continuous lines. Light solid lines for each flux range show discrete realizations using discrete mock sky catalogs and the best-fit SS model.

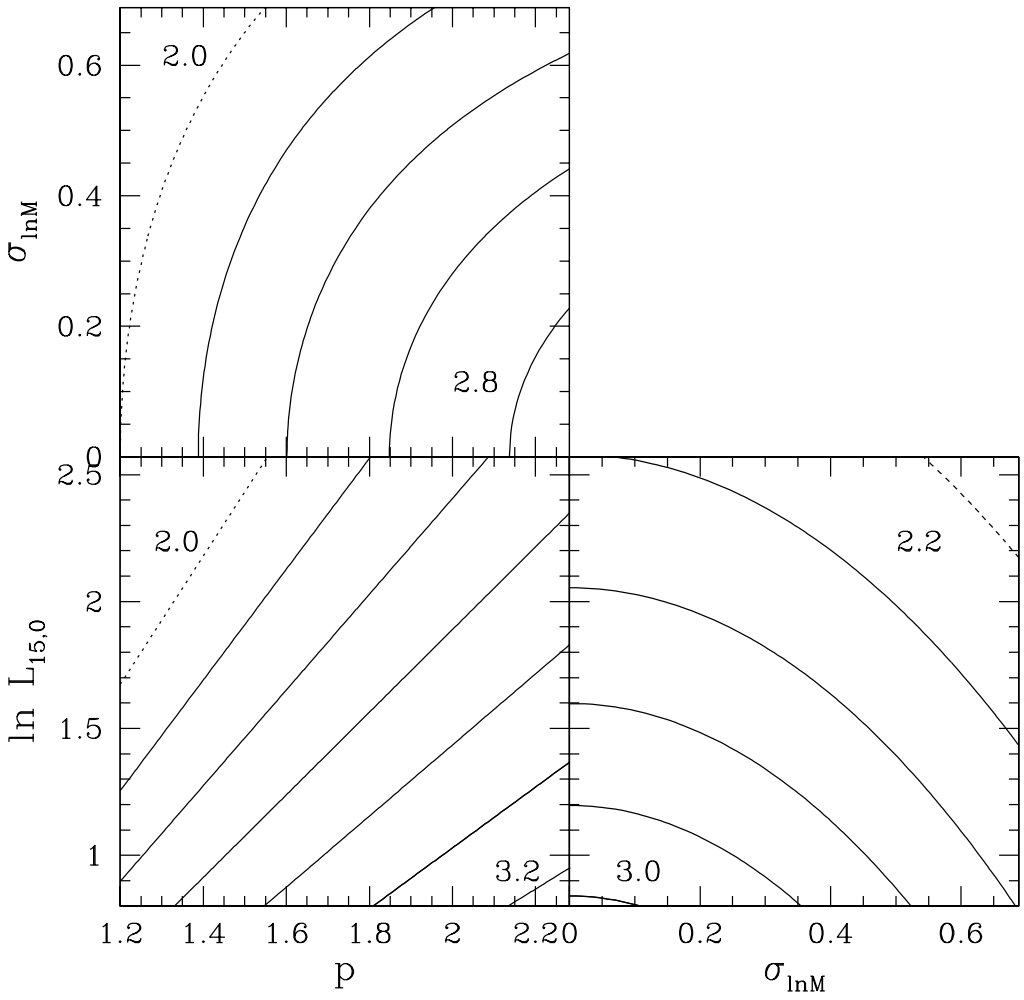

Figure 3.4. Contours of the effective bias $b_{\rm eff}$ are shown in slices through parameter space at the SS best-fit location of Fig 3.2. Contours are spaced by 0.2.

range of halo masses sampled decreases, implying a higher minimum mass scale and therefore an increasing bias. The effective bias decreases as $\ln L_{15,0}$ increases due to the fact that lower mass halos satisfy the flux limit. Finally, increasing $\sigma_{\ln M}$causes a decline in the effective bias, because increased scatter adds lower-mass halos at a fixed luminosity.

The power spectrum and uncertainties published for this sample by Schuecker et al. (2001) imply a prior on the effective bias of $b_{\rm eff} = 3.0 \pm 1.0$ for a concordance cosmology. As shown in Figure 3.4, the 1σ uncertainty on the effective bias nearly fills the parameter space we are considering. Because of the large uncertainty, adding the bias constraint does not significantly improve the fits from counts alone. More precise measurement of the clustering bias will require deeper surveys that better probe the high mass/high bias portion of mass function.

3.3.3 Scatter in the Luminosity-Temperature Relation

We next derive information on the mass variance $\sigma^2_{\ln M}$ from the intrinsic scatter of the temperature–luminosity relation. Figure 3.5 shows the T-L relation for 106 HIFLUGCS clusters published by RB02, with temperatures obtained from various original sources. We fit the relation to a power law, including the stated errors in temperature, and then measure the intrinsic variance $\sigma^2_{\ln T|L}$ by subtracting the measurement error contribution from the total variance. We bootstrap over the quoted errors on the temperatures to estimate the uncertainty in the intrinsic dispersion, with the result $\sigma_{\ln T|L} = 0.25 \pm 0.03$. While there are other cluster surveys with luminosity and temperature data (Horner, 2001; Ikebe et al., 2002), we use temperatures from RB02, to be consistent throughtout the paper.

To include the measured T-L scatter in the analysis, consider a mass-limited ensemble of co-eval halos with masses, X-ray spectral temperatures and soft X-ray luminosities $\{M_i, T_i, L_i\}$. Motivated by the virial theorem, and mirroring the case for luminosity, we assume that T and M are related by a power-law with log-normal scatter, and write $\overline{\ln T} = \ln T_{15} + q \ln M$. Any given halo will, in general, deviate from the mean L-M and T-M scalings. The $i^{\rm th}$ cluster's true mass $\ln M$ will deviate from the

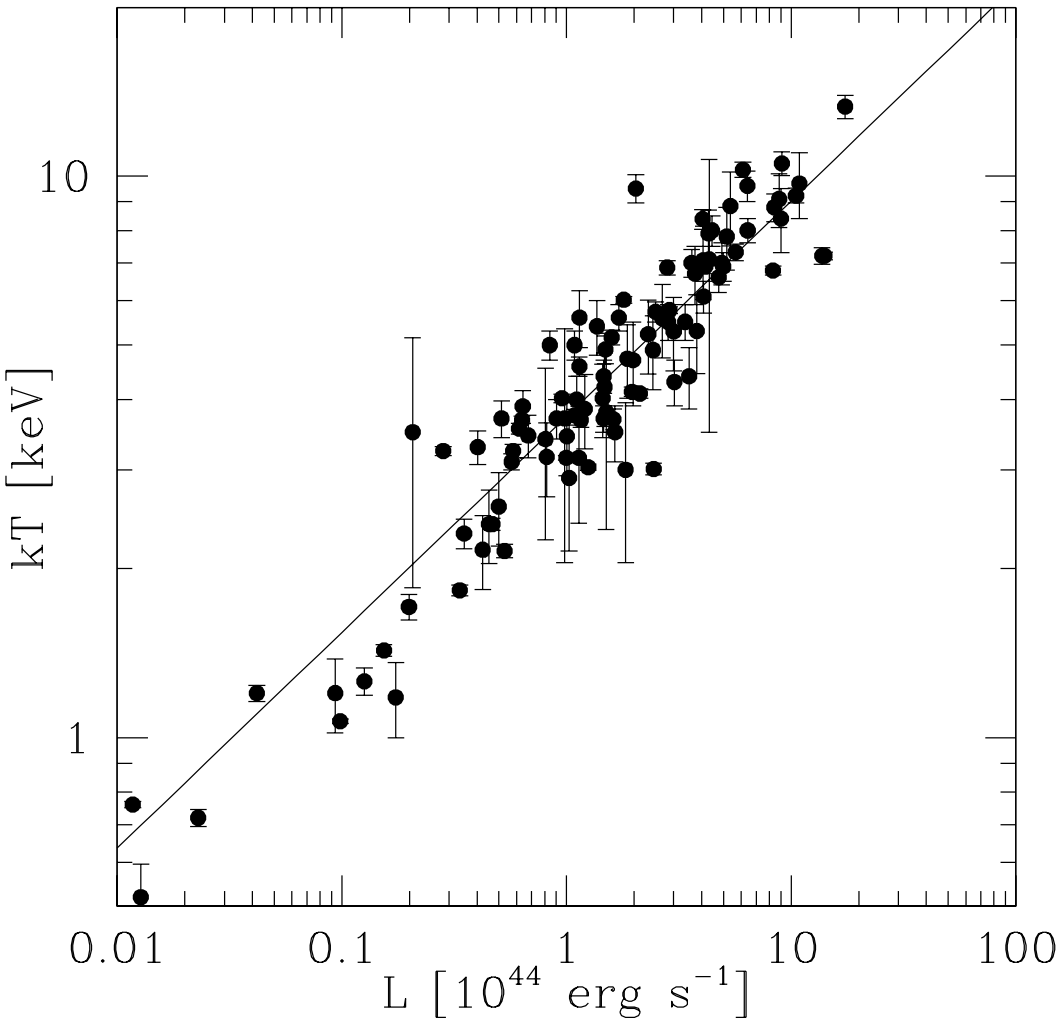

Figure 3.5. The T-L relation for HIFLUGCS clusters from Reiprich & Böhringer (2002). Error bars indicate the observed 1σ uncertainties in the temperature measurements.

values inferred by inverting the log-mean relations for its temperature and luminosity

$$\ln M = \frac{1}{q}\ln\left(\frac{T}{T_{15}}\right) + \delta_T^M, \tag{3.19}$$

$$\ln M = \frac{1}{p}\ln\left(\frac{L}{L_{15}}\right) + \delta_L^M. \tag{3.20}$$

The halos temperature and luminosity are then related by

$$\ln T = \frac{q}{p}\ln L + \ln T_{15} - \frac{q}{p}\ln L_{15} + q(\delta_L^M - \delta_T^M), \tag{3.21}$$

so, considering a subset of halos of fixed luminosity L, the expected T-L relation is

$$\langle \ln T \rangle = \frac{q}{p}\ln L + C, \tag{3.22}$$

where $\langle\,\rangle$ represents an average at fixed luminosity. The intercept $C = \ln T_{15} - \frac{q}{p}\ln L_{15} + q[\langle\delta_L^M\rangle - \langle\delta_T^M\rangle]$ will be biased from the zero-scatter expectation if the mean mass deviations based on temperature and luminosity do not cancel, $\langle\delta_T^M\rangle \neq \langle\delta_L^M\rangle$.

The second moment $\langle(\ln T - \langle\ln T\rangle)^2\rangle$ of the observed T-L relation yields

$$\sigma^2_{\ln T|L} = q^2\Big[\langle(\hat{\delta}_L^M)^2\rangle - 2\langle\hat{\delta}_L^M\,\hat{\delta}_T^M\rangle + \langle(\hat{\delta}_T^M)^2\rangle\Big], \tag{3.23}$$

where $\hat{\delta}_L^M \equiv \delta_L^M - \langle\delta_L^M\rangle$ and $\hat{\delta}_T^M \equiv \delta_T^M - \langle\delta_T^M\rangle$ are deviations from the sample means, again at fixed luminosity.

We show below that flux-limited samples are biased in favor of low-mass halos $\langle\delta_L^M\rangle < 0$, but we also find that the measured mass variance in mock HIFLUGCS samples is nearly unbiased relative to a complete, mass-limited sample. We therefore assume $\sigma^2_{\ln M|L} = \langle{\hat{\delta}_L^M}^2\rangle$. Noting that the variance of our underlying model is $\sigma^2_{\ln M} = \sigma^2_{\ln M|L}$, then equation (3.23) can be rearranged to give

$$\sigma^2_{\ln M} = \frac{\sigma^2_{\ln T|L}}{q^2} - \sigma^2_{\ln M|T} + 2\langle\delta_L^M\,\delta_T^M\rangle. \tag{3.24}$$

This equation links the variance in mass at fixed luminosity to an observable quan-

tity, the T-L variance $\sigma^2_{\ln T|L}$, along with other terms that are not directly observable. To evaluate these terms, we turn to an ensemble of 68 cluster simulations evolved under a 'preheated' assumption (Bialek & Evrard, 2006). Like previous simulations (Evrard et al., 1996; Bryan & Norman, 1998; Mathiesen & Evrard, 2001a; Borgani et al., 2004; Rasia et al., 2004), these models respect the virial scaling between temperature and mass, displaying a logarithmic mean relation $T \propto M^{0.58\pm0.02}$ that is slightly shallower in slope than the self-similar value of 2/3 due to the enhanced effects of the raised initial entropy on low mass systems. To approximate actual temperature estimates, the temperature T is determined from fitting mock X-ray spectra of each simulated cluster, assuming emission from a plasma enriched to 0.3 solar metallicity.

Figure 3.6 shows the frequency distribution of the residuals in mass estimates based on inverting the mean virial relation for the 68 clusters sampled at six low-redshift epochs, $z = 0.290$, 0.222, 0.160, 0.102, 0.49 and 0. The distribution of logarithmic deviations is very close to Gaussian, with dispersion $\sigma_{\ln M|T} = 0.19$. This small scatter is empirically supported by the work of Mohr et al. (1999), who find $\sim 17\%$ scatter in M_{ICM} at fixed temperature.

We use data from the same models to examine the covariance in the M-L and M–T deviations, shown in Figure 3.7. The simulations display weak covariance $\langle \delta_T^M \, \delta_L^M \rangle = 0.017$. The weak coupling presumably arises because T and L are sensitive to processes operating on different scales and because the effects of multiple mergers, rather than a single dominant encounter, are driving the halo dynamics at most times. This finding may seem at odds with results from binary merger simulations by Ricker & Sarazin (2001). In the binary case, the luminosity and temperature rise and fall in concert as the mass increases during the merger, suggesting strong covariance. However, recent cosmological simulations by Rowley et al. (2004) show complex evolution in L and T during cluster evolution that is more aligned with the results of Figure 3.7.

With these estimates in hand, and with $\sigma_{\ln T|L}$ from the RB02 data, we find the

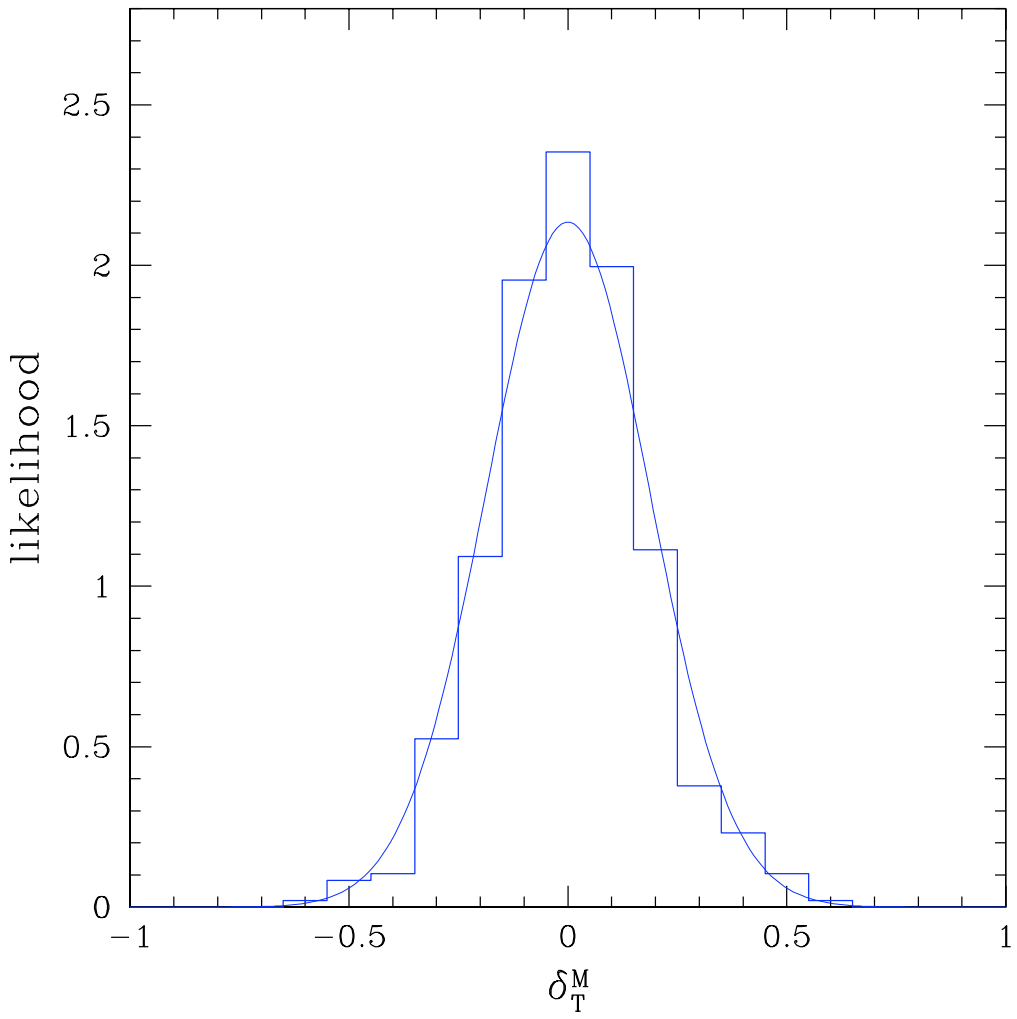

Figure 3.6. The histogram shows deviations in (natural) log mass from mean power-law fits to the $M - T$ relation from 68 preheated cluster simulations (Bialek & Evrard, 2006). The solid line shows a Gaussian fit with zero mean and dispersion of 0.19

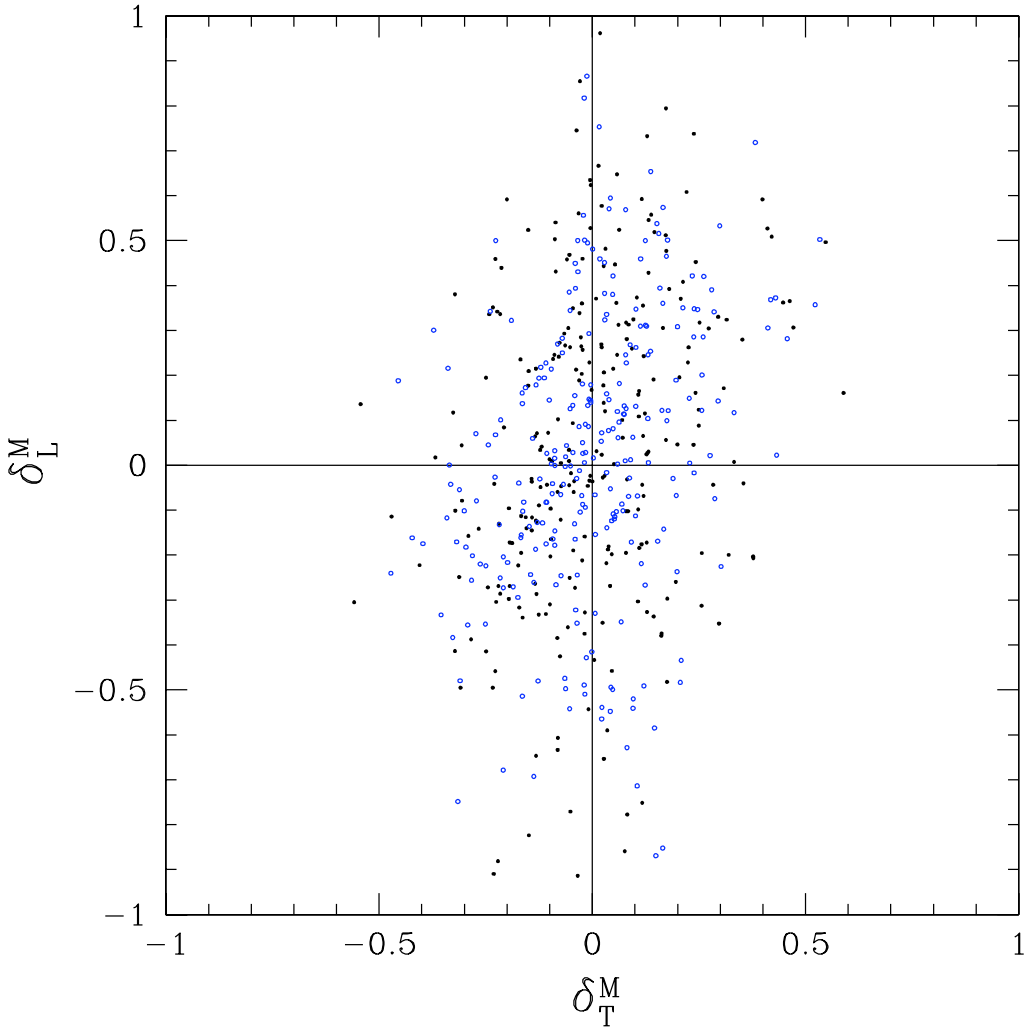

Figure 3.7. The correlation of residuals in log mass about the mean M-T and M-L relations derived from 68 preheated cluster simulations (Bialek & Evrard, 2006) at epochs $0 < z < 0.2$ (filled circles) and $0.2 < z < 0.3$ (open circles).

scatter in mass at fixed luminosity from equation (3.24) to be

$$\sigma_{\ln M} \;=\; 0.43 \pm 0.06, \tag{3.25}$$

where we have assumed a T-M slope $q = 0.58 \pm 0.05$, equivalent to $M \propto T^{1.72 \pm 0.12}$. The slope uncertainty, along with the intrinsic T-L scatter measurement error, dominate the uncertainty in $\sigma_{\ln M}$. Note that a self-similar T-M scaling, $q = 2/3$, leads to a 1σ reduction in scatter, $\sigma_{\ln M} = 0.37$.

3.3.4 Full Constraint Results

Adding the constraint of equation (3.25), along with the effective bias, to the analysis produces the marginalized likelihoods plotted in Figures 3.8 and 3.9. This analysis yields values $p = 1.59 \pm 0.05$, $\ln L_{15,0} = 1.34 \pm 0.09$, and $\sigma_{\ln M} = 0.37 \pm 0.05$. These values are strongly dependent on the scatter constraint, and thus depend on the measurements of temperature, luminosity, and their quoted errors, all of which determine $\sigma_{\ln T|L}$.

The solid circle in Figure 3.8 shows parameter values from RB02. Because the published values assumed $\Omega_m = 1$, we have made small (typically few percent) corrections to convert their luminosity and mass estimates to a concordance cosmology. Under an isothermal profile assumption ($\rho(r) \propto r^{-2}$) used by RB02, the correction to cluster mass scales as $\rho_c^{-1/2}(z)$, while the luminosity scales as $d_L^2(z)$, with d_L the luminosity distance.

Fitting corrected luminosity to mass, we find best-fit values $p = 1.50 \pm 0.08$ and $\ln L_{15,0} = 2.13 \pm 0.12$ for the slope and intercept of the RB02 sample. Subtracting in quadrature the measured mass uncertainties from the scatter in the L-M relation, we find an estimate of the intrinsic scatter, $\sigma_{\ln M} = 0.39$. A formal uncertainty in this estimate is complicated by the fact that there are several sources of scatter, including variance in the hydrostatic mass estimator, that are not easily separated. We defer this exercise to future work. The fact that this estimate of the intrinsic M-L scatter agrees with our model results suggests that the scatter in hydrostatic mass estimates

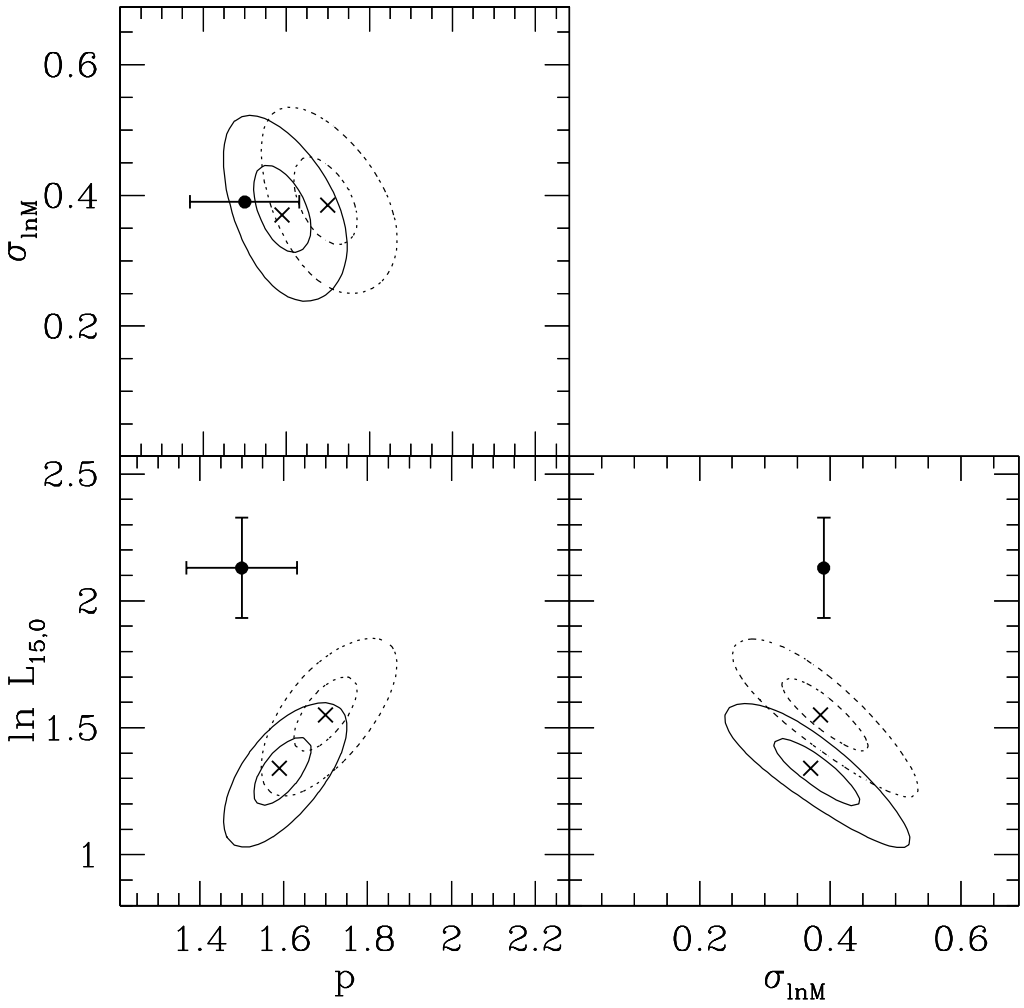

Figure 3.8. Marginalized 68 and 99% confidence intervals are shown after including constraints from clustering bias and from the estimated scatter of equation (3.24). Solid and dotted lines are SS and NE models. Crosses mark the maximum likelihood location. The data point is the RB02 result, shown with 90% confidence error bars on the slope and intercept.

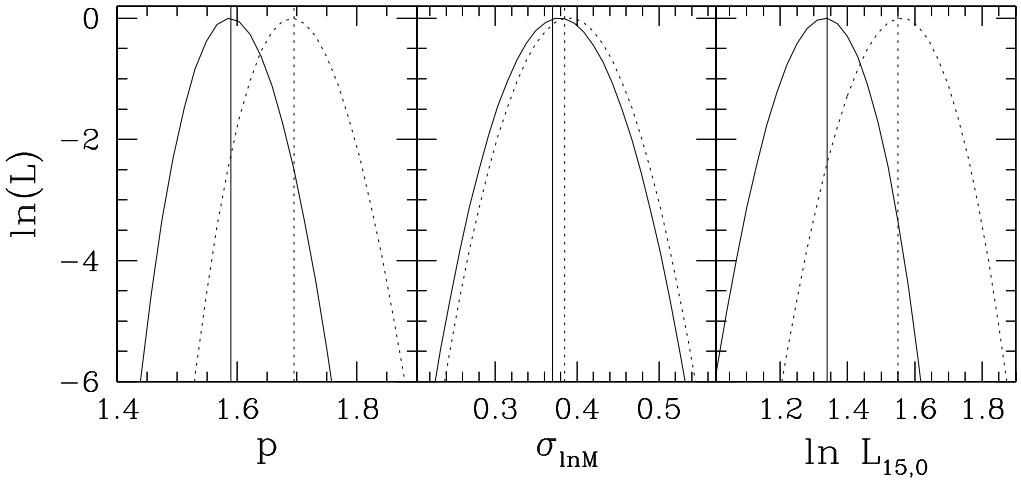

Figure 3.9. One-dimensional, marginalized likelihoods for each model parameter for the SS (solid) and NE (dotted) models after applying the constraints used in Figure 3.8. Vertical lines denote the maximum likelihood location in the full parameter space.

is less than $\sigma_{\ln M}$.

The RB02 normalization result is in serious conflict with the value determined here. We address the main source of this discrepancy, and discuss other implications, in the following section.

Note that the slope, q/p, inferred for the T-L relation via equation (3.22) is 0.36 ± 0.03, in reasonable agreement with the $T \sim L^{0.45\pm0.04}$ displayed by the data in Figure 3.5. A self-similar slope, $q=2/3$, yields better agreement, $q/p=0.42$, but the data do not compel this choice.

As a further comparison of the model and data, we show in Figure 3.10 a binned representation of the luminosity function of the REFLEX data, determined with a $1/V_{\rm max}$ sum described in Böhringer et al. (2001), along with discrete realizations of the function derived from HV mock sky catalogs using the best-fit SS and NE parameters (circles and triangles, respectively). Errors in the binned data include contributions from flux errors and Poisson fluctuations. At low luminosities, the sample variance due to the small volume probed becomes significant. The histogram shows raw REFLEX counts in 0.1 dex luminosity bins.

The mock realizations provide a good match to the REFLEX luminosity function above $\sim 4 \times 10^{43}\,{\rm erg\ s^{-1}}$, where the survey counts per bin exceed ten. At lower luminosities, the models predict higher space densities than those observed. The small numbers of clusters makes it difficult to assess the nature of these differences. It may signal a breakdown in our model, perhaps through a steepening of the slope p at low luminosities. Alternatively, the REFLEX survey may be slightly incomplete at the low luminosity end, which is populated mainly by nearby, extended systems near the survey flux limit. This interpretation is supported by the finding of a 'local void' within $z \lesssim 0.03$ in the cluster spatial distribution (Schuecker et al., 2001). At the bright end, both the observed and model counts decline more slowly than a pure Schechter form, $dn/dL \propto e^{-L/L_*}$.

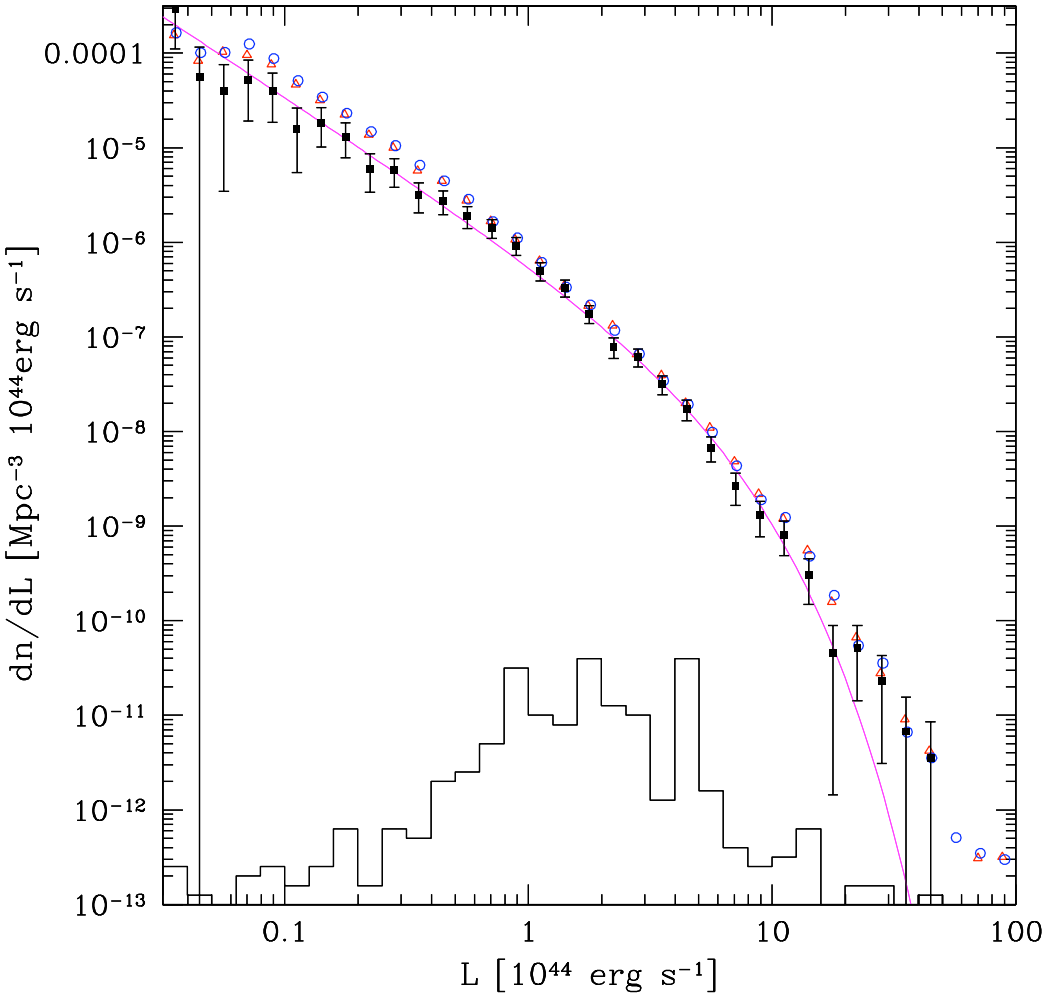

Figure 3.10. The luminosity function of the REFLEX data (filled squares), shown with 1σ uncertainty from Poisson and flux errors, is compared to mock HV sample results using the best fit SS (open circles) and NE (open triangles) parameters from Figure 3.8. The solid line is the Schecter function fit to the luminosity function from Böhringer et al. (2001). The histogram shows raw REFLEX counts in 0.1 dex luminosity bin, using a linear scale of 10 counts per decade.

3.4 Discussion

In this section, we first discuss the source of the discrepancy between the M-L relations derived here and that of RB02. We then briefly explore sensitivity of the model parameters to cosmology, focusing on changes to σ_8 and Ω_m. We then comment on theoretical uncertainty in the mass function, discuss connections to previous REFLEX analysis, and finish with remarks on the accuracy of isothermal beta mass estimates.

3.4.1 Selection Bias from Flux Limit

The results presented in Figure 3.8 indicate that the independent estimate of the luminosity–mass relation from RB02, based on isothermal β-model binding mass estimates, disagrees with the best-fit L-M relation derived above. There is reasonable agreement in the slope and scatter, but the RB02 intercept is substantially brighter than the best-fit values of both the SS and NE model results.

The large discrepancy in $\ln L_{15,0}$ results largely from a classical Malmquist bias expected in flux limited samples such as HIFLUCGS. For a given mass and redshift, a portion of the tail of low-luminosity clusters is lost due to the application of the flux limit. The amplitude of the resultant bias depends on the scatter in the mass-luminosity relation. We first calculate the expected bias analytically, then demonstrate it using mock realizations of flux-limited samples.

With our model, the expected log mean luminosity ($y \equiv \ln L$) as a function of mass ($x \equiv lnM$) for a flux-limited sample is

$$\langle y(x) \rangle = \frac{1}{dN_f(x)} \int dV(z)\, n(x,z)\, Y(x,z) \tag{3.26}$$

$$Y(x,z) = \frac{1}{2}\bar{y}(x,z)\mathrm{erfc}(t_{\min}) + \sqrt{\frac{1}{2\pi}}\sigma_y e^{-t^2_{\min}} \tag{3.27}$$

where $dV(z)$ is a comoving volume element at redshift z, $t_{\min} = (y_{\min} - \bar{y}(x,z))/\sqrt{2}\sigma_y$, $y_{\min} = \ln L_{\min}(x,z)$, $\bar{y}(x,z) = \overline{\ln L}(x,z)$, and $\sigma_y = \sigma_{\ln L} = p\,\sigma_{\ln M}$. As before, $L_{\min}(x,z) = 4\pi d_L^2(z) f / K(z,T)$ is the K-corrected minimum luminosity required to satisfy the flux limit at redshift z. The normalization $dN_f(x)$ is the differential number of halos of

mass e^x that satifsy the flux limit

$$dN_f(x) \;=\; \frac{1}{2}\int dV(z)\, n(x,z)\, \mathrm{erfc}(t_{\rm min}). \tag{3.28}$$

We employ this model, with the JMF assuming a concordance cosmology with our best-fit SS parameters, to calculate the L-M relation expected for the HIFLUGCS survey, with ROSAT soft-band flux limit $2 \times 10^{-11}\mathrm{ergs}^{-1}\mathrm{cm}^{-2}$. The result is shown as the dashed line in Figure 3.11. The HIFLUGCS sample systematically selects brighter objects at fixed mass, leading to a brightening, by roughly a factor two, in the L-M relation relative to the present epoch relation, shown as the solid line.

The brightening for this high flux sample results mostly from scatter, and not from evolution in the SS model. Figure 3.12 demonstrates this by comparing the increase, relative to $z = 0$, in log mean luminosity, calculated from equation (3.27) for SS and NE models. At low masses and luminosities, the volume probed is small, and there is little evolution in the SS model. Above $10^{14}\, h^{-1}\ \mathrm{M}_\odot$, the survey depth is approaching $z \sim 0.1$, and the SS model bias becomes larger than that of the NE model. As the survey probes to higher redshifts at higher masses, the SS model bias continues to grow up to $M \sim 10^{15}\, h^{-1}\ \mathrm{M}_\odot$. Beyond this mass scale, the bias drops because the number of the most massive halos falls to zero at high redshift. A similar decline is seen in the NE model.

In addition to the analytic calculation, we also create mock realizations of the HIFLUGCS sample using HV sky survey samples. We assign a luminosity and temperature to each halo in a manner consistent with our best-fit model, and apply the flux cut to K-corrected fluxes. The result for one random realization is shown as filled circles in Figure 3.11. The points scatter about the analytic expectation with *rms* deviation of $\sigma_{\ln L} = 0.63$, close to the input (mass-limited) scatter of 0.59. Due to the finite size of the HIFLUGCS sample, the degree of bias will vary from the analytic expectation. We estimate this variance using 200 Monte Carlo realizations of HV mock samples, derived from the MS and VS sky surveys (Evrard et al., 2002), adjusted to a sky area of 5.5 str to match the cluster counts in RB02. From this

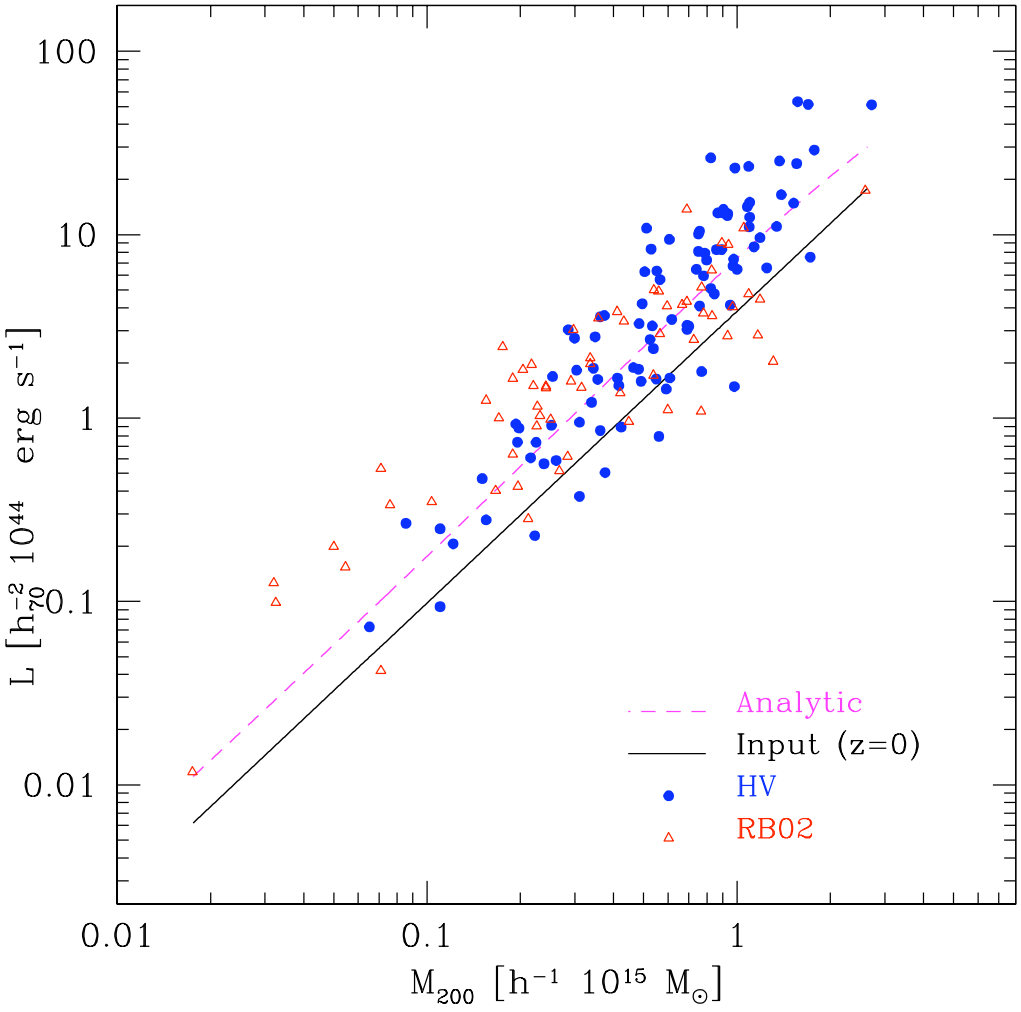

Figure 3.11. The best fit SS model relation between rest-frame, soft X-ray luminosity and mass at $z = 0$ (solid line) is compared to the relation expected from a HIFLUCGS flux-limited sample (dashed line), computed from equation (3.27). Triangles show the HIFLUGCS data while filled circles show an HV mock version of these data.

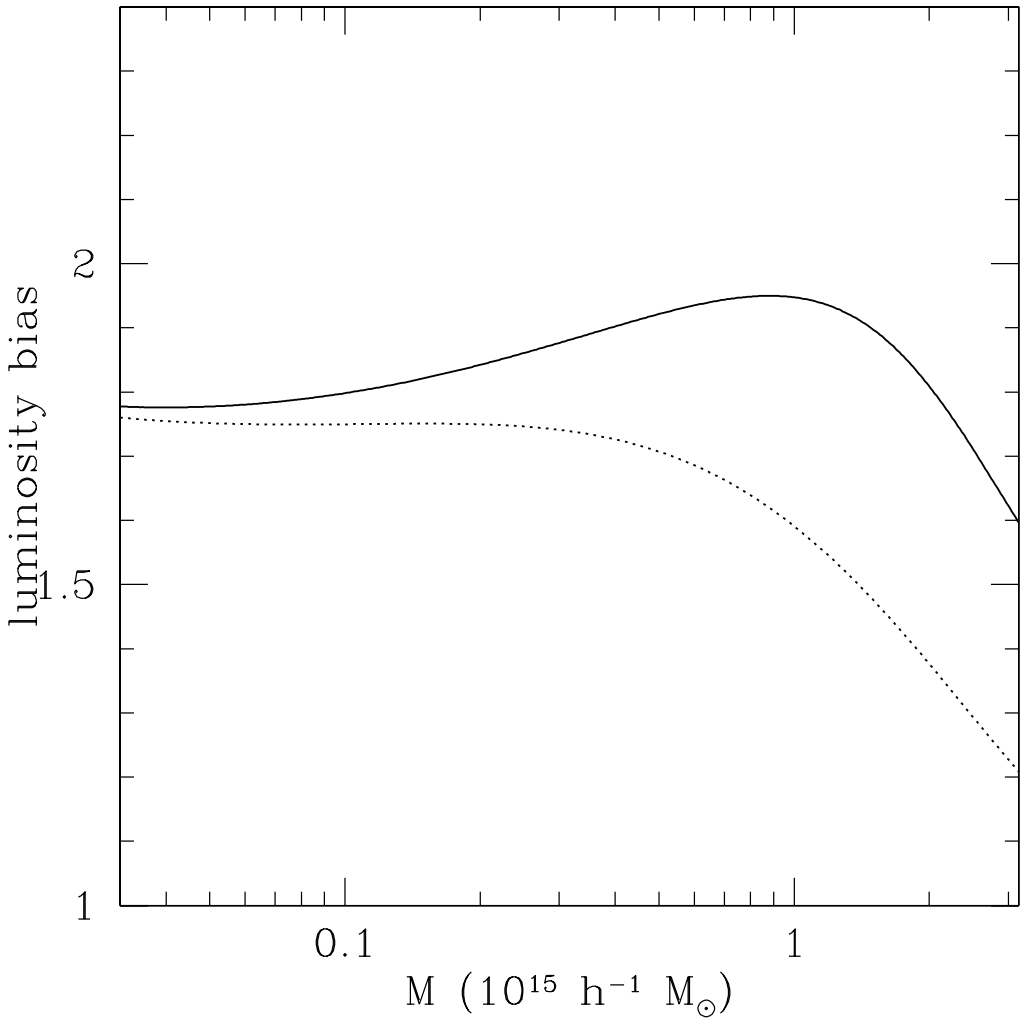

Figure 3.12. The ratio between the logarithmic mean luminosity of a flux-limited sample and the $z=0$ relation is shown for the best-fit SS (solid) and NE (dotted) models. The difference in the two models is the result of redshift evolution, which is more important for higher mass halos that satisfy the sample flux limit at larger distances.

exercise, we derive correction terms of -0.70 ± 0.11 to $\ln L_{15,0}$ and -0.06 ± 0.07 to p. The correction terms strongly depend on the degree of scatter in the L-M relation.

3.4.2 Degeneracy and Cosmology

The normalization $\ln L_{15,0}$, amount of scatter $\sigma_{\ln M}$, and power spectrum normalization σ_8 are strongly coupled parameters that control the number counts. In the current approach, we determine the scatter via measurement of variance in the L-T relation, using input from simulations in a manner described in §3.3.3. The rather large scatter in luminosity for halos of a given mass, $\sigma_{\ln L} = 0.59$, implies the signficant Malmquist bias discussed above. Previous analysis of the REFLEX cluster abundance and power spectrum (Schuecker et al., 2001, 2003) assumed a much smaller level scatter, $\sigma_{\ln L} \sim 0.2 - 0.3$, based on the impression that the main contribution to the L-M scatter derived in RB02 was large uncertainty in the binding mass measurement. With the smaller assumed scatter, no Malmquist bias correction was applied, so the value of $\ln L_{15,0}$ employed was higher, and the corresponding value of σ_8 lower, compared to the values used here. This approach has recently been emphasized by (Reiprich, 2006).

The set of parameters allowed by Figure 3.8 assumes a concordance cosmological model described in § 3.1. We now explore the sensitivity of the best-fit location to changes in cosmological parameters (Ω_m, σ_8), under a flat-metric assumption. In particular, we focus below on the world model favored by year-three WMAP analysis (Spergel et al., 2006), which involves a lower normalization $\sigma_8 = 0.76 \pm 0.05$ and matter density $\Omega_m = 0.234 \pm 0.035$.

The left panel of Figure 3.13 shows how the results of our likelihood analysis change as the cosmology is varied. The dotted and dashed lines show 68 and 99% marginalized contours for $\Omega_m = 0.24$ and $\Omega_m = 0.36$, respectively. The power spectrum normalization is varied to keep $\sigma_8^2 \Omega_m$ constant, a condition that roughly holds fixed the number of halos above $\sim 2 \times 10^{14}\, h^{-1}\ \mathrm{M}_\odot$ (Efstathiou, Frenk & White 1993; Viana & Lyddle 1998). The vacuum energy density $\Omega_\Lambda = 1 - \Omega_m$ is adjusted to maintain a flat metric. The shape of the filtered power spectrum $\sigma(M)$ is determined from

Ω_m	$\ln L_{15,0}$	p	$\sigma_{\ln M}$
0.24	1.19 ± 0.08	1.46 ± 0.04	0.39 ± 0.05
0.30	1.34 ± 0.09	1.59 ± 0.05	0.37 ± 0.05
0.36	1.46 ± 0.11	1.71 ± 0.05	0.37 ± 0.05

Table 3.2. Self-Similar Model Parameters for Different Cosmologies

CMBFAST (Seljak & Zaldarriaga, 1996) and we use equation (11) of Evrard et al. (2002) to adjust the constants $A(\Omega_m)$ and $B(\Omega_m)$ in the JMF. Parameter values are listed in Table 3.1.

The constraint from the observed scatter in the T-L relation ties the best-fit location to a narrow range of $\sigma_{\ln M}$. However, as Ω_m increases, the slope of the mass function steepens, and the best fit value of p must increase as a result. We find that the slope scales roughly as $p \propto \Omega_m^{0.5}$, being reduced to $p = 1.46 \pm 0.04$ for $\Omega_m = 0.24$ and increased to 1.71 ± 0.05 for $\Omega_m = 0.36$ for the case of SS evolution. Table 3.2 lists the best fit SS parameters for these cosmologies.

For the most massive and X-ray luminous halos, a change of normalization σ_8 produces a nearly constant shift in the mass function in the mass direction, such that the mass M_* at fixed space density n_* scales as $M_* \propto \sigma_8^{1/\alpha'}$, with $\alpha' = 0.4$ above $\sim 2 \times 10^{14}\ h^{-1}\ \mathrm{M}_\odot$ (Evrard et al., 2002). Since observations fix the luminosity at n_*, variations in σ_8, and hence the mass scale M_*, can be compensated by adjusting the normalization $L_{15,0} \propto M_*^{-p}$. We therefore expect $L_{15,0} \propto \sigma_8^{-p/\alpha'}$. With $\alpha' \simeq 0.4$, and $p \simeq 1.6$, the characteristic luminosity should have strong sensitivity to the power spectrum normalization, $L_{15,0} \propto \sigma_8^{-4}$.

The open symbol in the left panel of Figure 3.13 shows the RB02 result, after correction for the flux bias described in the preceding section. Error bars have been enlarged by adding in quadrature the scatter in the corrections derived from the mock HV Monte Carlo analysis. The corrected results lie very close to the values determined here.

The right hand panel offers a compromise model driven by cosmological parameters from the WMAP Year 3 data (Spergel et al., 2006). The model assumes a flat metric with $\Omega_m = 0.24$ and a slightly elevated normalization $\sigma_8 = 0.85$, along with

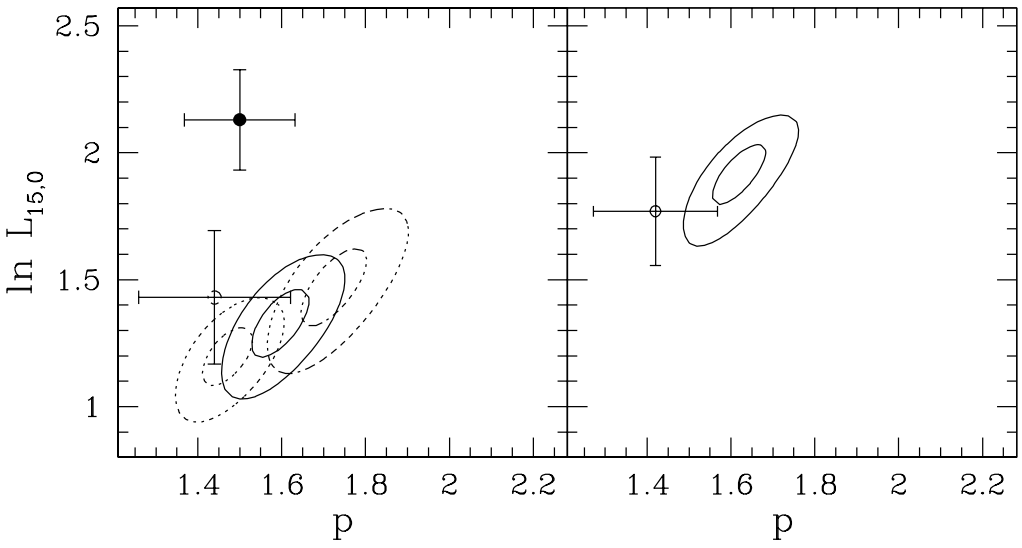

Figure 3.13. The left panel plots 68 and 99% confidence intervals of the slope and normalization for $\Omega_m = 0.24$, 0.3 and 0.36 (left to right), with $\Omega_m {\sigma_8}^2$ constant, after applying the joint constraints on counts, clustering, and $\sigma_{\ln M}$ scatter. The solid point in the left panel plots the original RB02 result, with 90% error bars. The right panel plots 68 and 99% confidence intervals of the slope and normalization for the WMAP compromise cosmology, $\Omega_m = 0.24$, $\sigma_8 = 0.85$, after applying the joint constraints on counts, clustering, and a lower $\sigma_{\ln M} = 0.25$ scatter. In both panels, the open point gives the RB02 result after correcting for the flux cut bias, with 90% error bars that include the variance of HV Monte Carlo realizations discussed in the text.

a reduced estimate of the scatter $\sigma_{\ln M} = 0.25 \pm 0.06$. The resulting best fit parameters are $p = 1.60 \pm 0.05$, $\sigma_{\ln M} = 0.21 \pm 0.06$, and $\ln L_{15,0} = 1.92 \pm 0.08$. The lower scatter leads to a smaller Malmquist bias for the RB02 sample, we derive corrections of -0.36 ± 0.05 to $\ln L_{15,0}$ and -0.08 ± 0.04 to p. The corrected RB02 result is then $p = 1.42 \pm 0.09$, $\ln L_{15,0} = 1.77 \pm 0.13$, and is plotted in the right-hand panel in Figure 3.13.

We concur with the analysis by Reiprich (2006) that a zero-scatter solution with $\sigma_8 = 0.76$ provides good agreement with the original RB02 result, but we feel that a zero-scatter solution is unphysical. The large variance in the observed T-L relation has been tied to variations in core emission (Fabian et al., 2006; O'Hara et al., 2006). Maintaining a tight L-M relation would require a strong coupling between core gas physics and total halo mass, as well as a large scatter in the virial (T-M) relation. These outcomes are neither anticipated theoretically nor supported by the current generation of numerical simulations.

3.4.3 Theoretical Uncertainty

Our model rests on the calibration of the M_{200} halo space density (Evrard et al., 2002). A full treatment of the theoretical error in the mass function is beyond the scope of this paper, but we comment here on the impact of normalization uncertainties in $n(M, z)$ on the $\ln L_{15,0}$ parameter.

Simulations by Hu & Kravtsov (2003b) find agreement with the form we employ at better than ten percent in number over the mass range $5 \times 10^{13} - 10^{15}\ h^{-1}\ \mathrm{M}_\odot$ (see their Fig. B10). The JMF calibration using percolation, rather than spherical overdensity, masses has been confirmed at the five percent level in number by Warren et al. (2005) using a set of sixteen 1024^3-particle simulations. That work proposes a slightly more complex formulation to replace our use of equation (3.6), but the difference at high masses is only a few percent in number (see their Fig. 2).

These results appear to indicate that the current calibration uncertainty in the halo space density is at the level of $\sim 5\%$ in number. For massive, X-ray luminous halos, where locally $d\ln n / d\ln M \simeq -3$, this translates into an error in mass scale of

$\sim$2%, or an additional $\sim$0.03 uncertainty in $\ln L_{15,0}$.

However, Warren et al. (2005) also find that one out of four non-concordance simulations shows a larger discrepancy with the model expectations, roughly 20% in number. Considering that this is one outlier out of 20 simulations, and given that the remaining N-body data show much better consistency, we feel that a 15% uncertainty in number density is a conservative upper limit on the theoretical error. This implies a maximum additional uncertainty in $\ln L_{15,0}$ of ~ 0.08. The theoretical uncertainty is most likely smaller than, or, at worst, comparable to, the statistical error of 0.09.

The use of M_{500} as a mass measure is not expected to affect the theoretical uncertainties. Assuming an NFW mass profile, Appendix B of Evrard et al. (2002) calculates a simple shift to the mass scale. Shifting the mass scale results in a shift of the JMF, and our normalization parameter would likewise be translated.

3.4.4 Accuracy of Hydrostatic Mass Estimates

The isothermal β-model masses employed by RB02 are determined by fitting the azimuthally-averaged X-ray surface brightness to derive the gas density profile under the assumption of isothermality for the intracluster gas. Simulations indicate that this approach may yield masses that are biased by up to a few tens of percent (Evrard, 1990; Schindler, 1996; Navarro et al., 1995; Evrard et al., 1996; Rasia et al., 2004, 2006), but the computational expectations are rendered uncertain by incomplete modeling of ICM physics and by systematic errors associated with determining the spectral temperature derived from the thermally complex intracluster medium of simulated clusters (Mathiesen & Evrard, 2001b; Mazzotta et al., 2003; Vikhlinin et al., 2005). The uncomfortably wide range of inferred mass–temperature relations from theory and observations (*cf.,* Table 1 of Pierpaoli et al. (2003), Table 3 of Henry (2004) and Table 1 of Evrard (2004)) is another reason for caution regarding the accuracy of cluster mass estimates.

From Figure 3.13, it is apparent that implied errors in hydrostatic masses will be model-dependent. For the concordance model with $\sigma_8 = 0.9$, there is little error in normalization at $10^{15}\,h^{-1}$ $\mathrm{M}_\odot$ after taking the flux bias into account. For the WMAP

cosmology, we tuned agreement in the right panel of Figure 3.13 by choosing $\sigma_8 = 0.85$ and $\sigma_{\ln M} = 0.25$. For a power spectrum normalization of $\sigma_8 = 0.76$, our normalization $\ln L_{15,0}$ is brighter than the RB02 result by a factor of 1.5, indicating that hydrostatic masses are overestimates of the true cluster mass by nearly a factor of 2.

Additional independent estimates of the slope and intercept of the L-M relation would help. Weak lensing analysis of joint X-ray and optical samples is a promising approach that has been applied in a preliminary fashion to clusters in the SDSS Early Data Release (Sheldon et al., 2004). The lensing mass estimates require careful calibration to eliminate the effects of projection (Metzler et al., 2001), but either stacking to acheive spherical symmetry (Johnston, 2005) or analysis of mock data from suitably selected simulated clusters (Hennawi & Spergel, 2005) can be used to validate procedures used to extract mass estimates from shear maps. Pedersen & Dahle (2006) examine the M-T relation at the high-mass end using lensing masses from 30 clusters, finding a higher normalization than studies using isothermal masses, and finding a power spectrum normalization of $\sigma_8 \sim 0.88$ for $\Omega_m = 0.3$. The large number statistics offered by nearby optical cluster catalogs from SDSS (Bahcall et al., 2003; Miller et al., 2005; Koester, 2006) and 2dF (Padilla et al., 2004), when matched with existing and forthcoming archival X-ray data, should ultimately be exploited for this exercise.

3.5 Conclusion

We derive constraints on a model that relates soft X-ray luminosity to halo mass and epoch, $p(L|M,z)$, described as a median power-law relation, $L \propto M^p \rho_c^s(z)$, with log-normal scatter of fixed width $\sigma_{\ln L}$. Convolving this with the mass function of a ΛCDM universe, we perform a likelihood analysis on the counts of galaxy clusters in flux and redshift observed in the REFLEX survey for specific cases of self-similar ($s = 7/6$) and no evolution ($s = 0$). A strong degeneracy between the intercept and scatter in the model means that counts place only an upper limit on the degree of scatter in mass at fixed luminosity $\sigma_{\ln M} < 0.4$.

To improve the estimate of the scatter, we apply additional constraints based

on the clustering bias of a volume-limited REFLEX sub-sample and on the intrinsic variance of the observed temperature–luminosity relation. Because the survey probes halo mass scales where the bias is relatively weakly dependent on mass, and because the measured clustering has a substantial uncertainty, the addition of bias has little practical effect on allowed parameters. Using gas dynamical simulations of clusters to probe the inter-relationships of M, T, L, we derive an estimate $\sigma_{\ln M} = 0.43 \pm 0.06$ from the observed scatter in the T-L relation.

After applying these additional constraints, we derive best-fit parameters $p = 1.59 \pm 0.05$, $\sigma_{\ln M} = 0.37 \pm 0.05$, and $\ln L_{15,0} = 1.34 \pm 0.09$ for a concordance cosmology with $\{\Omega_m, \Omega_\Lambda, \sigma_8\} = \{0.3, 0.7, 0.9\}$ and a self-similar evolutionary assumption. The slope and normalization increase, by 2σ and 1σ respectively, under a no evolution assumption. Exploring sensitivity to the assumed (flat-metric) cosmology, we find $\mathrm{L}_{15,0} \sim {\sigma_8}^{-4}$ for fixed Ω_m and $p \sim \Omega_m^{0.5}$ when $\Omega_m {\sigma_8}^2$ is held fixed. When applying a cosmological model guided by WMAP results, $\Omega_m = 0.24$, $\sigma_8 = 0.85$, and a lower constraint on the scatter, we derive best-fit parameters which include a much higher normalization term, $p = 1.60 \pm 0.05$, $\sigma_{\ln M} = 0.21 \pm 0.06$, $\ln L_{15,0} = 1.92 \pm 0.08$.

Our best-fit concordance model result differs from that determined by Reiprich & Böhringer (2002), who used hydrostatic (isothermal-beta model) mass estimates, which are lower in normalization by roughly a factor of two. We show that a bias of this magnitude is expected for the direct L-M relation derived from a flux limited sample, due to a Malquist bias induced by the survey selection process. Correcting for this bias leads to quite good agreement between the two approaches, implying that systematic uncertainties in hydrostatic mass estimates are unlikely to be larger than $\sim 15\%$. To accommodate the change in cosmology preferred by WMAP observations, we offer a compromise solution with slightly elevated σ_8 and lower intrinsic scatter $\sigma_{\ln M}$. Independent approaches to determining the L-M scaling relation, particularly through weak gravitational lensing analysis, should be vigorously pursued.

We anticipate that the approach used here can be fruitfully applied to relations between other observables, such as X-ray temperature or Sunyaev-Zel'dovich decrement, and underlying mass. The coming era of large area, deep cluster surveys,

coupled with increasingly detailed numerical simulations, will drive progress, for example, by allowing the evolutionary parameter s to be directly constrained and by enabling investigation of the detailed form of the likelihood $p(L|M, z)$. Possible future refinements for the latter include adding a non-Gaussian component and/or relaxing the assumptions of constant slope and scatter.

CHAPTER 4

Massive Halos in Millennium Gas Simulations: Multivariate Scaling Relations

4.1 Introduction

Accurate cosmology using surveys of clusters of galaxies requires a robust description of the relations between observed cluster signals and underlying halo mass. Even without strong prior knowledge of the mass-signal relation, cluster counts, in combination with other probes, add useful constraining power to cosmological parameters (Cunha, 2009). However, significant improvements can be realized when the error in mass variance is known (Lima & Hu, 2004b; Cunha et al., 2009). Improvements can also be gained by extending the model to multiple observed signals (Cunha, 2008), especially when an underlying physical model can effectively reduce the dimensionality of the parameter sub-space associated with the model (Younger et al., 2006). The coming era of multiple observable signals from combined surveys in optical, sub-mm and X-ray wavebands invites a more holistic approach to modeling multi-wavelength signatures of clusters.

Signal covariance also characterizes survey selection, in terms of both mass and additional observables. These issues have been recently been examined for the case of X-ray selected samples by Stanek et al. (2006) and Nord et al. (2008). In particular, Nord et al. (2008) show how luminosity–mass variance can mimic apparent evolution in the luminosity–temperature relation when data from deep, X-ray-flux limited samples are compared with shallow, local ones.

Employing a selection observable with small mass variance minimizes such errors. Recent work has shown that the total gas thermal energy, observable via an integrated

Sunyaev-Zeldovich effect (Carlstrom, 2004) or via X-ray imaging and spectroscopy, is a signal that scales as a power-law in mass with only $\sim 15\%$ scatter (White et al., 2002; Kravtsov et al., 2006; Maughan, 2007; O'Hara et al., 2007; Zhang et al., 2008; Jeltema et al., 2008). Still, a full understanding of mass selection properties of a given signal requires knowing the redshift evolution of the slope and intercept of the mean scaling relation, as well as evolution of the signal-mass variance. The redshift behavior of signals is generally not well known empirically, although recent work has begun to probe X-ray luminosity evolution to $z \sim 1$ (Maughan et al., 2006; Vikhlinin et al., 2008).

One can address signal–mass covariance observationally using hydrostatic, virial or lensing mass estimates. For individual clusters, several sources of systematic and statistical error pose challenges. For hydrostatic masses, early gas dynamic simulations (Evrard, 1990; Navarro et al., 1996; Thomas, 1997) suggested that turbulent gas motions forced hydrostatic masses to underestimate true values by $\sim 20\%$. Recent, more sophisticated approaches, with a factor thousand improvement in mass resolution, demonstrate this effect at a similar level in the mean, with $\sim 15\%$ scatter among individual systems Rasia et al. (2006); Nagai (2006); Jeltema et al. (2008). Cluster masses can also be measured by the shear it induces on background galaxies due to gravitational lensing. With this method, individual cluster masses have mass uncertainties $\sim 20\%$ due to the background web (Hoekstra, 2003; de Putter & White, 2005), but large samples can reduce the uncertainty in the mean.

When non-zero signal covariance is present, the mean scaling of stacked samples binned in a selected signal need not be the same as the intrinsic relation. Rykoff et al. (2008a) address this issue using the SDSS maxbcg sample Koester et al. (2007c), an optically-selected set of $\sim 14,000$ clusters for which weak lensing estimates have been made by stacking richness-binned sub-samples (Sheldon et al., 2007; Johnston et al., 2007). By stacking RASS data in the same maxbcg richness bins, Rykoff et al. (2008a) find that the mean scaling of the luminosity–mass relation derived from is consistent at the $\sim 2\sigma$ level with relations derived solely from X–ray data (Reiprich & Böhringer, 2002; Stanek et al., 2006). The expected shift in slope is a product of the local mass

function slope times the covariance in the logarithms of X-ray luminosity and optical richness at fixed mass, and the Rykoff et al. (2008a) result places an upper limit of ~ 0.1 on the latter.

Another approach to studying cluster covariance is to realize populations via numerical simulation. While high resolution treatment of astrophysical processes, including star formation, supernova and AGN feedback, galactic winds and thermal conduction have been included in recent simulations (Dolag et al., 2005; Borgani et al., 2006; Kravtsov et al., 2006; Sijacki et al., 2008; Puchwein et al., 2008), the computational expense has limited sample sizes to typically a few dozen objects or fewer. A detailed study of population covariance requires larger sample sizes, and this can be achieved with lower resolution simulations of large cosmological volumes with reduced physics treatment (Bryan & Norman, 1998; Hallman et al., 2006; Gottlöber & Yepes, 2007).

We take the latter approach in this paper, focusing on the bulk properties of massive halos identified the Millennium Gas Simulations (MGS), a pair of resimulations of the original $500\,h^{-1}$ Mpc Millennium run (Springel et al., 2005), each with 10^9 total particles, half representing gas and half dark matter. The pair of runs use different approaches to the gas physics — a gravity-only (GO) simulation, sometimes called "adiabatic", in which entropy is increased via shocks, and a simulation with preheating and cooling, denoted `PH` . The former ignores galaxies as both a sink for baryons and a source of feedback for the hot intracluster medium (ICM). The latter also ignores the mass fraction contribution of galaxies, but it approximates the feedback effects of galaxy formation by a single parameter, an entropy level imposed as a floor at high redshift (Evrard & Henry, 1991; Bialek et al., 2001; Kay et al., 2007; Gottlöber & Yepes, 2007). Our study focuses on samples of ~ 5000 halos with mass $M > 5 \times 10^{13}\,h^{-1}\,\mathrm{M}_\odot$.

This chapter is organized as follows: in Section 4.2 we discuss the details of the Millennium Gas Simulations and our cluster groupfinding. In Section 4.3 we discuss the mean scaling relations, and we present the second moment of the scaling relations in Section 4.4. Unless otherwise noted, our units of mass are $10^{14}\,h^{-1}\,\mathrm{M}_\odot$, measured

within a sphere of mean density $\Delta_c = 200$.

4.2 Simulations

4.2.1 Millennium Gas Simulations

The Millennium Gas Simulations (hereafter MGS) are a pair of resimulations of the original Millennium (Springel et al., 2005), a high-resolution, dark-matter-only simulation of a $500\,h^{-1}$ Mpc volume. The simulations were run with GADGET-2, as was the Millennium Simulation, treating the gas dynamics with smoothed particle hydrodynamics (SPH) (Springel, 2005b). As described in Hartley et al. (2008), the MGS use the initial conditions of the Millennium simulation, with 5×10^8 dark matter particles, each of mass $1.42 \times 10^{10}\ h^{-1}\ \mathrm{M}_\odot$, and 5×10^8 SPH gas particles, each of mass $3.12 \times 10^9\ h^{-1}\ \mathrm{M}_\odot$, resulting in a mass resolution about 20 times coarser than the original Millennium simulation. The gravitational softening length is $25\,h^{-1}$ kpc. The cosmological parameters match the original: $\Omega_m = 1 - \Omega_\Lambda = 0.25$, $\Omega_b = 0.045$, $h = 0.73$, and $\sigma_8 = 0.9$. While some differences between the simulations are expected due to the difference in mass resolution and gravitational softening length, Hartley et al. (2008) verify the positions of dark matter halos to within $50\,h^{-1}$ kpc between the original Millennium and the MGS. The value of σ_8 is higher than the WMAP3 value (Spergel et al., 2006), but we do not expect it to strongly affect the results of this paper. Shifting σ_8 to a lower value will merely move the halo populations along the axis of the scaling relations.

In this paper we consider two models of the MGS: a gravity-only simulation where the only source of gas entropy change is from shocks, denoted as `GO` , and a simulation with preheating and cooling, denoted as `PH` . The `GO` simulation is useful as a base model that can be easily compared to previous hydrodynamic simulations of galaxy clusters. Furthermore, comparing gravity-only simulations to observations highlights the cluster properties that are strongly affected by astrophysical processes beyond gravitational heating.

While adiabatic simulations match the self-similar prediction for the L-T relation,

$L \sim T^2$, observations show a steeper slope (Arnaud & Evrard, 1999; Osmond & Ponman, 2004). Preheating — the assumption of an elevated initial gas entropy — was introduced by Evrard & Henry (1991) and Kaiser (1991) as a means to resolve this discrepancy. The `PH` simulation is tuned to match X-ray observations of clusters at redshift zero, particularly the luminosity-temperature (L-T) relation (Hartley et al., 2008). The preheating is achieved by boosting the entropy of every gas particle to 200 keV cm^2 at redshift $z = 4$. Although the preheating dominates in the `PH` simulation, there is also cooling based on the cooling function of Sutherland & Dopita (1993). Fewer than 2% of the baryons are converted to stars, however, and star formation is halted by the preheating at $z = 4$. This simple model obviously does not capture all the effects of astrophysical properties in clusters; however, observations at moderate redshifts suggest that the heating of the ICM is dominated by a short-lived burst of star formation at high redshift. Red sequence galaxies in the Spitzer/IRAC Shallow Survey (Eisenhardt et al., 2008) evolve passively to a redshift of $z = 1.4$, agreeing with a star formation model of a short burst of star formation at redshift $z \sim 3$.

4.2.2 Halo Catalog

We identify halos in the simulation by their spherical overdensity, such that halos encompass a region with an average density of $\Delta\rho_c(z)$, where $\rho_c(z)$ is the critical density of the universe, including gas and dark matter. We use halos identified at an overdensity of $\Delta = 200$ for most of our analysis. Halo centers were identified with an N^{th}-*nearest neighbor* approach, which approximates the local density by calculating the distance to the 32^{nd} nearest dark matter particle. The groupfinder begins with the dark matter particle with the highest local density, and works outward in radius particle by particle (including gas and dark matter) until the interior mean density is $200\rho_c(z)$. The algorithm then identifies the densest dark matter particle not already in a halo, and continues iteratively until all overdense regions with more than 100 particles have been identified. Overlapping halos are permitted; however, the center of mass of a halo may not be in another halo.

At redshift zero, in the `PH` simulation we have approximately 220,000 halos with

at least 100 particles, and 4474 over a mass cut of $M > 5 \times 10^{13}\ h^{-1}M_{\odot}$. These numbers are higher in the GO simulation, with approximately 370,000 halos with at least 100 particles, and 5612 over the mass cut of $M > 5 \times 10^{13}\ h^{-1}M_{\odot}$. In Figure 4.1 we plot differential halo counts as a function of total mass from the GO and PH simulations, as well as the prediction from the Tinker mass function (TMF) (Tinker et al., 2008). As discussed in Stanek et al. (2009), preheating causes a decrease in total halo mass of up to $\sim 15\%$ relative to the GO treatment, with the largest effects at lower masses and higher redshifts. While the GO halo space density matches the TMF expectations well, the number of halos in the PH case is lower, especially at lower mass.

Among the halos over the mass cut of $M > 5\times10^{13}h^{-1}M_{\odot}$, we identify overlapping halos. For a pair of overlapping halos, we denote the less massive halo as a "satellite" and the more massive halo as a "primary" halo. For the rest of the analysis in this paper, we exclude the satellite halos. At redshift zero we are left with a sample of 4404 halos in the PH simulation and 5498 halos in the GO simulation.

We repeat the halo finding exercise at all redshifts available for each model. In the case of PH, we employ a total of 63 outputs extending to a redshift of two. For the GO, we analyze only a subset of outputs at redshifts, $z = 0$, 0.5, 1.0 and 2.0. Unless otherwise noted, all of our analysis is for primary halos over the total mass limit of $5 \times 10^{13}\ h^{-1}\ \mathrm{M}_{\odot}$.

4.2.3 Bulk Halo Properties

With the primary halo samples identified, we calculate bulk properties for them that we roughly classify into "structural" and "observable" categories. The former includes dark matter velocity dispersion, ICM mass fraction, gas mass-weighted temperature, and halo concentration while the latter includes X-ray luminosity and spectroscopic-like temperature, thermal Sunyaev-Zel'dovich effect, and a dimensionless ICM emission measure.

With one exception (the ICM mass fraction in the PH model), we model all scaling relations as power-laws with mass, $S = AM^{\alpha}$, normalized at $10^{14}h^{-1}M_{\odot}$. We perform

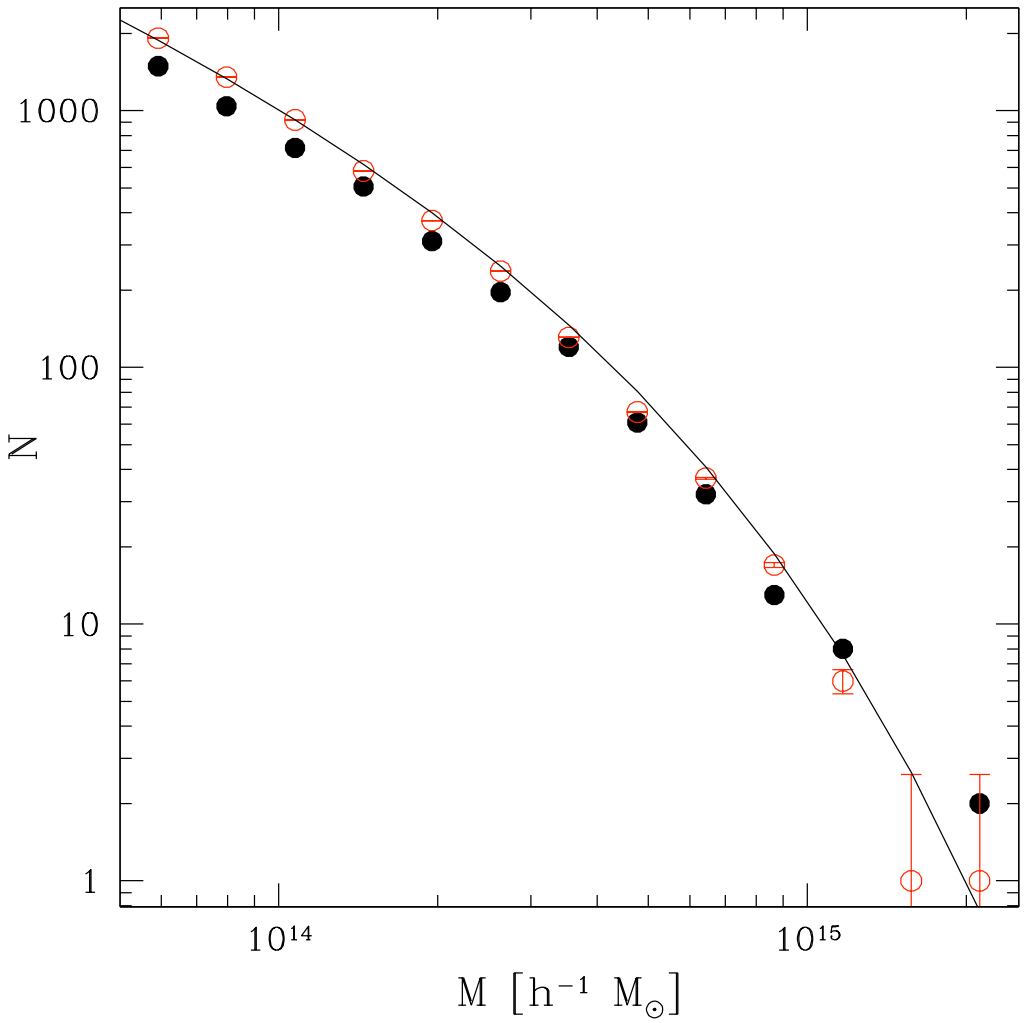

Figure 4.1. Differential counts of halos versus total mass at redshift zero for the PH simulations (filled, black points), the GO simulation (open, red points), and the prediction from the Tinker mass function (Tinker et al., 2008) (solid, black line).

a linear least squares fit to the natural log of the $i^{\rm th}$ signal as a function of mass and redshift, using the form

$$\langle s_i \rangle(\mu, a) = s_{i,14}(a) + \alpha_i(a)\mu, \tag{4.1}$$

where $s_i \equiv \ln S_i$ and $\mu \equiv \ln(M/\,h^{-1}10^{14}M_\odot)$. Brackets represent averaging in narrow mass bins at fixed epoch, so $\alpha(a)$ is the slope and $s_{i,14}(a)$ the normalization of the $i^{\rm th}$ signal at our pivot mass of $10^{14}\,h^{-1}M_\odot$ at redshift, $z = a^{-1} - 1$. For the ICM mass fraction in the PH case, we extend this model to a quadratic with respect to μ. We present mean scalings in §4.3 while deviations from perfect scaling in the form of a signal covariance matrix, $\langle (s_i - \langle s_i \rangle)(s_j - \langle s_j \rangle)\rangle$, are discussed in §4.4.

As the MGS simulations are SPH treatments of the gas, integrals over volume map to summations over all particles, via $\int dV \rho^n \rightarrow \Sigma_i m_i \rho_i^{n-1}$ (Mathiesen & Evrard, 2001b). We consider two measures of ICM temperature. First, we consider the mass-weighted temperature. As GADGET-2 is a Lagrangian simulation with equal mass gas particles, the mass-weighted temperature is simply the average temperature of the particles in the halo:

$$T_m = \frac{1}{M}\int_V dV \rho\, T \rightarrow \frac{1}{N}\sum_i^N T_i. \tag{4.2}$$

We also calculate the spectroscopic-like temperature, $T_{\rm sl}$, as defined in Mazzotta et al. (2004),

$$T_{\rm sl} = \frac{\int n^2 T^{\alpha-1/2} dV}{\int n^2 T^{\alpha-3/2} dV} \rightarrow \frac{\sum_i^N \rho_i T_i^{\alpha-1/2}}{\sum_i^N \rho_i T_i^{\alpha-3/2}}, \tag{4.3}$$

with $\alpha = 0.75$. The spectroscopic-like temperature offers a good match to the temperature derived from a one-component fit to an X-ray spectrum, but is far simpler to compute.

We calculate a total luminosity, assuming that the emission is bremsstrahlung, such that the cooling function $\Lambda(T) \propto T^{1/2}$,

$$L = \int_V dV \rho^2 \Lambda(T) \rightarrow \sum_i^N \rho_i T_i^{1/2} \tag{4.4}$$

. We use MEKAL tables to calculate the luminosity in the three energy bands of XMM: 0.7-2.0 keV, 0.7-5.0 keV, and 0.7-7.0 keV. These tables include both a smooth continuum and emission lines, given the metallicity of the simulation. We also used MEKAL tables to calculate a luminosity in the band [0.1-40.0] keV, which we denote as $L_{\rm bol}$ and use for most of the analysis in this paper.

We also calculate the Y parameter, which is an X-ray measurement that is an analog to the Sunyaev-Zeldovich (SZ) signal, as presented in Kravtsov et al. (2006). From the SZ flux we get a simple approximation

$$Y = \left(\frac{k_B \sigma_T}{m_e c^2}\right) \int_V dV n_e T_e \propto M_{gas} T_m. \tag{4.5}$$

4.2.4 Radial Profile Measures

In addition to bulk cluster properties, we include two measures of cluster structure in our analysis. We measure the halo concentration, c, after fitting an NFW density profile (Navarro et al., 1997) to the radial density profile of the halos. From the form for the density profile

$$\frac{\rho(r)}{\rho_{crit}} = \frac{\delta_c}{(r/r_s)(1+r/r_s)^2}, \tag{4.6}$$

we find halo concentration via

$$\delta_c = \frac{200}{3} \frac{c^3}{[\ln(1+c) - c/(1+c)]}. \tag{4.7}$$

Halo concentration is related to halo formation time (Busha et al., 2007; Wechsler et al., 2002), and can be a measure of how baryonic physics affect the overall halo structure.

We also measure the Q structural parameter, as derived by Arnaud & Evrard (1999), which measures the structural component of the halo luminosity. From the bolometric luminosity,

$$L = \int d^3 r \rho_{gas}^2(r) \Lambda[T(r)], \tag{4.8}$$

where the emissivity scales as temperature $\Lambda(T) \sim T^{1/2}$. Using a scaled radius,

$y = r/r_{\delta_c}$, we can write the radial gas density profile as

$$\rho_{gas}(yr_{\delta_c}) = f_{\rm ICM}\delta_c\rho_c h(y), \tag{4.9}$$

where $h(y)$ is defined as a structure function. This structure function is normalized by $3\int_0^1 dyy^2h(y) = 1$. We can then define a dimensionless emission measure

$$\hat{Q}(T) = (3/4\pi)\int \mathrm{d}^3 y h^2(y), \tag{4.10}$$

which results in a luminosity definition of

$$L \propto {f_{\rm ICM}}^2[M\rho_c\Delta_c\Lambda(T(M,z))]\hat{Q}. \tag{4.11}$$

When looking at the $L-M$ relation, we split up the luminosity into its baryon fraction, temperature, and $\hat{Q}$ components, to compare how these components influence the luminosity between the two simulations.

4.3 Mean Scaling Relations

With the exception of the baryon fractions, we model all scaling relations as a power-law with mass, normalized at $10^{14}\ h^{-1}\ \mathrm{M}_\odot$, with log-normal scatter at fixed mass. In practice, we perform a linear least squares fit to an equation of the form $\ln S = S_{14} + \alpha \ln M$. The scaling relations are fit to the sample of primary halos with $M > 5 \times 10^{13}\, h^{-1}\, \mathrm{M}_\odot$; this sample consists of about 4000 halos at redshift zero. The redshift-zero scaling relations for `PH` and `GO` are presented in Figures 4.2 and 4.5, along with their best-fit power law and their redshift evolution. It is thus easy at a glance to see how bulk cluster properties are affected by the cluster gas physics. The best-fit parameters are presented in Table 4.1, with error bars from Monte Carlo bootstrapping of the sample with replacement. In general, the uncertainties on the best fit parameters are very small, $\sim 0.1\%$ at redshift $z = 0$, and are much smaller than the degree of scatter at fixed mass about the median power law relation. We measure the evolution of the normalization with the form $S_{14}(a) \sim \beta \ln(E(a))$, and

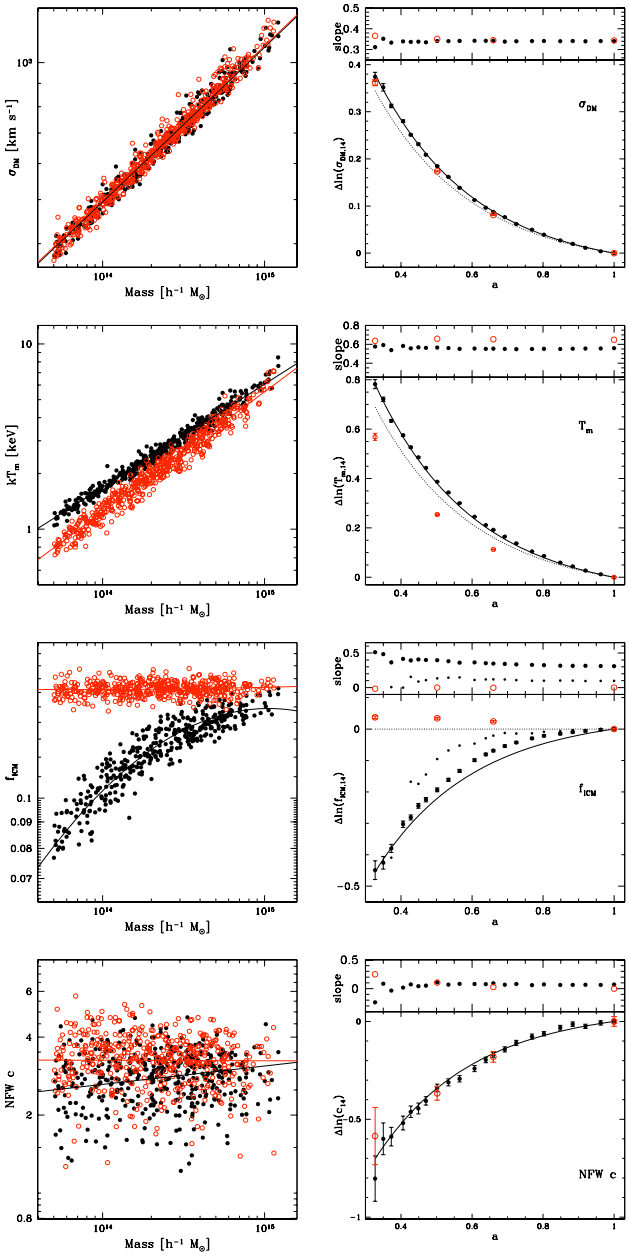

Figure 4.2. Scaling relations at redshift zero and evolution of fit parameters of the structural quantities for the PH (black, filled points) and GO (red, open points) simulations, along with the best-fit scaling relation. The left-hand panels present scaling relations of $\sigma_{\rm DM}$, T_m, $f_{\rm ICM}$, and the NFW concentration c. In the scaling relation panels, we have plotted a random subset, weighted to the low-mass end, making up approximately 10% of the sample. The right-hand panels present the evolution of the slope and the differential evolution of the normalization ($\Delta \ln S$). In the right-hand panels, the solid lines denote the real evolution of the normalization, while the dotted line denotes the self-similar prediction, as listed in Table 4.2. For the evolution of the PH parameters, we plot a subset of time outputs evenly spaced in a.

	PH Simulation		GO Simulation	
Signal	S_{14}	α	S_{14}	α
$\sigma_{\rm DM}$	6.1990 ± 0.0006	0.341 ± 0.001	6.2037 ± 0.0006	0.345 ± 0.001
T_m	0.5121 ± 0.0008	0.559 ± 0.002	0.209 ± 0.001	0.650 ± 0.002
$T_{\rm sl}$	0.605 ± 0.001	0.576 ± 0.002	0.163 ± 0.003	0.576 ± 0.005
Y	-1.781 ± 0.002	1.182 ± 0.003	-1.613 ± 0.002	1.651 ± 0.003
$L_{\rm bol}$	-1.653 ± 0.003	1.868 ± 0.006	0.622 ± 0.005	1.079 ± 0.008
NFW c	0.966 ± 0.005	0.071 ± 0.007	1.181 ± 0.004	-0.002 ± 0.006
$\hat{Q}$	0.461 ± 0.002	0.161 ± 0.003	1.219 ± 0.001	0.030 ± 0.003

Table 4.1. Fit Parameters at redshift zero, fitting on $\ln S = S_{14} + \alpha \ln M$, with mass in units of $10^{14}\, h^{-1}\, {\rm M}_\odot$. The uncertainties are calculated from Monte Carlo sampling with replacement.

we present these results in Table 4.2.

We begin with the fundamental structural quantities in Section 4.3.1, followed by the X-ray and SZ signals in Section 4.3.2. In each section we consider both the redshift zero behavior and the evolution of the mean scaling relations.

4.3.1 Structural Quantities

The fundamental quantities which probe the halo structure and dynamics are the dark matter velocity dispersion, $\sigma_{\rm DM}$, the mass-weighted temperature, T_m, the baryon fraction, $f_{\rm ICM}$, and the NFW concentration, c. We also use the gas velocity dispersion, $\sigma_{\rm gas}$, to probe the total energy budget of the gas. Not all of these quantities are directly observable, but understanding the scaling of these quantities with mass sets the stage for understanding the mass scaling of the observed signals.

Dark matter velocity dispersion. The velocity dispersion of the dark matter particles is a fundamental measure of the dynamic state of a halo. Observationally, the galaxy velocity dispersion should track the dark matter velocity dispersion, with some bias factor (Becker et al., 2007). In both simulations, the scaling of dark matter velocity dispersion with mass is very close to the self-similar prediction, $\sigma_{\rm DM} \propto M^{1/3}$; this in good agreement with the slopes of the simulations presented in Evrard et al. (2008). In both PH and GO , this slope remains constant to high redshift, $z \sim 2$, as seen in Figure 4.2. The normalization, $\sigma_{DM,14}$ agrees well between the two simulations: we find $\sigma_{DM,14} = 496.21\,{\rm km\,s^{-1}} \pm 0.29$ in the GO simulation and $\sigma_{DM,14} = 494.37 \pm 0.31\,{\rm km\,s^{-1}}$ in the PH simulation. This is in good agreement with the result presented in Evrard

et al. (2008), which has a normalization of $\sigma_{DM,14} = 500.2 \pm 6.0\,\mathrm{km\,s^{-1}}$. The evolution of the normalization is slightly steeper than the self-similar prediction verified by Evrard et al. (2008): $\sigma_{\rm DM} \propto [E(z)M]^{1/3}$, with the exact evolution parameters listed in Table 4.2. The consistency in dark matter dynamics at fixed mass, over a range of gas physics, is a good sanity check for the simulations.

Mass-weighted temperature. The mass-weighed temperature, T_m, is a useful probe of the hydrodynamic state of a cluster, and has a low scatter with mass (Evrard et al., 1996; Bryan & Norman, 1998; Borgani et al., 2004). While the slope of the `GO` scaling relation agrees with the virial relation, $T \sim M^{2/3}$, the slope in the `PH` simulation is less steep. As all gas particles receive the same entropy boost at $z \sim 4$ in `PH` , the resultant fractional increase in the characteristic entropy of the halo is higher for low-mass halos than for high-mass halos. This preheating results in a higher normization of the $T_m - M$ relation in the `PH` simulation than in the `GO` . Due to the difference in slope, the T_m of high-mass clusters at fixed mass agrees quite well between the two simulations. Only in lower-mass halos, which are more strongly affected by the preheating processes, do we see up to a $\sim 30\%$ difference in the T_m at fixed mass.

Although the slope of the $T_m - M$ relation in the `GO` simulation agrees with the virial relation, the evolution of the $T_m - M$ relation does not exactly follow the self-similar prediction of $T_m \sim [ME(z)]^{2/3}$ (Kaiser, 1986). The self-similar prediction is for halos in perfect hydrostatic equilibrium, so we examine the contribution of the kinetic energy of the gas. Following Evrard et al. (2008), we define a measure of the kinetic energy content of the gas,

$$\beta_{\rm gas} = \frac{{\sigma_{\rm gas}}^2}{kT_{\rm sl}/\mu m_p}. \tag{4.12}$$

Although the total thermal and kinetic energy of the gas behaves similarly in the two simulations, the behavior of $\beta_{\rm gas}$ varies in the simulations. At a mass scale of $10\,h^{-1}\,\mathrm{M}_\odot$, the mean value of $\beta_{\rm gas}$ in the `GO` simulation is $\beta_{\rm gas} = 0.16$, while in the `PH` simulation it is merely $\beta_{\rm gas} = 0.06$. However, there is significant scatter about the mean, as seen in Figure 4.3. As shown in Rasia et al. (2004), non-zero values of $\beta_{\rm gas}$

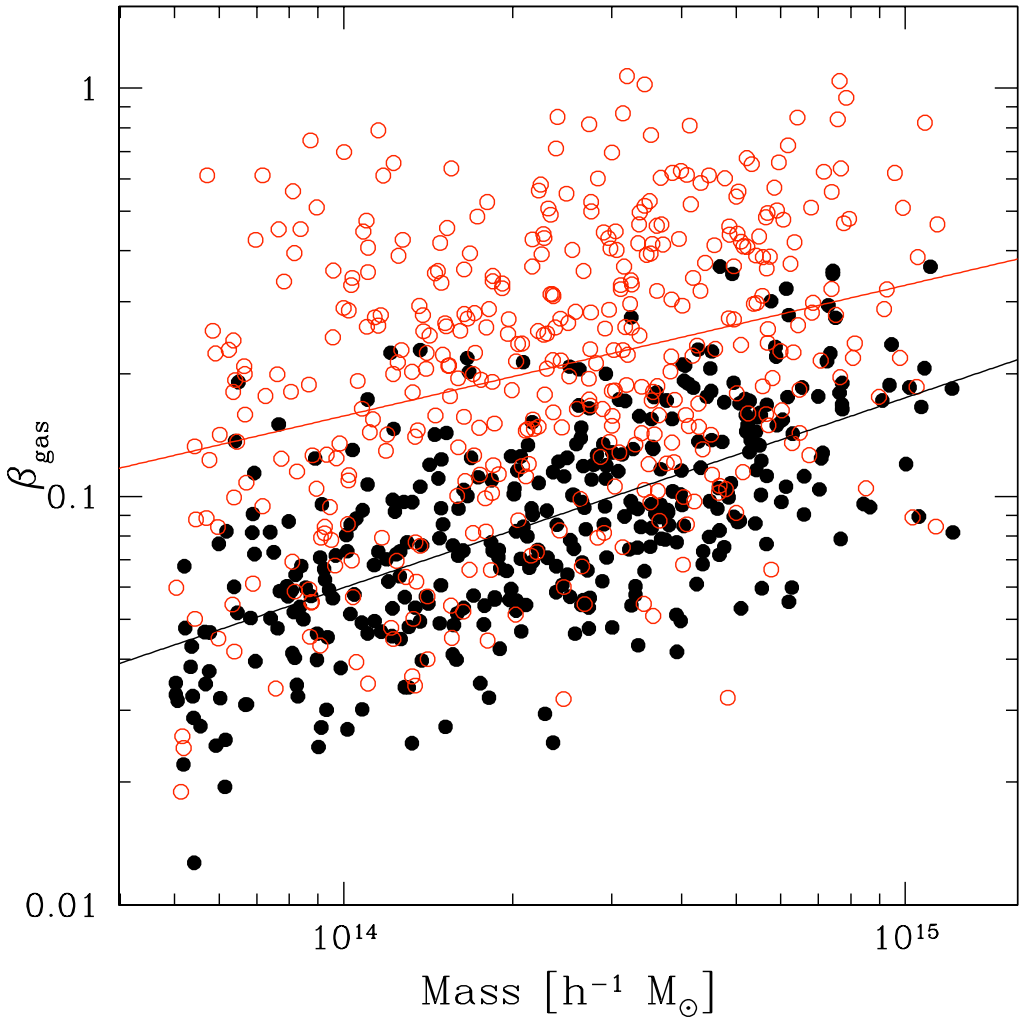

Figure 4.3. $\beta_{\rm gas}$ as a function of mass for the PH simulation (filled, black points) and the GO simulation (open, red points). We have plotted a random subset, weighted to the low-mass end, making up approximately 10% of the sample.

contribute to systematic uncertainties in hydrostatic mass estimates. Unfortunately, $\sigma_{\rm gas}$ is not measureable with the current generation of X-ray telescopes, so we must rely on simulations to provide constraints on the value of $\beta_{\rm gas}$ in clusters.

To measure the evolution of the total energy of the gas, we look at the thermal energy and the and kinetic energy of the gas:

$$E = \frac{kT_m}{\mu m_p} + {\sigma_{\rm gas}}^2. \tag{4.13}$$

Signal	β	Self-Similar Prediction
$\sigma_{\rm DM}$	0.34	1/3
T_m	0.76	2/3
$T_{\rm sl}$	0.73	2/3
$L_{\rm bol}$	1.39	7/6
$f_{\rm ICM}$	-0.44	0
Y	0.33	2/3
$\hat{Q}$	-0.13	N/A
c	-0.68	N/A

Table 4.2. The evolution of the normalization in the PH simulation via the form $S_{14}(a) \propto E(a)^{\beta}$, and the expected self-similar evolution (Kaiser, 1986).

Even if the mass-weighted temperature does not evolve in a self-similar fashion, we expect the total gas energy to evolve self-similarly in an adiabatic simulation. Indeed, we see in Figure 4.4 that the total gas energy in the GO simulation follows the relation $E \sim [ME(z)]^{2/3}$; the contribution by the gas velocity dispersion to the total energy of the gas cannot be ignored.

Baryon fraction. The baryon fraction drastically differs between the PH and GO halos. Although $f_{\rm ICM}$ is difficult to measure observationally, as it requires measuring the cluster mass, the differences in cluster properties in PH and GO are driven by the different states of the ICM. At redshift zero, the distribution of $f_{\rm ICM}$ in the GO simulation is uniform: halos have a baryon fraction of $f_{\rm ICM} = 0.90$ within r_{200}, with a scatter of 3.6%. There is effectively no trend with mass, as the slope is $4.7 \times 10^{-4} \pm 1.9 \times 10^{-2}$. This is consistent with the range of adiabatic SPH simulations done at similar resolution and evaluated at r_{200} by Crain et al. (2007) and Ettori et al. (2006). The adiabatic SPH simulations of the MareNostrum universe Gottlöber & Yepes (2007) are simulated at twice our numerical resolution, and have a baryon fraction at r_{vir} of $f_{\rm ICM} = 0.92$. This small but significant increase is due to the larger radius inside of which $f_{\rm ICM}$ is measured. Our measured value of $f_{\rm ICM}$ is also much lower than the value measured by Kravtsov et al. (2005) at r_{vir} in their adiabatic AMR (Adaptive Mesh Refinement) code. This difference is due to the larger radius at which they measure $f_{\rm ICM}$, and the different algorithm for treatment of the gas physics. For adiabatic simulations, they note a statistically-significant offset in the

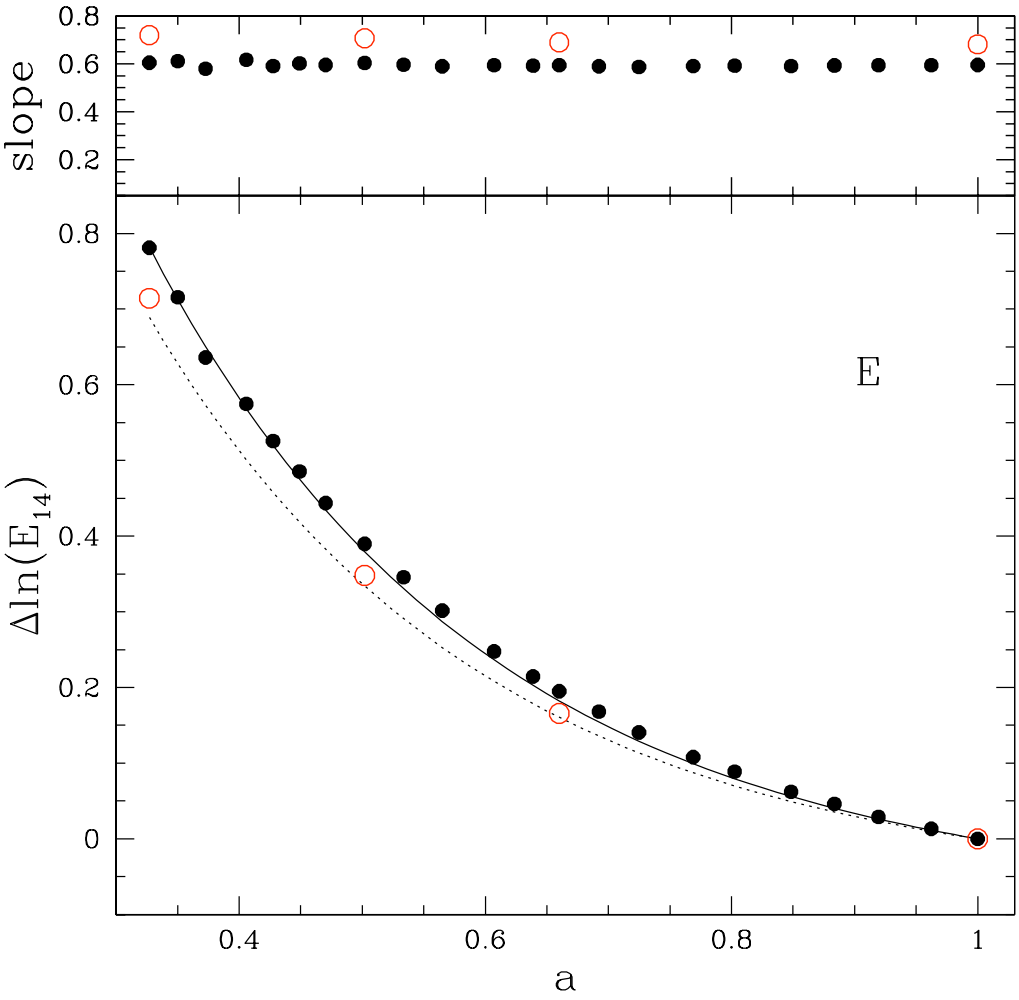

Figure 4.4. Evolution of the normalization of the total energy of the gas for the PH simulation (filled, black points) and the GO simulation (open, red points). The dotted line is the self-similar prediction of $E \sim [ME(z)]^{2/3}$, and the solid line is the measured evolution in the PH simulation. For the evolution of the PH energy, we plot a subset of time outputs evenly spaced in a.

PH Simulation			GO Simulation		
a_0	a_1	a_2	a_0	a_1	a_2
-2.27	0.310	-0.0661	-1.82	5.11×10^{-4}	9.38×10^{-4}

Table 4.3. Fit parameters for the $f_{\rm ICM} - M$ relation at redshift zero, which is fit to the quadratic form $\ln f_{\rm ICM} = a_0 + a_1 \ln M + a_2 (\ln M)^2$, with mass in units of $10^{14}\ h^{-1}\ {\rm M}_\odot$. The scatter is measured in ln space at fixed mass, and the uncertainties are calculated from Monte Carlo sampling with replacement.

baryon fractions of halos in SPH and AMR simulations.

The distribution of $f_{\rm ICM}$ in the PH simulation at redshift zero is more complicated. As the preheating has a greater effect on the low-mass halos, there is a mass dependency in the baryon fraction: lower-mass halos lose a greater fraction of their baryons within r_{200}. The more massive halos are able to hold onto more of their gas, due to the lower fractional increase of entropy they experience, and their deeper potential wells. Due to this complication, we model the baryon fraction at fixed mass with a quadratic in $\ln M$. When presenting the evolution of the slope and normalization of the baryon fraction in Figure 4.2, we use the values at $10^{14}\ h^{-1}\ {\rm M}_\odot$ and at $5 \times 10^{14}\ h^{-1}\ {\rm M}_\odot$ to illlustrate this strong mass dependence.. The high mass clusters have baryon fractions similar to clusters in GO , $f_{\rm ICM} \sim 0.90$.

The evolution of the baryon fraction in the GO simulation is straightforward: the slope and scatter remain the same, while the mean baryon fraction increases slightly as redshift increases. This is consistent with the findings of Gottlöber & Yepes (2007) in the MareNostrum simulation. Due to energy transfer, the dark matter mass of a halo increases faster than the gas mass, during infall events (McCarthy et al., 2007). Hence, over the course of many merger events, the baryon fraction of a halo slightly decreases. Gottlöber & Yepes (2007) measure baryon fraction within r_{vir}, which corresponds to a critical overdensity of $\Delta_c \sim 100$. Within r_{vir}, they see the mean baryon fraction increase from $f_{\rm ICM} = 0.92$ at $z = 0$ to $f_{\rm ICM} = 0.94$ at redshift $z = 1$. Considering that the measured baryon fraction depends on the choice of overdensity, this agrees with our numbers at $\Delta_c = 200$ of $f_{\rm ICM} = 0.90$ at redshift $z = 0$ and $f_{\rm ICM} = 0.93$ at $z = 1$.

The evolution of the baryon fraction in the PH simulation is more complicated.

We see a strong increase in baryon fraction between redshift $z = 1$ and redshift $z = 0$, as gas blown out during the preheating at $z \sim 4$ falls back onto the halos. By redshift $z = 0$, the baryon fraction of the high-mass halos, $M \sim 10^{15}\, h^{-1}\, \mathrm{M}_{\odot}$, is very close to the baryon fraction of the halos in the GO simulation. In practice, this is an upper limit for the baryon fraction of the PH halos, so the slope at $M = 10^{14}\, h^{-1}\, \mathrm{M}_{\odot}$ decreases towards redshift $z = 0$, as the baryon fraction of the lower-mass halos continues to increase. In Figure 4.2 we also present the evolution of the slope and the normalization at $M = 5 \times 10^{14}\, h^{-1}\, \mathrm{M}_{\odot}$ in the PH simulation. At this higher mass scale, the slope is lower and the evolution with redshift is weaker. In fact, there is very little evolution since redshift $z = 1$, at which point the high-mass halos have baryon fractions similar to that of their GO counterparts. The most massive halos are much more stable to the effects of the preheating than the lower-mass halos in the PH simulation.

NFW concentration. We measure the NFW concentration, c from the total mass density profile of each cluster. The mean concentration in the PH simulation at $10^{14}\, h^{-1}\, \mathrm{M}_{\odot}$, $c = 2.62$, is lower than the mean concentration in the GO simulation, $c = 3.26$. As discussed in Stanek et al. (2009), the PH halos have a lower baryon fraction than the GO halos, due to the preheating. This leads to deeper potential wells in the GO simulation at fixed number density, leading to the more concentrated density profiles. The mass dependence of the baryon fraction in the PH simulation likely contributes to the slight mass dependence of c in the PH simulation. The mean concentrations in PH and GO are slightly lower than the mean halo concentrations measured at the high-mass end in the original Millennium Simulation, of $c \sim 3.5$ to 4 (Gao et al., 2008).

4.3.2 X-ray and SZ Signals

The quantities presented in Section 4.3.1 are direct probes of a cluster's dynamical state. However, they are not directly observable, so we must measure the common bulk observed properties Y, T_{sl}, L_{bol}, and the emission measure $\hat{Q}$ in the pair of simulations.

Sunyaev-Zeldovich decrement. We measure Y, an X-ray analogue to the Sunyaev-Zeldovich decrement. Simulations by Kravtsov et al. (2006); Nagai (2006) show that it has low scatter with mass, making it ideal both for cluster detection and mass measurements. As seen in Figure 4.5, despite the differences in the scaling of T_m and $f_{\rm ICM}$ with mass in the two simulations, the $Y - M$ relation is consistent between PH and GO . As Y is a probe of the cluster pressure, a higher T_m will result in a lower $f_{\rm ICM}$, hence the agreement between simulations. Physically, the quantity $-\nabla P/\rho$ should closely trace the halo mass, and we find that the radial profiles at fixed mass match well between the simulations. At high mass, the simulations agree very well. At low mass, the GO SZ-decrement is slightly higher than the PH SZ-decrement, leading to the steeper slope in the PH simulation. This is driven by the lower gas density in the PH simulation. Observationally, at fixed mass PH halos have a higher T_m than the GO halos, while the GO halos have a higher $f_{\rm ICM}$ than the PH halos. At the high mass end, these effects offset each other to create good agreement between the two simulations. At lower masses, the baryon fraction in the PH halos is so low that this agreement disappears, leading to a Y that is $\sim 10\%$ lower in PH than in GO . Whatever the cluster astrophysics, Y may be the best unbiased probe of the thermal state of the ICM, especially above the mass limit of $10^{14}\,h^{-1}\,{\rm M}_\odot$ of future SZ surveys (Kravtsov et al., 2006; Zhang et al., 2008). In Figure 4.5 we compare the evolution of the $Y-M$ relation in the two simulations. Although the two simulations agree at redshift $z = 0$, the evolution differs between the two simulations. Furthermore, driven by $f_{\rm ICM}$, the evolution of the normalization is not a simple power of $E(z)$.

Spectroscopic-like temperature. We also consider the spectroscopic-like temperature, $T_{\rm sl}$, an analytic prescription derived by Mazzotta et al. (2004) to match observed X-ray temperatures. Rasia et. al. (2009, in prep) show that the $T_{\rm sl}$ measured in a simulation agrees well with the X-ray temperature measured in simulated observations of simulated halos. The slopes agree well between the simulations, $\alpha = 0.57$, but at fixed mass the PH halos have a $T_{\rm sl}$ about $\sim 40\%$ higher than the GO halos. The PH simulation has a much more uniform gas distribution than the GO simulation, and the cold, dense clumps in GO pull down the $T_{\rm sl}$ measure.

In the PH simulation, the evolution of the $T_{\rm sl} - M$ relation is steeper than the self-similar prediction of $T_{sl,14}(a) \sim [E(a)]^{2/3}$. Furthermore, as listed in Table 4.2, the evolution of the $T_{\rm sl} - M$ relation in the PH simulation is very close to the evolution of the $T_m - M$ relation. However, the evolution of the $T_{\rm sl} - M$ relation in the GO simulation is much less steep than the evolution in the PH simulation. This is likely due to the effect that the dense gas and substructure have on the $T_{\rm sl}$ measure.

Bolometric luminosity and Emission measure. The difference in baryon fraction and temperature between the simulations drives the rest of the bulk X-ray properties. We measure the cluster bolometric luminosity, $L_{\rm bol}$, and its scaling with mass. In GO , the $L_{\rm bol} - M$ relation is less steep than the self-similar slope of $L \sim M^{4/3}$ (Kaiser, 1986). The normalization of the $L-M$ relation between the two simulations disagrees by nearly an order of magnitude at the low-mass end. At fixed mass, we break down the halo luminosity to its temperature, gas density, and structure components, via $L \propto {f_{\rm ICM}}^2 Q T^{1/2}$ (Arnaud & Evrard, 1999). From this, we can pinpoint which factors contribute to the vast difference between halo luminosity at fixed mass between the two simulations. Although the PH halos have a higher temperature at fixed mass, this affect is dwarfed by the difference in $f_{\rm ICM}$ at fixed mass between the two simulations. The steeper slope in $f_{\rm ICM} - M$ in PH drives the steeper slope in $L_{\rm bol} - M$ in PH . In Section 4.4.1 we consider how the scatter in the $L_{\rm bol} - M$ relation depends on the scatter in $f_{\rm ICM}$, T, and Q at fixed mass.

The evolution of the normalization in PH is not a perfect power of $E(a)$, due to the complicated evolution of $f_{\rm ICM}$ with redshift. We see a best-fit of $L_{14}(a) \sim [E(a)]^{1.39}$ in the PH simulation, which is not as steep as the evolution in the GO simulation. The evolution of the $L - M$ relation in the PH simulation is driven by the evolution of the baryon fraction. For halos with a roughly constant baryon fraction with redshift, if halos are identified by their critical overdensity, higher-redshift halos have a gas density that is higher at a fixed critical overdensity. This higher physical density at higher redshift leads to the higher luminosities at fixed mass. In the PH simulation, however, the higher-redshift halos have a lower baryon fraction than their redshift zero descendents: hence the lower luminosities at high redshift. Identifying how the true

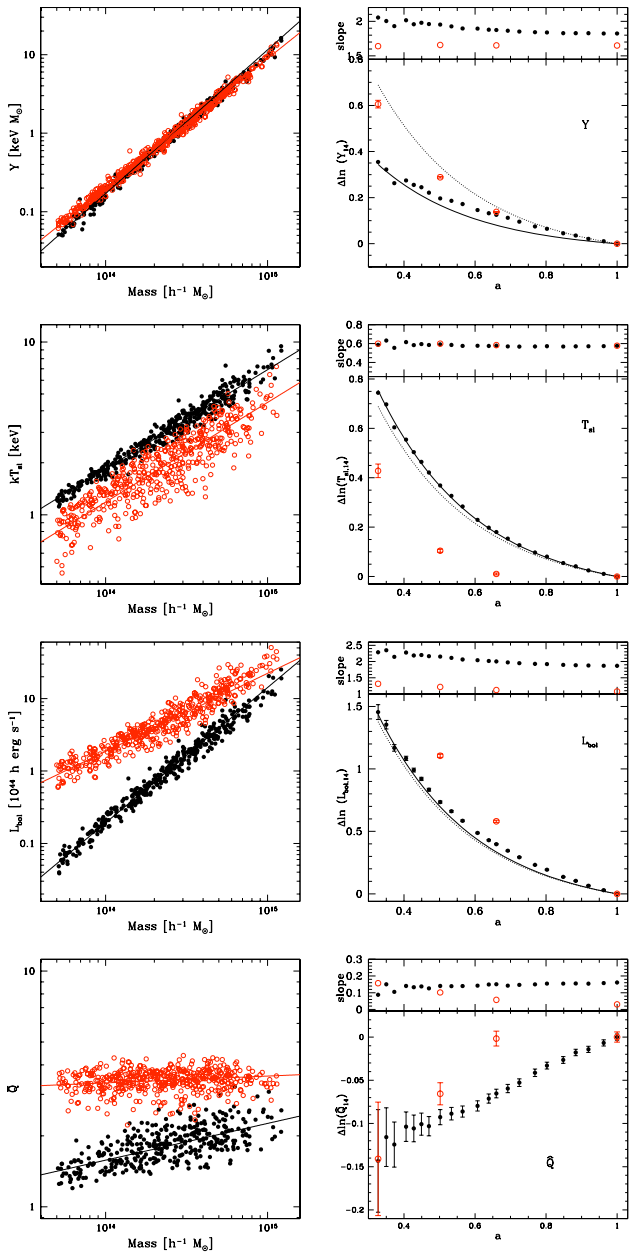

Figure 4.5. Scaling relations at redshift zero and evolution of fit parameters of the X-ray and SZ signals for the PH (black, filled points) and GO (red, open points) simulations, along with the best-fit scaling relation. The left-hand panels present scaling relations of Y, $T_{\rm sl}$, $L_{\rm bol}$, and $\hat{Q}$, and we plot a random sample of about 10% of the halos. The right-hand panels present the evolution of the slope and the differential evolution of the normalization ($\Delta \ln S$). In the right-hand panels, the solid lines denote the real evolution of the normalization, while the dotted line denotes the self-similar prediction, as listed in Table 4.2. For the PH simulation, we present time outputs evenly spaced in a.

$L - M$ relation differs from the self-similar prediction will let us draw observational constraints on evolution of the hot gas component of galaxy clusters.

We look at the mass scaling of the dimensionless emission measure $\hat{Q}$, which is a piece of the bolometric X-ray luminosity, as derived by Arnaud & Evrard (1999). The slopes of the $\hat{Q} - M$ relation are similar between the two simulations, but the normalization is significantly higher in the GO simulation. This higher normalization contributes to the higher normalization of the $L - M$ relation in the GO simulation. A higher normalization of the $\hat{Q} - M$ relation points to a steeper gas density profile. Just as the GO halos had a more concentrated total mass density profile than the PH halos, the GO halos have a steeper gas density function.

Although $\hat{Q}$ differs at redshift $z = 0$ at fixed mass between the two simulations, the evolution of the normalization is similar in the two simulations, as seen in Figure 4.5. As $\hat{Q}$ is one of the luminosity components, we see that the evolution of the $L-M$ relation is driven by the baryon fraction, not the structure function.

4.3.3 Connection with Observations

As shown by Hartley et al. (2008), the PH simulation matches the normalization of the observed local $L-T$ relation quite well. We continue by comparing the PH $L-T_{\rm sl}$ relation to the REXCESS survey (Pratt et al., 2008), the most recent large-scale local X-ray survey. In Figure 4.6, we plot the GO and PH $L_{\rm bol}-T_{\rm sl}$ relations, measured within $\Delta_c = 500$, and the core-excised $L_{\rm bol} - T$ data presented in Pratt et al. (2008). Much of the large scatter in the observed $L_{\rm bol} - T$ relation is due to variation in the core emission. The similarly low scatters in the core-excised REXCESS $L_{\rm bol} - T$ and the PH $L_{\rm bol} - T_{\rm sl}$ indicate that most galaxy clusters are smooth and well-behaved outside of the core. This agrees with simulations by [CITE DOLAG?] which show that the outer regions of clusters are dominated by gravity.

For higher redshift, we consider the CCCP clusters, a subset of the 400 square degree survey which has been followed-up with Chandra (Vikhlinin et al., 2008). These clusters range from approximately $0.3 < z < 0.8$, so we scale all luminosities to redshift $z = 0.5$ for comparison to our $L_{\rm bol} - T_{\rm sl}$ relation. In Figure 4.7, we plot

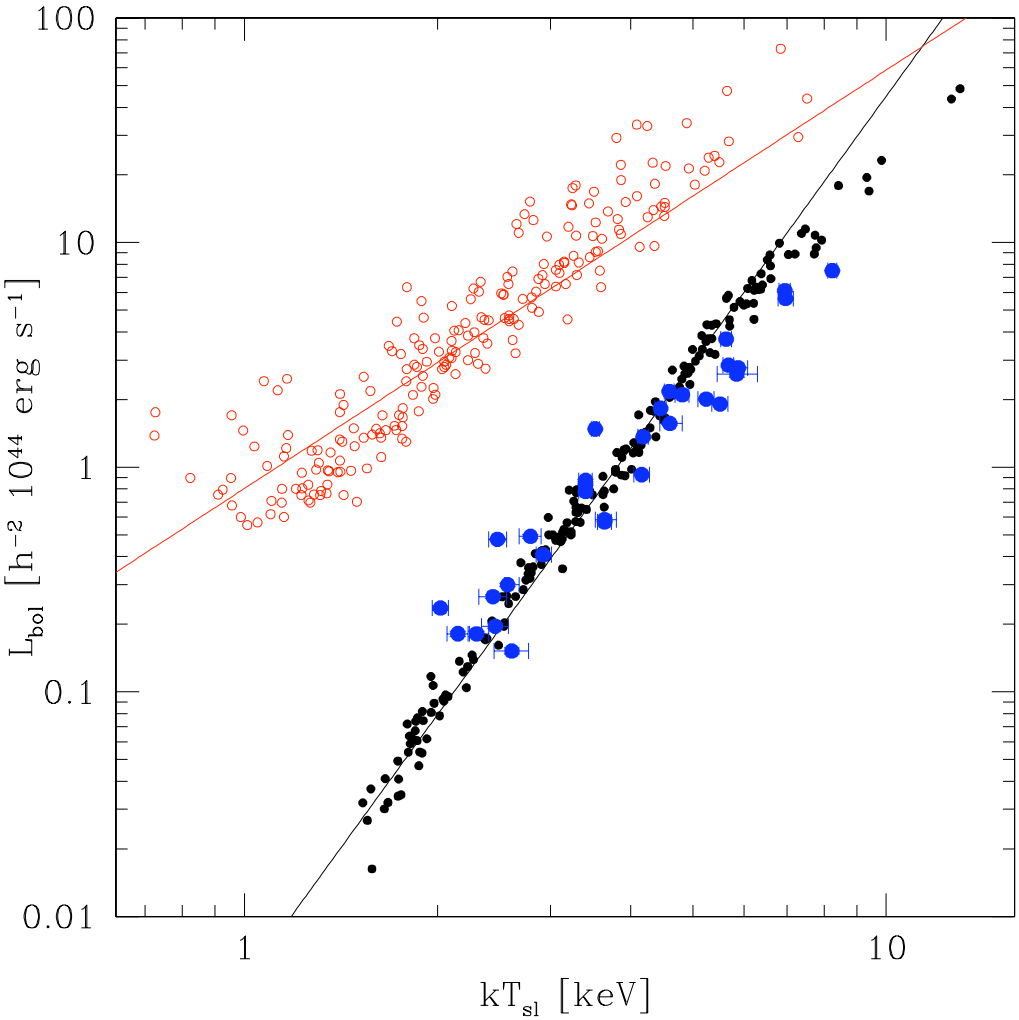

Figure 4.6. The redshift zero $L_{\rm bol} - T_{\rm sl}$ relation for `GO` (open, red points), `PH` (filled, black points), measured within $\Delta_c = 500$, and the core-excised $L_{\rm bol} - T$ relation from the REXCESS survey (large, blue points) (Pratt et al., 2008).

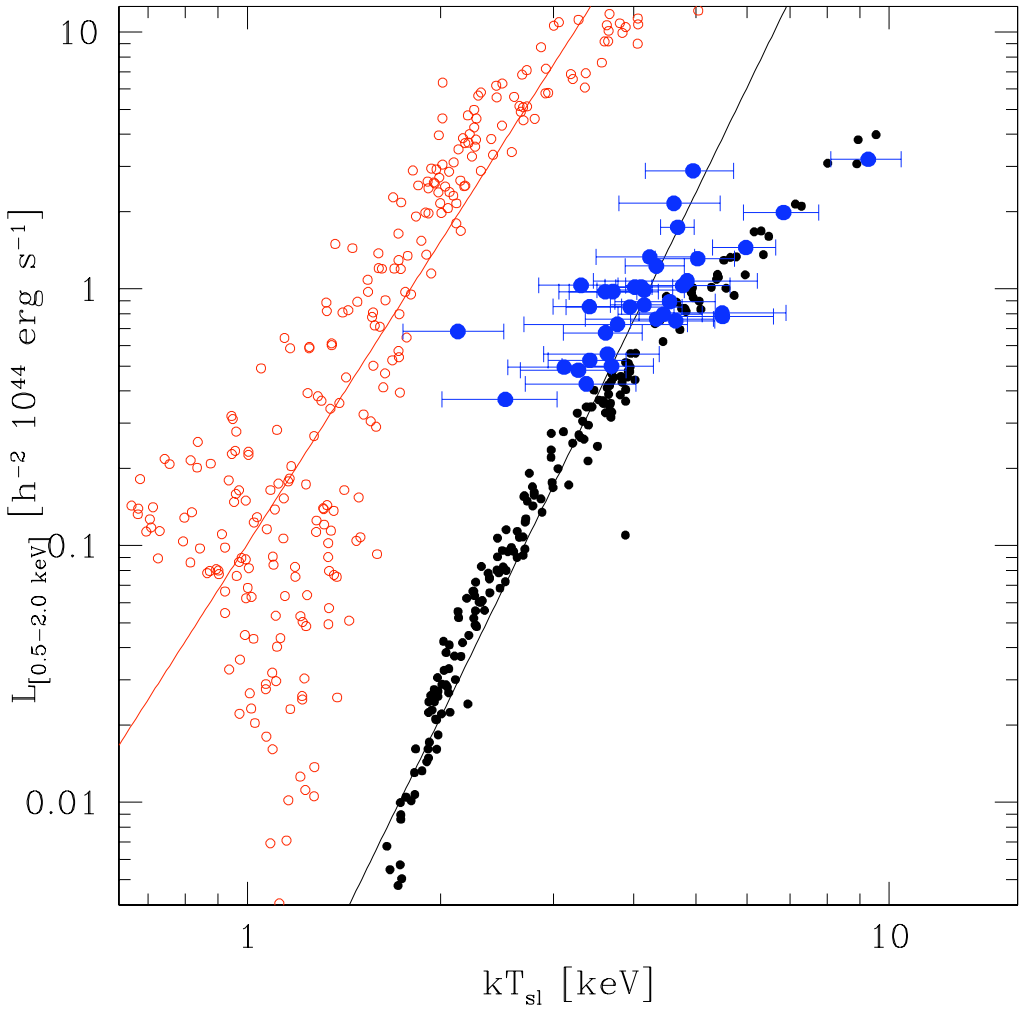

Figure 4.7. The redshift $z = 0.5$ $L_{[0.5-2.0]} - T_{\rm sl}$ relation for GO (open, red points), PH (filled, black points), measured within $\Delta_c = 500$, and the CCCP $L_{[0.2-2.0]} - T$ relation from Vikhlinin et al. (2008) (large, blue points), scaled to redshift $z = 0.5$.

the redshift $z = 0.5$ GO and PH $L - T_{\rm sl}$ relations, measured within $\Delta_c = 500$, and the $L_{\rm bol} - T$ data presented in Vikhlinin et al. (2008). The cores of the CCCP clusters have not been excised in the luminosity calculation, which likely accounts for the higher observed scatter than that of the REXCESS $L_{\rm bol} - T$ relation.

We see agreement to redshift $z = 0.5$ in the PH $L_{[0.5-2.0]} - T_{\rm sl}$ relation and the observed data, particularly if the observations have been core-excised. Now we consider some components of the $L - T$ relation, particularly the observed $T - M$ and $f_{\rm ICM} - M$ relations. For these comparisons, we use the local set of clusters from

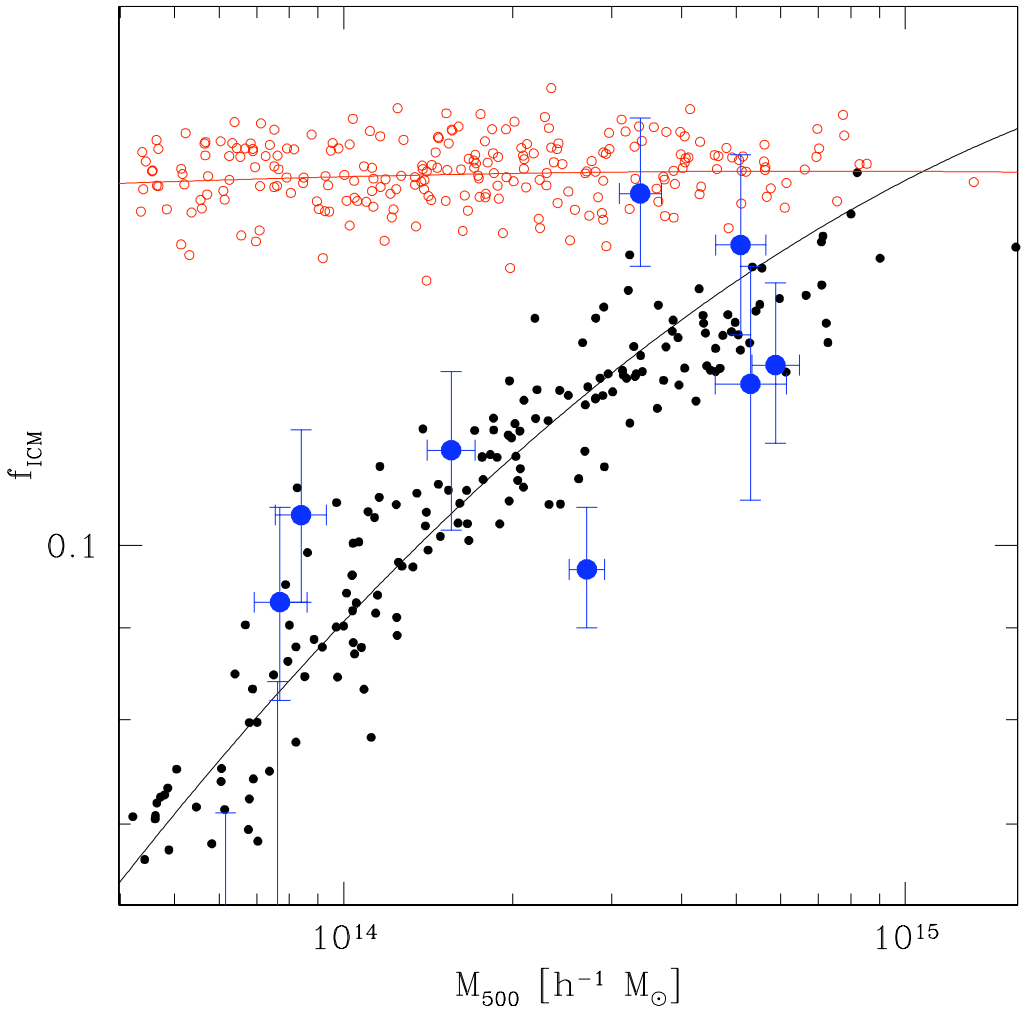

Figure 4.8. The redshift zero $f_{\rm ICM} - M$ relation for `GO` (open, red points), `PH` (filled, black points), measured within $\Delta_c = 500$, and the data from Arnaud et al. (2007) (large, blue points).

Arnaud et al. (2007). Again measuring within $\Delta_c = 500$, at redshift zero the `PH` data agrees well with the observed $f_{\rm ICM} - M$ relation (Figure 4.8). Not only do the two populations have a similar mean $f_{\rm ICM}$ value, but both show a trend with mass. This agrees with previous observations by Vikhlinin (2006). Recalling that $f_{\rm ICM}$ is only a measure of the hot gas content of a cluster, and not the total baryon content, these hot gas fractions are much lower than $\Omega_b/Omega_m$.

When comparing the `PH` $M - T_{\rm sl}$ relation to the $M - T$ from Arnaud et al. (2007), we see that the two relations have very similar slope and scatter, but a consistent offset in mass, as seen in Figure 4.9. Arnaud et al. (2007) calculated the masses using

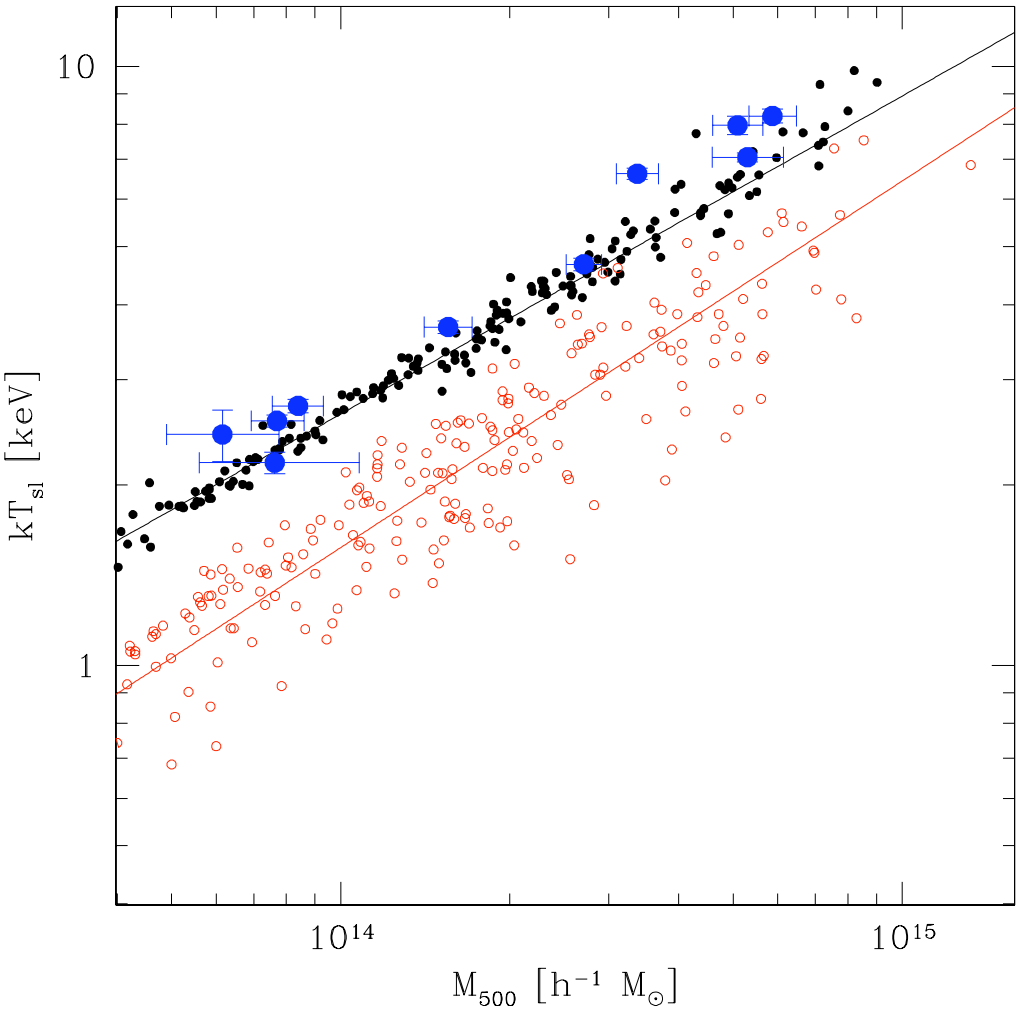

Figure 4.9. The redshift zero $T_{\rm sl} - M$ relation for `GO` (open, red points), `PH` (filled, black points), measured within $\Delta_c = 500$, and the data from Arnaud et al. (2007) (large, blue points).

hydrostatic mass estimates, which simulations show underestimate the true mass by approximately 20% (Rasia et al., 2006). Assuming that the `PH` model is a realistic model of galaxy clusters, we investigate the degree of this shift by creating realizations of the `PH` data with many values of the mean mass bias and the scatter in the mean mass bias. Although the the shift was not particularly sensitive to the scatter, our best fit finds that hydrostatic mass estimates underestimate the true mass by $\sim 16\%$. This is in good agreement with the simulations by Rasia et al. (2006). In Figure 4.10, we plot the significance contours from the χ^2 test for the mean mass bias and the scatter in the mean mass bias.

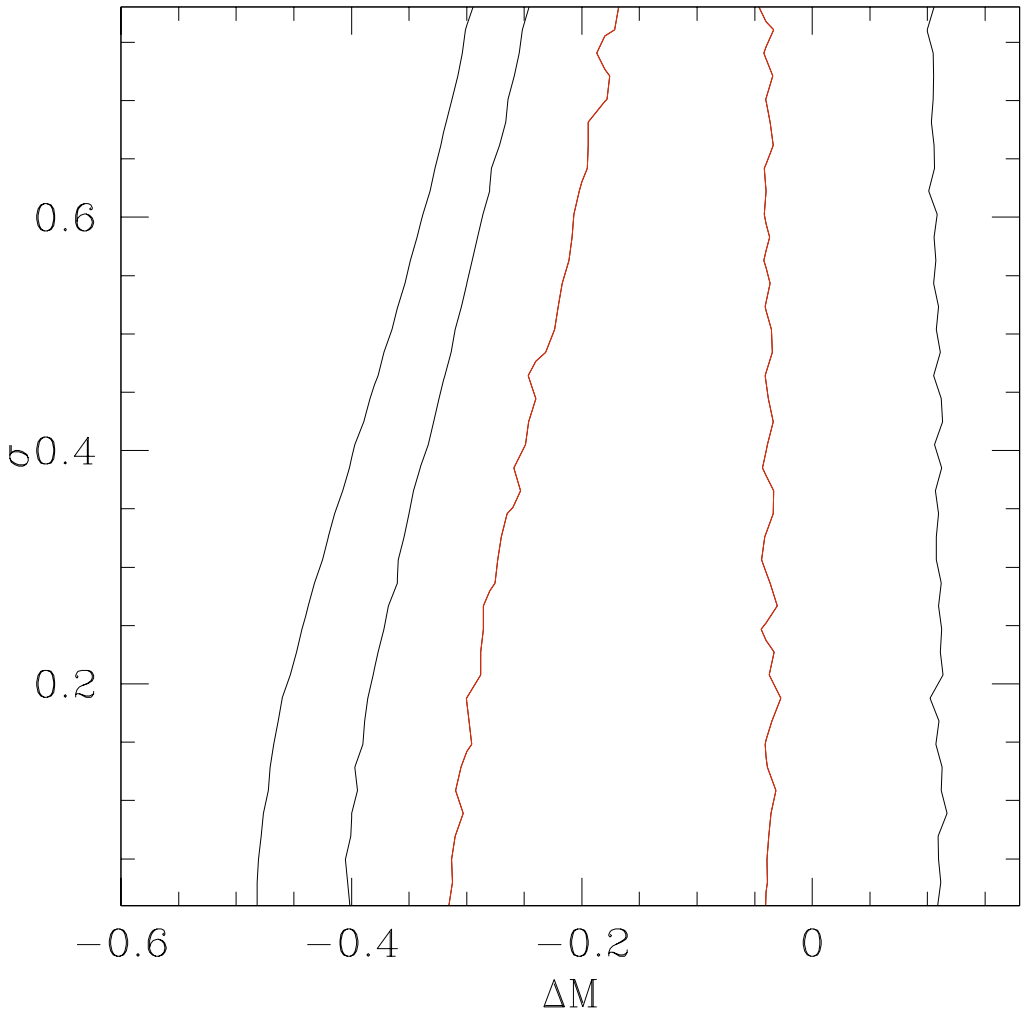

Figure 4.10. Contours marking the 99%, 98%, and 95% significance levels for the mean and scatter of the mass shift needed to match the `PH` simulation masses to the observed masses from Arnaud et al. (2007) at fixed temperature. Although these results are not particularly sensitive to the degree of uncertainty in the mass shift, the mean mass shift, $\Delta M \sim 16\%$, is in agreement with results from Rasia et al. (2006).

Overall, the bulk X-ray properties of the PH simulation match the local scaling relations quite well. This is particularly true after excising the core from the observations, and after considering the mass bias introduced by hydrostatic mass estimates. Although the physics of the PH model are simple, it is useful for providing statistically- significant constraints on observations. In the next section, we discuss the second moment of the scaling relations in the simulations.

4.4 Covariance of Bulk Properties

We move on to the second moment of the cluster scaling relations. We describe it as a covariance matrix, where each element can be described by

$$\Psi_{xy} = \frac{1}{N}\sum_{i}^{N}(x_i - \bar{x}(\mu, a))(y_i - \bar{y}(\mu, a)), \tag{4.14}$$

also denoted as $< \delta_x \delta_y >$, and the correlation matrix $C_{xy} = \frac{\Psi_{xy}}{\sigma_x \sigma_y}$. We measure and plot the normalized deviations, $\delta_{x,i} = (x_i - \bar{x})/\sigma_x$ The diagonal elements of the covariance matrix is simply the variance in the j^{th} element of the covariance matrix at fixed mass: $\sigma_j^2 = \Psi_{jj}$ We show a graphic representation of the covariance matrix in Figure 4.11, at redshift zero for both PH and GO . Along the diagonal, we plot the distribution of the deviation of each cluster property from the mean power-law relation at fixed mass. Off the diagonal, we plot the normalized deviation (δ_y/σ_yvs.δ_x/σ_x) for each pair of cluster observables in our array of observables. The panels below and to the left of the diagonal plot PH halos, and the panels above and to the right of the diagonal plot GO halos. The eccentricity of the spray of clusters in each panel scales with the correlation coefficient: for instance, the correlation coefficient between $f_{\rm ICM}$ and Y in the PH simulation is very high, $r = 0.9$, and this is clearly illustrated by the panel plotting $\delta_Y$vs.δ_{fICM}. The redshift-zero values of the correlation coefficients, along with uncertainties from Monte Carlo sampling, are presented in Table 4.5. At redshift zero, as in the best-fit parameters to the power laws, the uncertainties in the correlation coefficients are on the order of $\sim 0.1\%$.

Understanding the variance at fixed mass is necessary for calculating the window

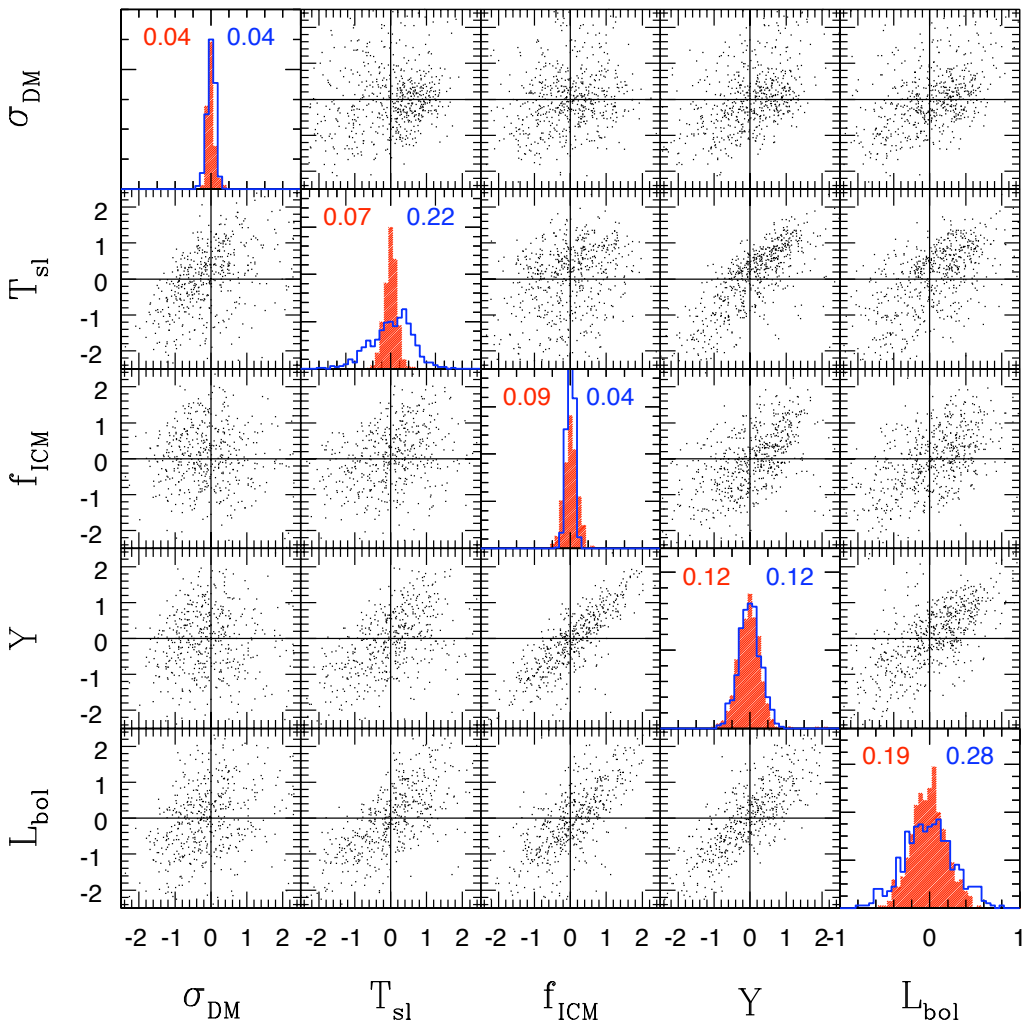

Figure 4.11. A graphical representation of the covariance matrix for the two simulations at $z = 0$. The lower-left panels are for the PH simulation, and the upper-right plot the GO simulation. Each off-diagonal panel plots the normalized deviation of each cluster, $\delta_{xy}/(\sigma_x\sigma_y)$, from the mean relation with mass for a pair of bulk properties. From top to bottom and left to right, the bulk properties considered are dark matter velocity dispersion $\sigma_{\rm DM}$, mass-weighted temperature $T_{\rm sl}$, baryon fraction $f_{\rm ICM}$, Sunyaev-Zeldovich decrement Y, and luminosity L. The panels along the diagonal plot the distribution of the deviations from the mean relation for each bulk property, with shading for the PH simulation and a thick solid line for the GO simulation.

function of flux-limited observations (Stanek et al., 2006). In addition to the variance, multi-waveband surveys also require measuring the covariance between the selected properties at fixed mass. As shown in Nord et al. (2008), the covariance between observables is an important part of a joint probability distribution, and is necessary for calculating the selection function of flux-limited surveys. In section 4.4.4, we will discuss the implications of our covariance measures for the results from cluster surveys.

4.4.1 Signal Variance at Fixed Mass

Measuring the scatter in mass-observable relations is essential for calculating the selection function of cluster surveys (Stanek et al., 2006). Before we calculate the covariance between cluster properties at fixed mass, we present and discuss the scatter in some of the bulk halo properties. We also consider the Gaussianity of the distribution of the deviations at fixed mass, presenting the distribution of the normalized deviates in Table 4.4. In Table 4.4, we chose percentages corresponding to ± 1 and 2σ for a perfect Gaussian, so that the deviations from Gaussianity are obvious at a glance. For example, a perfect Gaussian should have a deviate of $\delta/\sigma = 0$ at the 50% rank. A number significantly different than zero indicates that the distribution is skewed in one direction. As in Section 4.3, we begin with structural properties and move on to the X-ray and SZ observables.

The scatter in the dark matter velocity dispersion, $\sigma_{\rm DM}$, is very low in both simulations, $\sigma \sim 0.04$. This is in agreement with the low degree of scatter discussed in Evrard et al. (2008). Not only is this scatter very small, but both distributions are narrower than a Gaussian distribution, as shown in Table 4.4. Both simulations also have a slight tail towards high velocity dispersion. Looking merger histories for the `PH` halos, we find that nearly all halos with a deviation of $\delta > 3\sigma$ have undergone a merger since redshift $z = 0.2$. This enhancement due to a merger is quite small, however, and it is reassuring to note that the dark matter velocity dispersion closely tracks the mass, no matter the state of the baryons.

The scatter in the mass-weighted temperature, T_m, is significantly lower in the

PH simulation than in the GO simulation. If gas physics are dominated by only gravitational effects, then in a virialized cluster, ${\sigma_{\rm DM}}^2 \sim T_m$, and $2\sigma\sigma_{\rm DM} \simeq \sigma_{T_m}$. The values of the scatter in the GO simulation is very close to this, with $\sigma_{T_m} \sim 2.5\sigma_{\sigma_{\rm DM}}$. However, the scatter in T_m is much lower in the PH simulation. This lower scatter is due to the domination of the preheating in the temperature measure.

The scatter in $f_{\rm ICM}$ at fixed mass in the GO simulation is very small, $\sim 3.6\%$. This is in the range of other gravity-only SPH simulations: Crain et al. (2007) see a scatter of $\sim 6\%$ about the mean baryon fraction, while Ettori et al. (2006) see a scatter of $\sim 2\%$. In the absence of other astrophysical properties, the gas distribution traces the dark matter distribution very well. In the PH simulation, however, the scatter in $f_{\rm ICM}$ at fixed mass is significantly higher, $\sim 9\%$. Furthermore, the scatter is highly mass-dependent: if we split the sample at $3\times10^{14}h^{-1}{\rm M}_\odot$, the scatter on the low-mass end is $\sim 13\%$, while only $\sim 7\%$ on the high-mass end. However, in both simulations, the distribution of the deviates in $f_{\rm ICM}$ is very close to a Gaussian distribution.

Not only does the mean $Y-M$ relation agree well between the two simulations, but both simulations have a similarly low scatter, $\sim 13\%$. This low degree of scatter point to the Sunyaev-Zeldovich effect being an excellent mass proxy in cluster surveys. Furthermore, as seen in Table 4.4, the distribution of deviations in Y at fixed mass are very close to a Gaussian distribution. In Section 4.4.2 we discuss the contribution of σ_{T_m} and $\sigma_{f_{\rm ICM}}$ in each simulation to the scatter in Y.

In both simulations, the scatter in $T_{\rm sl}$ at fixed mass is higher than the scatter in T_m at fixed mass. The difference is slight in PH , but over a factor of two in GO . The substructure in the gas in GO contributes to the scatter in fixed mass in the $T_{\rm sl}$ measure. As $T_{\rm sl}$ is extremely sensitive to the gas physics in the halos, caution is necessary when calibrating the scatter from simulations. Furthermore, while the scatter in T_m has a significant tail towards $\delta_T > 0$, the scatter in $T_{\rm sl}$ in GO has a significant tail towards $\delta_T < 0$. This tail is dominated by halos with many clumps of cold, dense gas. As seen in Section 4.3.3, the scatter in $T_{\rm sl}$ at fixed mass is comparable to the observed scatter in temperature at fixed mass.

The luminosity has the highest scatter at fixed mass in both the PH and GO sim-

Signal	Scatter	2.275%	15.865%	50%	84.135%	97.725%
Gaussian	-	-2.0	-1.0	0.0	1.0	2.0
$\sigma_{\rm DM}$	0.0420 ± 0.0008	-1.66	-0.90	-0.11	0.85	2.43
$f_{\rm ICM}$	0.0859 ± 0.0011	-2.14	-0.93	0.03	0.93	1.93
T_m	0.0581 ± 0.0016	-1.90	-0.84	-0.04	0.75	2.11
$T_{\rm sl}$	0.0690 ± 0.0012	-2.17	-0.93	0.04	0.90	1.88
Y	0.125 ± 0.002	-2.04	-0.97	0.04	0.90	1.95
$L_{\rm bol}$	0.193 ± 0.002	-1.98	-0.98	0.004	1.00	1.94
$\hat{Q}$	0.116 ± 0.001	-1.89	-0.99	-0.04	0.97	2.19
c	0.300 ± 0.008	-1.27	0.43	0.13	0.89	0.31
$\sigma_{\rm DM}$	0.0424 ± 0.0010	-1.65	-0.88	-0.12	0.77	2.54
$f_{\rm ICM}$	0.0361 ± 0.0005	-2.12	-0.98	0.03	0.99	1.90
T_m	0.102 ± 0.001	-2.23	-1.00	0.12	0.93	1.69
$T_{\rm sl}$	0.219 ± 0.002	-2.32	-1.06	0.19	0.96	1.49
Y	0.123 ± 0.001	-2.17	-1.00	0.10	0.95	1.75
$L_{\rm bol}$	0.282 ± 0.003	-2.19	-1.03	0.10	0.97	1.70
$\hat{Q}$	0.109 ± 0.001	-2.59	-0.91	0.19	0.85	1.55
c	0.280 ± 0.008	-2.42	-0.97	0.13	0.86	1.28

Table 4.4. The scatter and the distribution of the deviates using percentages for the normalized deviates (δ/σ) for each signal. The top eight rows are for the PH simulation, and the bottom rows for the GO simulation. The error bars on the scatter come from Monte Carlo sampling with replacement of the data. The numbers for a perfectly Gaussian distribution are listed in the first row.

ulations. In the PH simulation, $\sigma_L = 0.19$, and $\sigma_L = 0.28$ in the GO simulation. In Section 4.4.2 we discuss how the scatter in T_m, $f_{\rm ICM}$, and $\hat{Q}$ affect the scatter in the luminosity. The scatter in $\hat{Q}$, the emission measure, is quite low in both simulations: $\sim 12\%$ in PH and $\sim 11\%$ in GO . In the GO simulation, there is a large tail towards negative deviations. Like the $T_{\rm sl}$ deviates in the GO simulation, this tail is dominated by halos with clumps of cold, dense gas. As seen in Section 4.3.3, the scatter in luminosity in both simulations is lower than that of the observed population. However, the luminosities in the PH model are a good description of a core-excised population, so we consider the full covariance matrix to be a good predictor of the core-excised observed population.

4.4.2 Off-Diagonal Elements of the Covariance Matrix

A drastic difference in C_{ij} between the two simulations points to a physical property that is strongly affected by the preheating. It is very useful to identify pairs of cluster

Signal	$\sigma_{\rm DM}$	T_m	$T_{\rm sl}$	$f_{\rm ICM}$	Y	$L_{\rm bol}$	$\hat{Q}$	c
$\sigma_{\rm DM}$	–	0.55	0.81	0.28	0.54	0.51	0.17	0.19
T_m	0.35	–	0.85	0.48	0.97	0.67	0.38	0.49
$T_{\rm sl}$	0.86	0.5	–	0.42	0.83	0.67	0.47	0.64
$f_{\rm ICM}$	-0.10	0.42	0.37	–	0.69	0.60	0.32	0.37
Y	0.079	0.74	0.62	0.88	–	0.73	0.40	0.51
$L_{\rm bol}$	0.26	0.50	0.73	0.76	0.78	–	0.65	0.70
$\hat{Q}$	0.32	0.029	0.56	0.15	0.12	0.59	–	0.71
c	0.15	0.053	0.39	0.29	0.26	0.51	0.64	–

Table 4.5. The redshift zero correlation coefficients, with the results from the PH simulation in the lower, left-hand half, and the results from the GO simulation in the upper, right-hand half, as in Figure 4.11. At redshift zero, we calculated the uncertainties in these measures with Monte Carlo bootstrapping with replacement; the uncertainties are on the order of 0.01

properties whose correlation coefficient is stable to different models of the underlying physics. There are some strong differences in the bulk cluster properties between the two simulations: most notably, the halos in GO have steeper gas density profiles, which the halos in PH are hotter. Stable values of C_{ij} between the two simulations tell us which properties coevolve in similar ways during a merger event over a wide range of cluster types. High values of the correlation coefficient may point to pairs of halo properties that evolve on similar time scales during merger events. In a future paper, we will examine this relationship more closely.

Overall, the correlation terms between pairs of observables are higher in GO than in PH , even though the scatter at fixed mass is higher in GO than in PH for most cluster properties. The correlation matrix illustrates that despite the high scatter in many signals at fixed mass in the GO simulation, the gravitational potential of the halo dominates the gas physics, such that the X-ray observables end up highly correlated to each other.

We begin by discussing the contribution of covariance terms in the scatter of Y and L at fixed mass. From there, we move on to discussing the covariance between pairs of structural properties, and between pairs of observed signals.

As $Y \propto f_{\rm ICM} T_m$, we expect that we can describe the scatter in Y at fixed mass as

$$\sigma_Y^2 = \sigma_T^2 + \sigma_f^2 + 2\Psi_{Tf} \tag{4.15}$$

Thus, the large scatter in T_m and low scatter in $f_{\rm ICM}$ in GO is countered by low scatter in T_m and high scatter in $f_{\rm ICM}$ in the PH simulation. Our measured scatter is still higher than the scatter observed in the simulations of Kravtsov et al. (2006). The low degree of scatter in Kravtsov et al. (2006) is due to an anti-correlation in the deviations of gas mass and temperature at fixed mass. We do not see a negative correlation between $f_{\rm ICM}$ and T_M: $C = 0.42$ in PH and $C = 0.48$ in GO , but these correlations do not contribute much to the scatter in Y at fixed mass.

Since $L \propto {f_{\rm ICM}}^2 \hat{Q} T^{1/2}$, we expect the scatter in luminosity at fixed mass to be described by:

$$\sigma_L^2 = 4\sigma_f^2 + \sigma_Q + \frac{1}{4}\sigma_T^2 + 4\Psi_{fQ} + 2\Psi_{fT} + \Psi_{QT} \tag{4.16}$$

. We see that the scatter in baryon fraction at fixed mass and the scatter in $\hat{Q}$ at fixed mass are the two main contributors to the scatter in luminosity at fixed mass. However, in equation 4.16 we are only considering the second moment of the mean relation. In the GO simulation, the distribution of the deviates in both T_m and $\hat{Q}$ are significantly non-Gaussian, as shown in Table 4.4. As a result, we cannot describe the scatter in L at fixed mass in the GO simulation with Equation 4.16, especially as the distribution of the deviates in L are also significantly non-Gaussian.

Now we consider the covariance of the X-ray and SZ signals with the dark matter velocity dispersion $\sigma_{\rm DM}$. The dark matter velocity dispersion has the lowest scatter at fixed mass in both simulations. The degree of covariance at fixed mass with $\sigma_{\rm DM}$ is a measure of how the X-ray property correlates with the dynamical state of the halo. In general, the covariance between $\sigma_{\rm DM}$ and the various X-ray properties is higher in GO than in PH .

Looking at the covariance between $\sigma_{\rm DM}$ and T_m at fixed mass is a measure of whether the halos are virialized. Since $T_m \propto \sigma_{DM}^2$, independently of mass, a high covariance between $\sigma_{\rm DM}$ and T_m indicates that most of the halos are virialized. We see that the at redshift zero this correlation is much higher, $C = 0.56$ in GO than in PH , where $C = 0.35$. The halos in the GO simulation are governed by gravitational affects only, so T_m and $\sigma_{\rm DM}$ track each other very closely. In PH , however, the preheating

affects the temperature structure of the halos, such that T_m does not only depend on mass, and thus have a high correlation with $\sigma_{\rm DM}$.

In the PH simulation, the baryon fraction of halos is still increasing at redshift zero, especially at low mass. In the GO simulation, however, there is no trend with mass in $f_{\rm ICM}$, and only the slightest evolution since $z = 1$. These very different trends in evolution strongly affect the covariance between $\sigma_{\rm DM}$ and $f_{\rm ICM}$ at fixed mass. In the PH simulation, the two properties are anti-correlated, $r = -0.10$ at redshift zero. In general, halos with recent merger or infall activity will have a higher $\sigma_{\rm DM}$ at fixed mass than the mean relation. During these infall and merger events, the collisionless dark matter accretes faster than the baryons: hence the lower baryon fraction at fixed mass for these halos. Meanwhile, the correlation between $\sigma_{\rm DM}$ and $f_{\rm ICM}$ is positive in GO : $C = 0.28$ at redshift zero.

At fixed mass, the correlation of the other signals with $\sigma_{\rm DM}$ is driven by that with T_m and $f_{\rm ICM}$. Both Y and $L_{\rm bol}$ have a higher correlation with $\sigma_{\rm DM}$ at fixed mass in GO than in PH . The only two signals with lower correlations with $\sigma_{\rm DM}$ in GO than in PH are are $T_{\rm sl}$ and $\hat{Q}$. As $\hat{Q}$ is a measure of the "clumpiness" of the gas, and $T_{\rm sl}$ is very sensitive to small regions of cold, dense gas, their common status is not surprising. In general, there is more substructure in the gas in the GO simulation than in the PH , as seen by the higher values of $\hat{Q}$ in GO , and the higher degree of scatter in $T_{\rm sl}$ in GO . However, $\sigma_{\rm DM}$ is insensitive to the clumpiness of the gas, so these values of the correlation coefficient are lower than in PH .

It is worth noting the interesting case of $C = 0.08$ between Y and $\sigma_{\rm DM}$ in the PH simulation. Algebraically, this is unsurprising due to the positive correlation between $\sigma_{\rm DM}$ and T_m and the negative correlation between $\sigma_{\rm DM}$ and $f_{\rm ICM}$. This lack of correlation suggests that SZ surveys should produce cluster samples that are not biased towards clusters in a particular dynamical state. Furthermore, the low correlation between Y and $\hat{Q}$, $C = 0.12$, shows that SZ surveys should not be biased towards clusters based on the clumpiness of the gas.

We continue to the pairs in the correlation matrix which are similar between the two simulations. In both simulations, the correlation between T_m and $T_{\rm sl}$ at fixed

mass is very high. Although a given halo will not have the same T_m and $T_{\rm sl}$, the high correlation coefficients indicate that the two temperature measures similarly trace the thermal state of a halo. The correlation is higher in the PH simulation than in the GO , due to the effects of cold gas in GO on the $T_{\rm sl}$ measure. Not surprisingly, in both simulations the correlation between $T_{\rm sl}$ and $\hat{Q}$ is higher than the correlation between T_m and $\hat{Q}$. The cold, dense gas which affects the $T_{\rm sl}$ measurement also affects the $\hat{Q}$ emission measure.

Likewise, the correlations between $f_{\rm ICM}$ and the temperature measures agree between the two simulations. As the temperature increases, the gas expands to stay in equilibrium, so the baryon fraction within our chosen radius slightly decreases. Even though the baryon fractions and temperatures differ greatly between the two simulations, the correlation between $f_{\rm ICM}$ and T_m is very close: $C = 0.42$ in PH and $C = 0.48$ in GO .

In the GO simulation, the covariance betweeen T_m and Y is strongest, with $r = 0.97$, while in the PH simulation, the covariance between $f_{\rm ICM}$ and Y is strongest, at $r = 0.90$. Since $Y \propto f_{\rm ICM} T_m$, we generally expect high covariances between Y and T_m or $f_{\rm ICM}$. However, the covariances differ between simulations, and we explain this based on the scatters in the two simulations. In the GO simulation, the scatter in T_m at fixed mass is much higher than the scatter in $f_{\rm ICM}$, so the deviations in T_m drive the deviations in Y. The situation is the opposite in the PH simulation: the higher scatter in $f_{\rm ICM}$ at fixed mass drives the deviations in Y at fixed mass. Despite these differences with Y and $f_{\rm ICM}$ between the two simulations, the correlation coefficient between Y and L agrees between the two simulations: $C = 0.81$. This consistency between simulations is promising for calibrating future surveys that combine X-ray data with SZ measurements, and we discuss this result further in Section 4.4.4.

4.4.3 Evolution of the Covariance Matrix

We first consider the evolution of the scatter with redshift, which we plot in Figure 4.12. The error bars come from Monte Carlo bootstrapping with replacement of the sample. Going back to $z = 2$, few halo properties show any evolution with redshift.

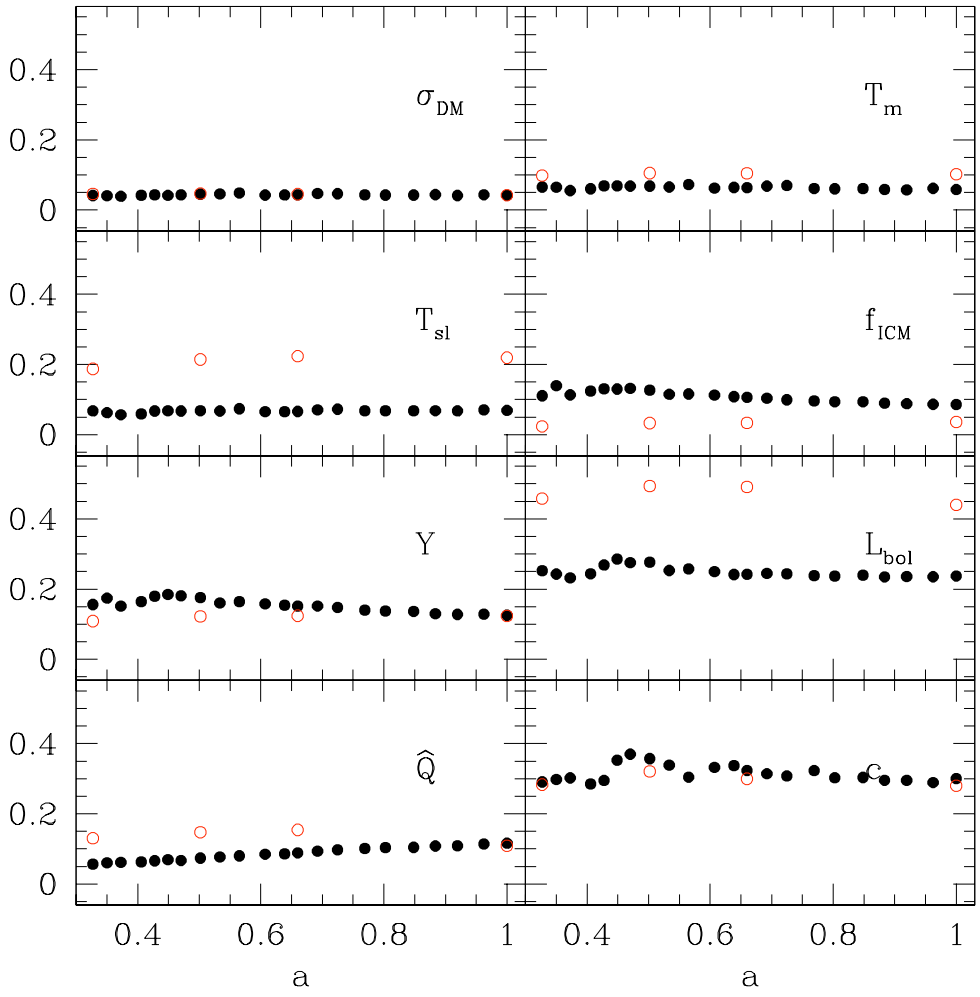

Figure 4.12. Evolution of the scatter in eight bulk cluster properties.

Near redshift $z = 2$ the scatter in baryon fraction slightly increases, which causes an increase in the scatter of Y and L. This increase in scatter is due to the nature of the small, mass-limited sample: at redshift $z = 2$ there are only 62 halos in the PH simulation above our mass cut of $5 \times 10^{13}\ h^{-1}\ \mathrm{M}_{\odot}$. Furthermore, there is a slight mass dependence to the scatter in baryon fraction: at redshift zero, there is a higher scatter at the low-mass end of our mass range, as seen in Figure 4.2. Since the halos at redshift $z = 2$ are only slightly over the mass cut, they have a higher scatter at fixed mass than does the full sample at redshift zero.

Only the emission measure $\hat{Q}$ has a scatter with fixed mass that decreases towards

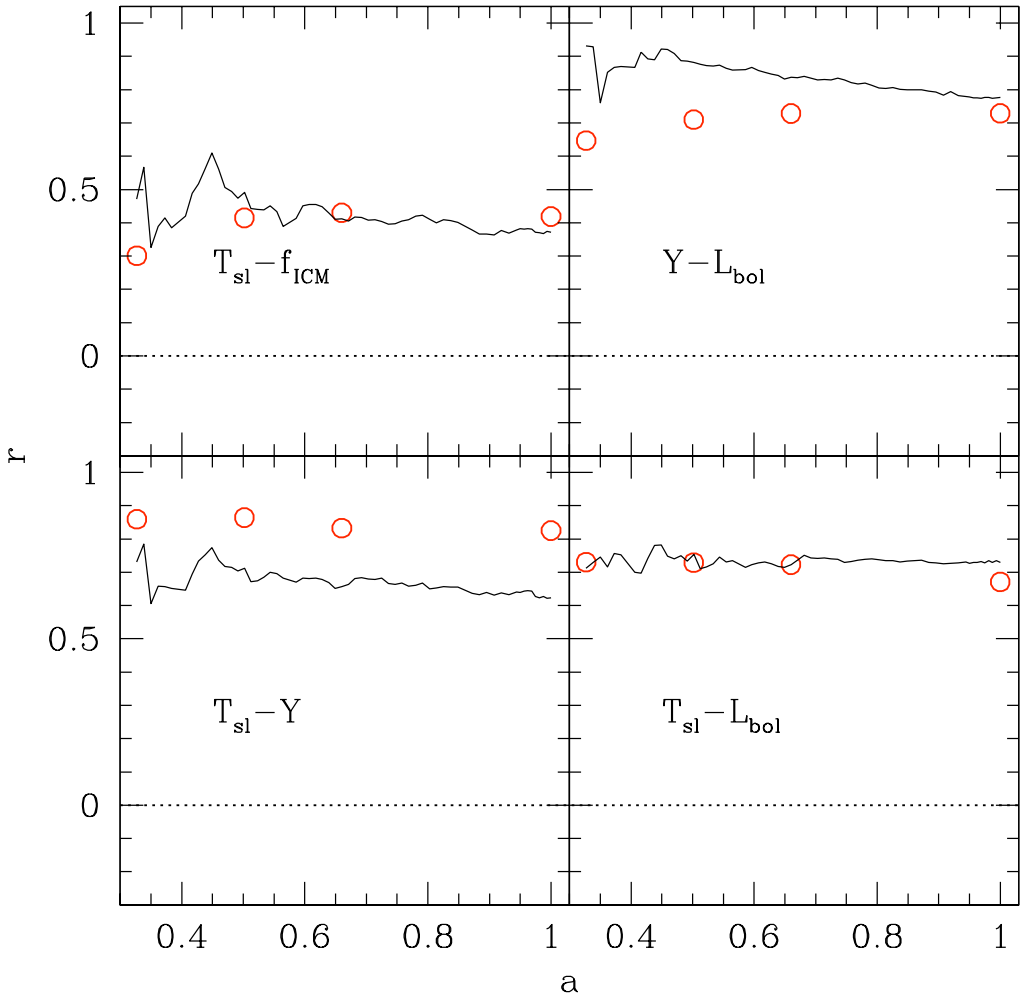

Figure 4.13. Four pairs of signals which show little to no evolution in the correlation coefficient. The black, solid line denotes the PH simulation, and the red, open points the GO simulation.

higher redshift. This is perhaps surprising, particularly as the scatter in c at fixed mass increases towards higher redshift.

Moving on to the off-diagonal elements, most pairs of signals show little evolution in the correlation coefficient with redshift. Figure 4.13 shows four typical pairs with little evolution. Even as the physical density of halos changes with redshift, we see that the interplay of Y and L or $T_{\rm sl}$ and $f_{\rm ICM}$ does not change. We see particularly little evolution in pairs of signals in the PH simulation.

We do see evolution in a few signal pairs, notably between $\sigma_{\rm DM}$ and other signals in the GO simulation. It is notable that there are several pairs of signals – such as

$\sigma_{\rm DM} - T_{\rm sl}$ and $f_{\rm ICM} - Y$ – in which the correlation evolves in the GO simulation, but not in the PH simulation. Furthermore, for $\sigma_{\rm DM} - L_{\rm bol}$, we see evolution in both simulations, but in opposite directions. The evolution of these pairs is shown in Figure 4.14.

The correlation between $\sigma_{\rm DM}$ and the SZ and X-ray signals increases towards high redshift in the GO simulation. This is due to the increase in $\hat{Q}$ with time at fixed mass in the GO simulation, as shown in Figure 4.5. As $\hat{Q}$ is a measure of the clumpiness of the gas, we see that the gas in the GO simulation develops more substructure with time. These clumps of cold gas affect the X-ray and SZ signals in the GO simulation, particularly L and $T_{\rm sl}$. While $\sigma_{\rm DM}$ remains a tight tracer of halo mass, L and $T_{\rm sl}$ depend on both the halo mass and the halo substructure.

Although $\hat{Q}$ also increases with time in the PH simulation, its normalization at all redshifts is much lower than in the GO simulation. Hence, the substructure of the gas does not contribute much to the $T_{\rm sl}$ or L measures in the PH simulation, and there is little evolution of their correlation with $\sigma_{\rm DM}$.

4.4.4 Implications of the Covariance

We discuss the implications for future cluster surveys given the scatter in Y at fixed mass in both simulations, and the covariance between Y and $L_{\rm bol}$ at fixed mass.

After calculating covariance, we can determine the ideal signal (or pair of signals) for multiwaveband cluster surveys. Using σ to denote the scatter in the signal at fixed mass, and r to denote the correlation coefficient, our covariance matrix can be written as

$$C = \begin{pmatrix} \sigma_1^2 & r\sigma_1\sigma_2 \\ r\sigma_1\sigma_2 & \sigma_2^2 \end{pmatrix}. \tag{4.17}$$

To find the scatter in mass at a fixed signal, we take the inverse of the covariance matrix,

$$C^{-1} = (1-r^2)^{-1} \begin{pmatrix} \frac{1}{\sigma_1^2} & -\frac{r}{\sigma_1\sigma_2} \\ -\frac{r}{\sigma_1\sigma_2} & \frac{1}{\sigma_2^2} \end{pmatrix}. \tag{4.18}$$

If we define the scatter in mass for a fixed signal as $\sigma_\mu = \sigma/b$, where b is the slope of

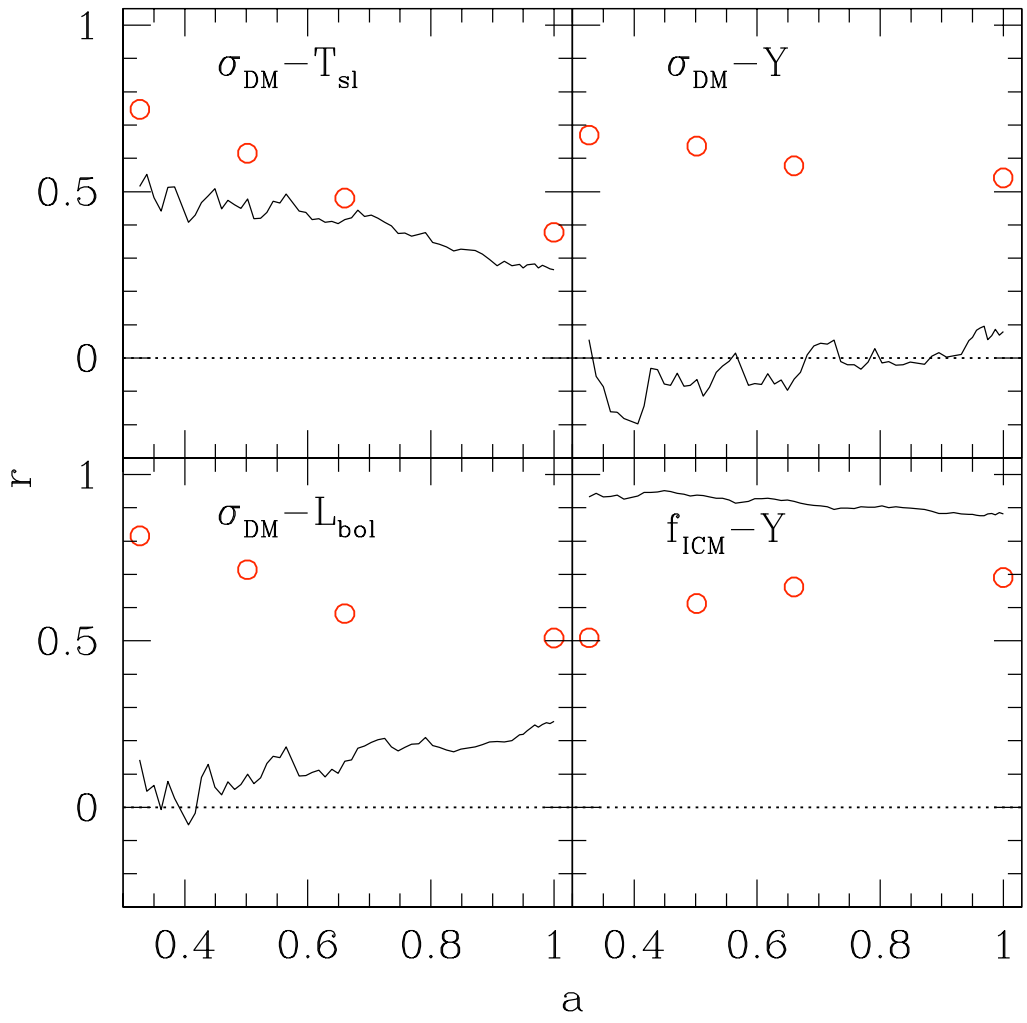

Figure 4.14. Four pairs of signals which show some degree of evolution in the correlation coefficient, particularly in the GO simulation. The black, solid line denotes the PH simulation, and the red, open points the GO simulation.

Cluster Property	$\sigma_{\rm DM}$	$T_{\rm sl}$	$f_{\rm ICM}$	Y	$L_{\rm bol}$	PH	GO
$\sigma_{\rm DM}$	–	0.12	0.12	0.075	0.12	0.12	0.12
$T_{\rm sl}$	0.10	–	0.35	0.050	0.26	0.12	0.38
$f_{\rm ICM}$	0.11	0.12	–	0.054	0.21	0.28	0.12
Y	0.062	0.069	0.041	–	0.066	0.069	0.075
$L_{\rm bol}$	0.09	0.10	0.09	0.069	–	0.10	0.26

Table 4.6. The redshift zero mass scatter for each pair of signals, with the results from the PH simulation in the lower, left-hand half, and the results from the GO simulation in the upper, right-hand half, as in Figure 4.11. The mass scatter for the individual signal is listed on the right-hand side of the table.

the power law, then the inverse mass variance for a pair of signals is

$$\Sigma^{-2} = (1 - r^2)^{-1}(\sigma_{\mu 1}^{-2} + \sigma_{\mu 2}^{-2} - 2r\sigma_{\mu 1}^{-1}\sigma_{\mu 2}^{-1}). \tag{4.19}$$

We use Equation 4.19 to derive the scatter in mass for a pair of signals from our covariance matrix, and present the numbers in Table 4.6.

We present $\Sigma/\sigma_{\mu 1}$ as a function of the scatter ratio $(\sigma_{\mu 2}/\sigma_{\mu 1})$ for several values of the correlation coefficient in figure 4.15. For signals which are positively correlated, the improvement in the mass scatter when using both signals is extremely sensitive to the ratio of the signals' scatters at fixed mass.

The scatter in mass for a pair of signals depends on the scatter in mass at each signal, but in general a pair of signals with a high correlation coefficient with have a low mass scatter when used as a joint mass proxy. In the PH simulation, the correlation coefficient between L and Y is $r = 0.78$, and the scatter in mass for the pair of signals is 6.9%. This is a significant improvement from the scatter in mass for only using $L_{\rm bol}$ (11%) or only Y (7.5%). Given the high covariance between $L_{\rm bol}$ and Y, future multiwaveband surveys requiring both SZ and X-ray detections should have a good mass selection function.

The covariance between a pair of signals does not only affect the mass selection of the survey. All derived properties will depend on the covariance between the selection signal and the derived property. For example, Nord et al. (2008) present the $L - T$ relation for a range of correlation coefficients, given a flux cut in a survey. Both simulations have a significantly non-zero correlation coefficient between L and T:

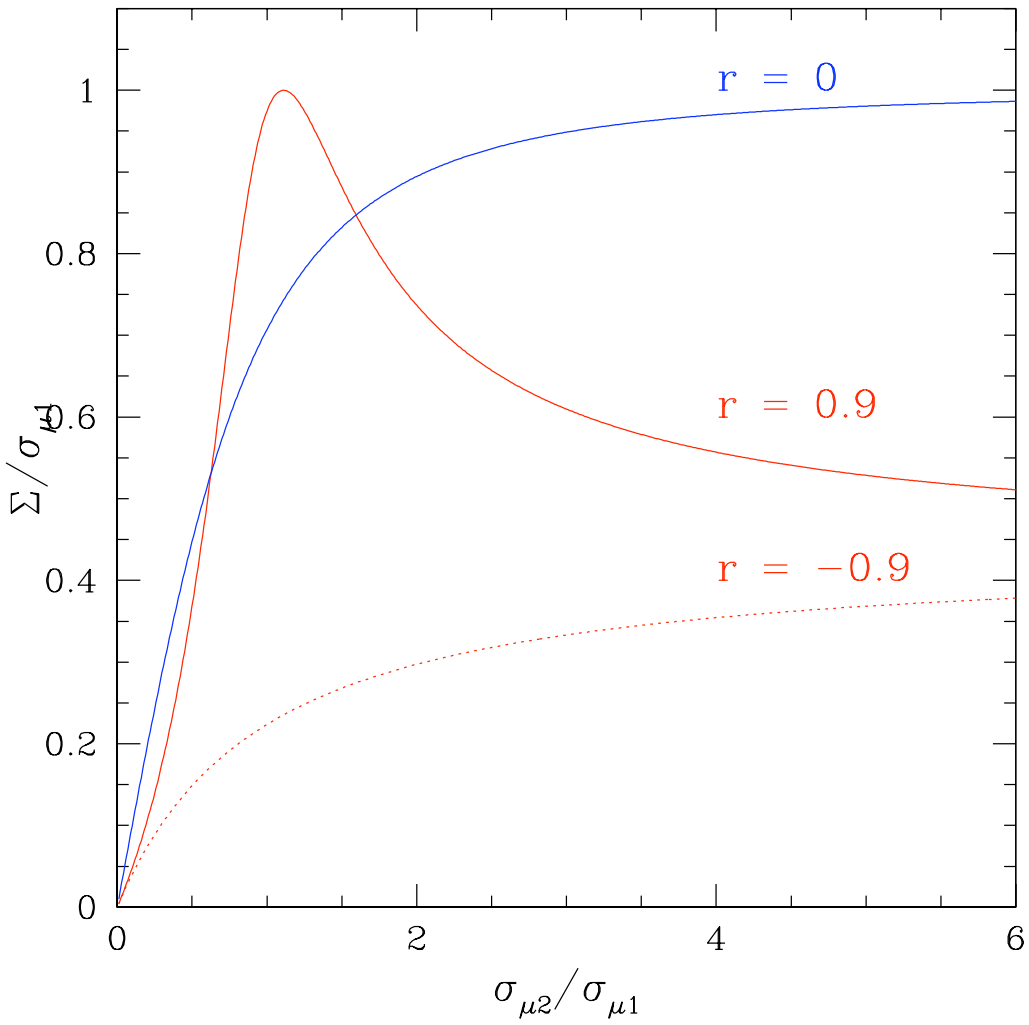

Figure 4.15. For a range of correlation coefficients, the ratio of the combined mass scatter with one signal's scatter against the ratio of the two signals' scatter. This illustrates the gains possible from using two signals in a cluster survey, given their covariance and individual mass scatter.

$r = 0.73$ in PH and $r = 0.78$ in GO .

4.5 Conclusion

We have presented statistical properties from a pair of hydrodynamic simulations of cosmological volumes, with two different treatments of the gas physics. In comparing the mean scaling relations of the two simulations, we see how preheating in our PH simulation causes deviations from a scenario where only gravity and shock heating affects the gas. As the preheating models the effects of astrophysical processes, such as heating from AGN and star formation, comparison with observations can tell us about the quantity of energy injected into galaxy clusters. The largest effect of the preheating in the PH simulation is the drastic reduction of the baryon fraction in the PH halos compared to the GO halos. This lower baryon fraction drives much of the difference in the scaling relations between the PH and GO simulations. As the high-mass halos in the PH simulation are similar to the halos in GO in both normalization and scatter in the $f_{\rm ICM} - M$ relation, we see that by redshift $z = 0$, the high-mass halos are nearly impervious to the underlying cluster physics. At fixed mass, the halos in PH are also hotter than the GO halos, but this effect is stronger at the low mass end.

When compared to observations, we see a high degree of agreement between the PH halos and observations including temperature, luminosity, baryon fraction, and mass. This agreement is particularly good for observations which have been core-excised. While we do not directly simulate the complicated astrophysics in galaxy clusters, such as star formation and AGN activity, a simple preheating at redshift $z = 4$ models these effects outside the core quite well. With the large volume of our simulation, we produce statistically-significant measures of the mean scaling relations of cluster properties with mass. We calculate the covariance between cluster signals, which is essential for calibrating the selection function of multiwaveband surveys. We also discuss how requiring two signals for a survey detection can improve the scatter in mass. We consider the statistics of the PH model to be a good description of a core-excised population.

We intend to extend this work with merger histories of the PH halos. With merger histories, we can calculate the median lag time between a merger event and the change in the X-ray and SZ signals. This will allow us to produce a physical explanation of the terms in the covariance matrix. Furthermore, tracing merger histories will illustrate if cluster surveys are biased towards clusters in various dynamical states.

CHAPTER 5

The Effect of Gas Physics on the Halo Mass Function

5.1 Introduction

Deep cluster surveys offer the promise of tightly constraining cosmological parameters, including the nature of dark energy (Holder et al., 2001; Levine et al., 2002; Majumdar & Mohr, 2003; Lima & Hu, 2004b, 2005b; Younger et al., 2006; Sahlén et al., 2008). Realizing this promise requires accurate calibration of the expected counts and clustering of massive halos, along with a careful treatment of how halo mass relates to the signals observed by such surveys. This logical division is reflected by two long-standing threads of effort, one focused on the emergence of massive structures from gravity and the other focused on scaling relations of multiple signals within the population of massive halos.

The fact that 17% of clustered matter in the universe is baryonic ties these threads together. Non-gravitational physics is required in massive halos, not simply to create galaxies (White & Rees, 1978) but also to reproduce scaling behavior of the hot, intracluster medium (ICM) observed in X-rays (Evrard & Henry, 1991; Borgani et al., 2001; Reiprich & Böhringer, 2002; Stanek et al., 2006; Nagai et al., 2007). If a significant fraction of halo baryons become spatially segregated from the dark matter, either condensed within galaxies or disbursed from non-gravitational heating, then the gravitational development of massive structures will be altered, perhaps at the $\sim 10\%$ level, under strong baryonic effects.

The spatial number density of halos, or mass function, expected from Gaussian random initial conditions was originally derived using a mix of analytic arguments

and numerical simulations (e.g. Press & Schechter, 1974; Bond et al., 1991; Sheth & Tormen, 1999a). Modern efforts focus on providing fitting functions of increasing statistical precision (Jenkins et al., 2001; Warren et al., 2006; Tinker et al., 2008). The recent Tinker et al. (2008) mass function (hereafter TMF), calibrated to a wide range of cosmological simulations that include gas-dynamic, Marenostrum simulations (Yepes et al., 2007; Gottlöber & Yepes, 2007), has pushed statistical errors to the level of 5%.

To date, however, there have been few gas-dynamic simulations that include a non-gravitational treatment of baryonic processes in volumes large enough to provide good statistics for high-mass halos. Calibration of the mass function at the level of the Tinker et al. (2008) using hydrodynamic simulations is too expensive to be feasible in the near-term. A less computationally expensive technique is to compare realizations of fixed initial conditions evolved with different baryonic physics. Jing et al. (2006) and Rudd et al. (2008) employ this approach to study baryonic effects on the matter power spectrum, finding 2-10% modifications of the matter power spectrum at scales $k \sim 1h\,\mathrm{Mpc}^{-1}$. Rudd et al. (2008) finds a halo mass function that is enhanced by $\sim 10\%$ relative to the dark-matter only case. Neither set of simulations were sufficiently large to properly probe rich cluster scales, however.

In this letter, we take a similar approach to examine the effect of non-gravitational, baryonic physics on the cluster mass function. Specifically, we consider two pairs of gas-dynamic simulations, each comprised of a treatment of the gas with gravity and shock heating only and a second, more complicated treatment. One pair are Millennium Gas Simulations (Hartley et al., 2008, MGS hereafter), with SPH gas dynamics under Gadget-2 (Springel, 2005b), and the second pair are adaptive-mesh ART simulations from Rudd (2007). As the two simulations in each pair have the same initial conditions, we infer the effects of baryonic physics by comparing halos in the more detailed simulations with their gravity-only counterparts. The outline of this paper is as follows: in Section 5.2, we discuss the various simulations and their bulk cluster properties, comparing them to observations. Section 5.3 compares halo masses between corresponding halos in each pair of simulations, and discusses the

effect on the total mass function. All halos masses are identified as M_{500}, the mass of a spherical halo with radius r_{500} and mean density $500\rho_c(z)$, where $\rho_c(z)$ is the critical density of the universe.

5.2 Simulations and Halo Samples

We use two pairs of gas dynamic simulations, each pair run from a single set of initial conditions and differing only in the included physical processes. Our baseline simulations are evolved with only gravity, shock heating, and adiabatic processes acting on the gas (hereafter `GO`) and a second has more complicated treatment of the gas physics discussed below.

Halos in all simulations are identified as spherical regions, centered on the peak of the dark matter distribution, where the mean enclosed density is $500\rho_c(z)$. Our analysis focuses on $z = 0$ and $z = 1$ samples, redshifts that roughly bracket the range important for dark energy studies. When calculating the bulk cluster properties, we exclude from our sample halos that overlap with more massive neighbors; however, to remain consistent with Tinker et al. (2008) halos that overlap but whose centers lie outside their respective virial radii are included in the mass function analysis.

5.2.1 Millennium Gas Simulation

The Millennium Gas Simulations (hereafter MGS) are a pair of resimulations of the Millennium Simulation (Springel et al., 2005), a high-resolution, dark-matter-only simulation of a $500\,h^{-1}$ Mpc cosmological volume. Like the original Millennium Simulation, the simulations were run with GADGET-2, which treats the gas dynamics with smoothed particle hydrodynamics (SPH) (Springel, 2005b). The MGS runs use a down-sampled version of the initial conditions of the Millennium simulation, with 5×10^8 dark matter particles, each of mass $1.4 \times 10^{10}\ h^{-1}\ \mathrm{M}_\odot$, and 5×10^8 SPH gas particles, each of mass $3.1 \times 10^9\ h^{-1}\ \mathrm{M}_\odot$. This mass resolution is about 20 times coarser than the original Millennium simulation, and the gravitational softening length of $25\,h^{-1}$ kpc is correspondingly larger. The cosmological parameters match the Millennium Simulation: $(\Omega_m,\ \Omega_b,\ \Omega_\Lambda,\ h,\ n,\ \sigma_8) = (0.25,\ 0.045,\ 0.75,\ 0.73,\ 1.0,$

0.9).

Complementing the aforementioned GO realization is an MGS simulation with cooling and preheating, denoted as the PH model. Preheating is a simple approximation that assumes high redshift galaxy formation feedback drove the proto-ICM gas to a fixed entropy level, after which the ICM evolves under hierarchical gravity (Evrard & Henry, 1991; Kaiser, 1991; Bialek et al., 2001). In our implementation, the entropy of each gas particle is instantaneously boosted to 200 keV cm^2 at $z = 4$. The gas is allowed to radiatively cool thereafter using the cooling function of Sutherland & Dopita (1993), but the cold gas fraction is very small. The entropy level of the PH model is tuned to match bulk X-ray observations of clusters at redshift zero, as we discuss shortly.

For both MGS models, we calculate bulk cluster gas properties with primary halos of mass $M_{500} \geq 5 \times 10^{13}\, h^{-1}\ \mathrm{M}_\odot$, yielding sample sizes of 2527 (PH) and 3446 (GO) at $z = 0$ and of 475 (PH) and 818 (GO) at $z = 1$. For the mass function analysis, we extend the mass cut to $M_{500} \geq 10^{13}\, h^{-1}\ \mathrm{M}_\odot$.

5.2.2 ART Simulations

Our second set of models are simulated using the distributed-parallel hydrodynamic ART code (Rudd et al., 2008; Rudd, 2007). The simulations evolve a $240^3 h^{-3}\mathrm{Mpc}^3$ volume of a WMAP3-motivated cosmological model with parameters, (Ω_m, Ω_b, Ω_Λ, h, n, σ_8) = (0.25, 0.042, 0.75, 0.73, 0.95, 0.8). The baseline GO simulation was performed using 512^3 dark matter particles with mass $m_p \sim 5.9 \times 10^9\, h^{-1}\ \mathrm{M}_\odot$ and allow for 4 levels of refinement achieving a minimum cell size of $240\ h^{-1}\ \mathrm{Mpc}/(512 \times 2^4) \approx 29\, h^{-1}\,\mathrm{kpc}$. The ART-GO simulation has 244 halos over a mass cut of $5 \times 10^{13}\, h^{-1}\,\mathrm{M}_\odot$. We then selected the 13 most massive halos in the simulation volume at $z = 0$, and resimulated at 1024^3 effective resolution ($m_p \approx 7.4 \times 10^8\, h^{-1}\ \mathrm{M}_\odot$) the regions within $5r_{\mathrm{vir}} \sim 5 - 10\, h^{-1}$ Mpc surrounding each cluster center. This simulation includes prescriptions for star formation and metal-dependent radiative cooling described in Rudd (2007). For this simulation, the same 512^3 uniform mesh was used, but in the high-resolution regions 7 levels of refinement were used for a peak spatial resolution

of $\approx 3.6\,h^{-1}$ kpc.

5.2.3 Baryon Census

We begin by exploring the bulk properties of baryons in the massive halo samples as a means of assessing the viability of the different physical treatments.

Figure 5.1 shows baryon mass fractions within r_{500}, normalized to the universal baryon fraction Ω_b/Ω_m. In the `GO` simulations, all the baryons are in the hot intracluster medium phase, so that $f_b = f_{\rm ICM}$. In the `CSF` simulation, gas is removed from the hot phase through radiative cooling and converted to stars. For these halos, we plot both the ICM mass fraction $f_{\rm ICM}$ and the total baryon fraction, $f_b = f_{\rm ICM} + f_{\rm cond}$, where condensed baryons, $f_{\rm cond}$, includes both stars and cold gas ($T < 2 \times 10^5 K$). Although the `PH` model allows radiative cooling, the fraction of cold gas in our halo samples is very small, less than two percent of the baryons.

The `GO` simulations display constant baryon fractions that are slightly suppressed from the universal mean value. The level of suppression is somewhat larger in the MSG halos compared to the ART sample, which is consistent with the difference between SPH and grid codes reported by Kravtsov et al. (2005). The mass-limited samples have average baryon fractions at $z = 0$ of $f_b = 0.89 \pm 0.025$ and 0.93 ± 0.038, respectively. The MGS baryon fractions are consistent with those in SPH simulations done at similar resolution and measured within $\Delta_c = 200$ by Crain et al. (2007) and Ettori et al. (2006).

The baryon distributions in the `PH` and `CSF` simulations are more complicated. In the `PH` case, the entropy increase at $z \sim 4$ causes the gas to expand, especially in lower-mass halos for which the characteristic entropy is lower, and raises the sound speed throughout the proto-ICM. The latter effect pushes the effective shock radius to larger values compared to the purely gravity-driven case (Voit et al., 2003). As a result, lower-mass halos retain a smaller fraction of their baryons within r_{500}, leading to the mass-dependence seen in Figure 5.1. Since the characteristic halo entropy increases with time at fixed mass, the mean ICM gas fraction at fixed mass increases from $z = 1$ to $z = 0$ in the `PH` halos. At $z = 0$, the highest mass halos have baryon

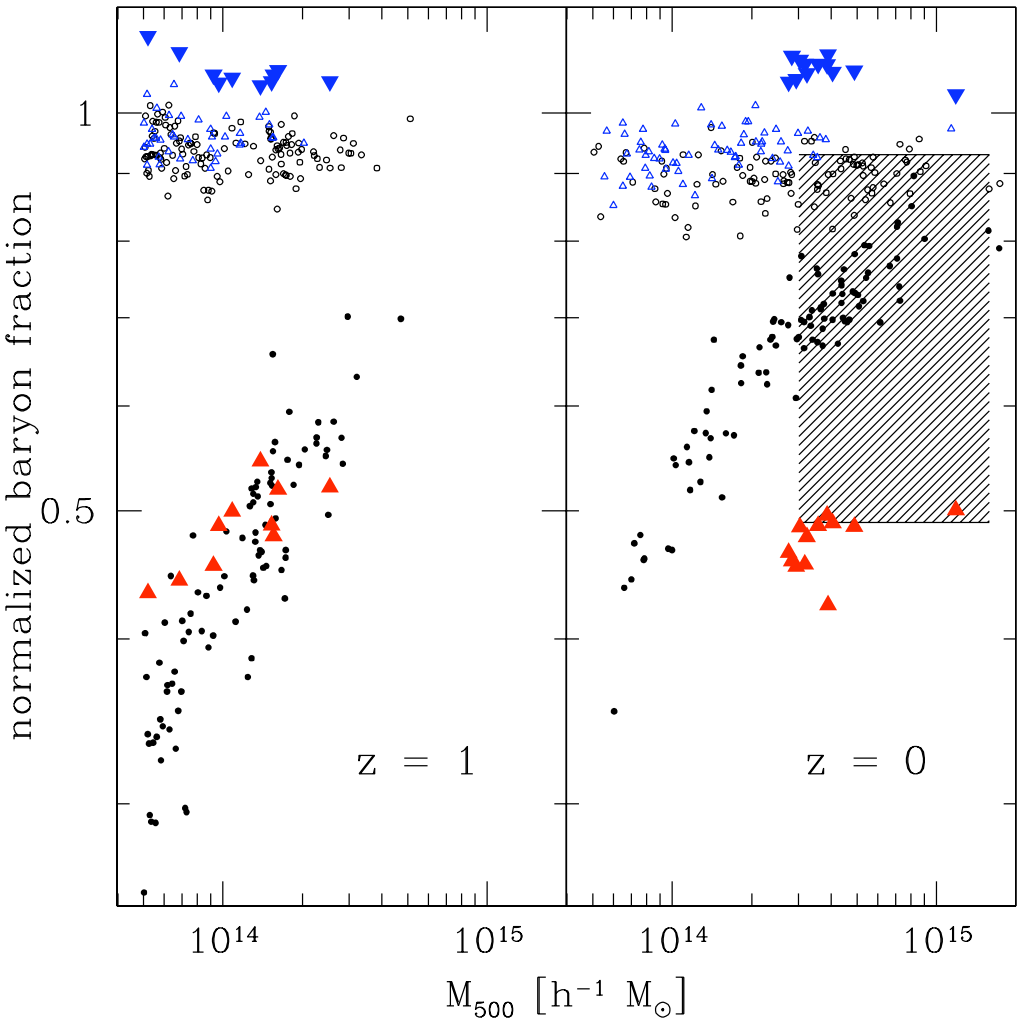

Figure 5.1. Baryon fractions as a function of total halo mass at $z = 1$ (left panel) and $z = 0$ (right panel) are shown for the MGS halo samples in the `GO` (open circles) and `PH` (filled circles) treatments and for the ART samples in the `GO` (open triangles) and `CSF` (filled triangles) cases. For the latter, regular triangles show the ICM mass fraction while inverted triangles show the total baryon fraction (gas plus stars) within the halos. The shaded region shows the 90% confidence range of the mean, observed ICM mass fraction inferred for local, $kT > 4\,\mathrm{keV}$ clusters by Vikhlinin (2006). For clarity, only a subset of the MGS samples are shown for masses below $4 \times 10^{14} M_{\odot}$.

fractions suppressed by only 10% relative to the GO treatment.

In the CSF halos, the hot gas fraction, $f_{\rm ICM}$, is comparable to that in the PH clusters of similar mass at $z = 1$. However, the total baryon fraction in these halos is close to universal, due to the contribution of cold gas and stars. Unlike the PH models, the ICM mass fraction does not evolve with time, remaining approximately constant at $\approx 50\%$ from $z = 1$ to $z = 0$, even as the clusters themselves grow by a factor of two in total mass. The total baryon fraction grows by 4% due primarily to the small increase in the ICM. The stellar component grows significantly from $\sim 40\%$ to $\sim 47\%$ but is balanced by a corresponding decrease in the fraction of cold gas from $\sim 10\%$ to $\sim 4\%$.

As an empirical test of the models, we show in Figure 5.2 the scaling between bolometric luminosity $L_{\rm bol}$ and spectral temperature $T_{\rm sl}$ for the $z = 0$ halo samples of the MGS and ART–CSF simulations. The models are compared to a local sample of clusters compiled by Hartley et al. (2008). As the local sample extends only to modest redshifts, $z \lesssim 0.2$, we do not apply evolutionary corrections to the observations.

For the models, we use the analytic approximation of Bartelmann & Steinmetz (1996) to compute L_{bol} within r_{200} of each halo. For all MGS halos we compute spectroscopic temperatures, $T_{\rm sl}$, using the expression in Mazzotta et al. (2004). This expression is insufficient for large quantities of low-temperature gas, so, for the CSF clusters, we use instead the method of Vikhlinin (2006). Additionally, for the CSF clusters we exclude gas within $0.1r_{200}$ and within dark matter substructures to crudely reproduce the clump removal procedure applied in Nagai et al. (2007) and Rasia et al. (2006). The cores of the CSF clusters have unphysical cooling flows that must be excised; our choice of core radius affects the position of a cluster on the $L - T$ relation, but not the normalization of the overall $L - T$ relation. Applying this simple analysis proceedure to the simulated clusters used in Nagai et al. (2007) give temperatures that differ by $\sim 10\%$ or less from the mock *Chandra* analysis. The measured X-ray quantities are sensitive to the choice of innermost radius, with larger cuts leading to simultaneously lower measured $L_{\rm bol}$ and $T_{\rm sl}$.

Both of the non-gravitational physics models provide a better match to the ob-

served data than the GO simulation. As discussed in Hartley et al. (2008), the PH halos match the slope and normalization of the observed $L - T$ relation well. The observed scatter is much larger, however, due primarily to the existence of cool cores in real clusters.

The slope of the CSF halos also agrees with the observations, but the normalization and scatter are not well matched to the data. The normalization offset is partly due to the lower gas fraction seen in Figure 5.1, but the spectral temperatures also play a role. As discussed in Borgani et al. (2004) and Nagai et al. (2007), the temperature profile of the hot phase is steeper than observed in cluster cores, resulting in enhanced $T_{\rm sl}$ values.

In summary, we have shown that both the PH and CSF simulations offer a reasonable match to the form of the $L - T$ relation, but the overall baryon content of halos differs substantially between the two. In the CSF simulation, star formation is overly efficient, so that nearly 50% of the baryons are in stars rather than in the hot phase. In the PH simulation, the stellar fraction is entirely neglected, but the net heating effect of early galaxy formation is assumed to be large enough to drive the halo baryon fraction substantially below the global value. Neither of these treatments is fully consistent with observations, but they represent two extreme approximations for the true behavior. We next examine the effects that these treatments have on halo mass.

5.3 Halo Masses and the Mass Function

Since both pairs of simulations are evolved from the same initial conditions, we are able to match halos between the realizations performed under the two physical treatments. In Figure 5.3, we show the fractional shift in mass that occurs under the PH and CSF treatments, relative to the respective GO model, as a function of GO halo mass at redshifts $z = 0$ and 1. The mean mass shift are plotted for MGS halos in mass bins. Individual clusters are plotted for the ART simulations at $z = 0$ and $z = 1$.

The PH halos experience a substantial decrease in mass relative to the GO halos. The magnitude of the $z = 0$ fractional mass shift depends on halo mass, declining

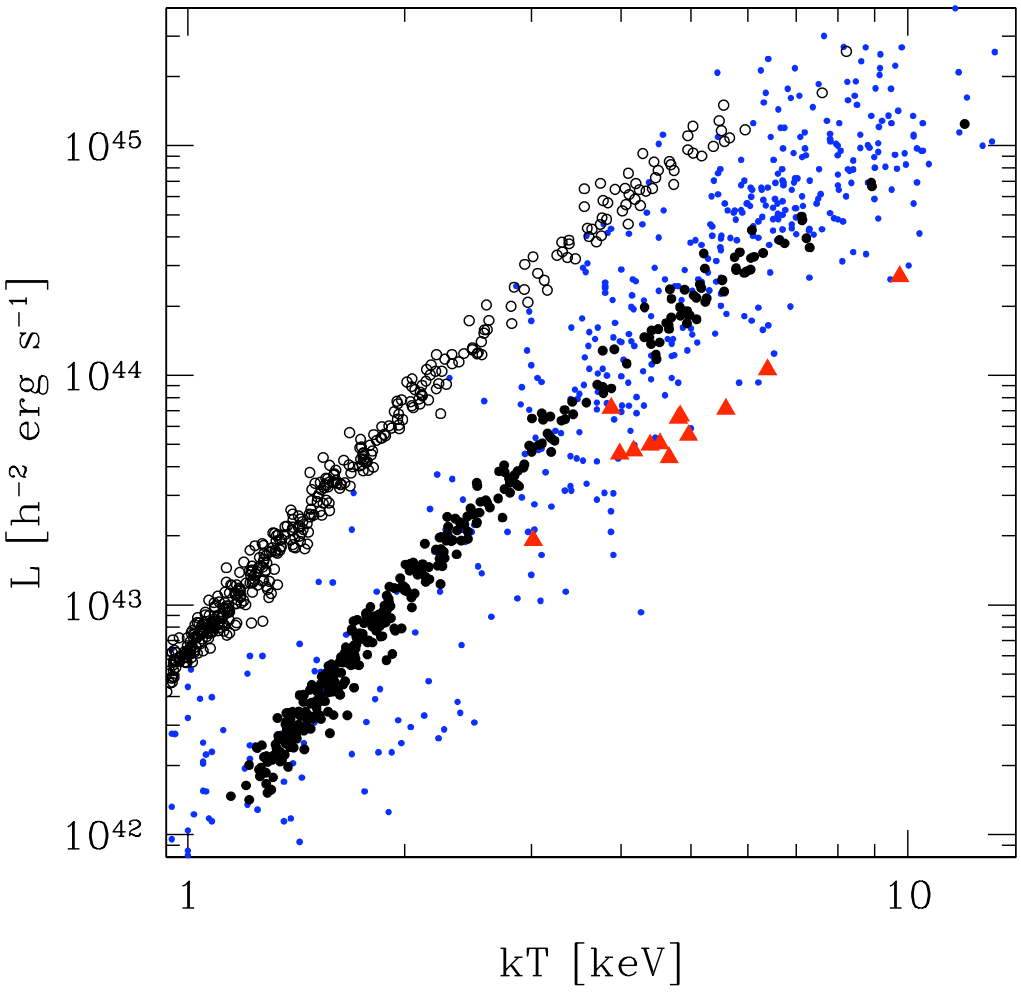

Figure 5.2. The $L_{\rm bol} - T_{\rm sl}$ relations for the MGS–`GO` (open cirles), MGS–`PH` (filled circles), and ART–`CSF` (filled triangles) samples are compared to observations (small points) compiled by Hartley et al. (2008). The MGS halos are sub-sampled as in Figure 5.1.

from 15% at $10^{14}h^{-1}$ $M_\odot$ to 5% at $10^{15}h^{-1}$ $M_\odot$. Although these mass shifts are mostly due to the change in gas fraction, there is also a difference in dark matter structure that enhances the shift. All but the most massive ART–CSF halo show increased mass relative to the respective GO halos. At the mean mass of the sample at $z = 0$, $3 \times 10^{14}\ h^{-1}\ M_\odot$, the mean fractional mass shift is 0.162 ± 0.022. Approximately 2% of this shift is due to the increase in baryon mass. The remainder is due to the change in halo structure brought about by baryon cooling (Gnedin et al., 2004; Nagai, 2006).

These mass shifts depend on the choice of scale, as shown in the inset of Figure 5.3. For comparison with the ART–CSF halos we plot the mean mass profile for MGS halos in the range $1 - 3 \times 10^{14}\ h^{-1}\ M_\odot$. Within the core, the mass difference between matched halos in the MGS simulations is nearly 20%, but the mass difference approaches zero on scales significantly larger than r_{200}. In the ART simulations, we also see that the mass shift is a strong function of scale: within the core it is very high, $\sim 80\%$, and approaches zero beyond r_{200}. Because of this scale dependence, the magnitude of the mean mass shift and its evolution with redshift is sensitive to our choice of $\Delta = 500\rho_c(z)$.

The shifts in mass seen with complex physical treatments will lead to changes in the mass function relative to the GO models. For both MGS simulations and the ART–GO run, we compute binned space densities directly from the simulation counts. Figure 5.4 plots these mass functions at redshifts $z = 0$ and $z = 1$, and compares them to the TMF expectations for mean density contrasts equivalent to $\Delta_c = 500$, shown by the solid lines. To account for differences in cosmology (primarily the difference in σ_8) we calculate the TMF for both cosmologies. From a fixed number density, we find the mass shift between the two cosmologies, and apply it to the ART–GO data for simple comparison with the MGS mass functions.

The redshift zero GO mass functions match the TMF prediction quite well. The top panels show the fractional difference in counts between the simulations and the TMF, with the 90% statistical calibration uncertainty of the latter shown by the solid, horizontal lines. We include 90% uncertainties on the data points: jackknife uncertainties as a measure of cosmic variance for the ART–GO sample, and Poisson

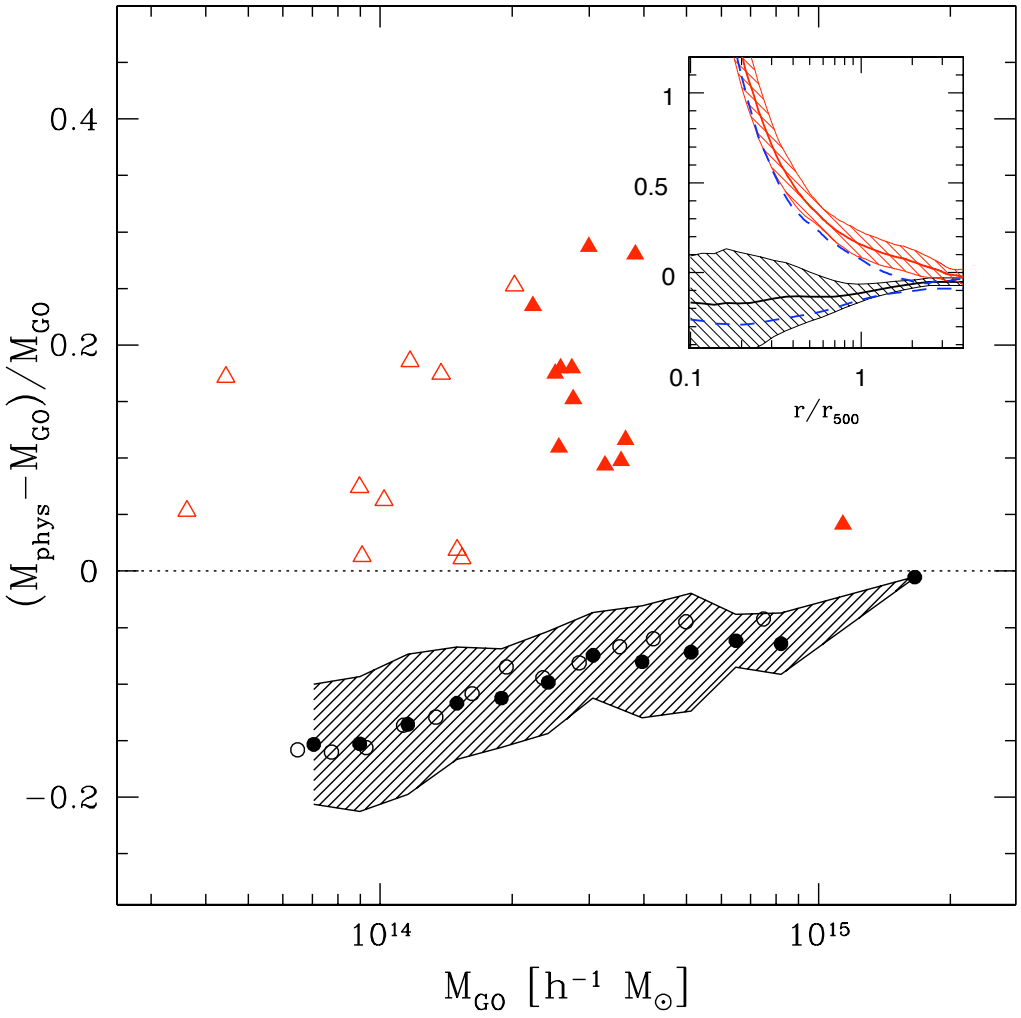

Figure 5.3. Fractional mass difference in halo mass with respect to the GO realization. Circles show the mean shift for the PH halos at $z = 0$ (filled) and $z = 1$ (open). Triangles show individual CSF halos at $z = 0$ (filled) and $z = 1$ (open). The inset panel plots the cumulative radial mass difference for CSF halos (red) and PH halos (black) at $z = 0$ (solid, with $1-\sigma$ scatter) and $z = 1$ (dashed).

uncertainties for the larger volume of the MGS simulation. The counts of both the ART and MGS models under GO treatment lie within the TMF expectations at $z = 0$.

At all masses, the PH halo mass function is suppressed with respect to the GO halo mass function, at a statistically significant level. At $M_{500} \sim 10^{14}\ h^{-1}\ \mathrm{M}_{\odot}$, the number density of PH halos is 20% lower than the TMF prediction, a 4σ shift relative to the 5% TMF calibration error. At the very high mass end, $\sim 10^{15} M_{\odot}$, there is consistency with the TMF expectations.

We do not have a complete mass function from the CSF simulation. However, we can anticipate the shift in halo number based on the mean shifts in halo mass presented above. Since the ART–GO models are consistent with the TMF, we derive CSF expectations by shifting the mass by fractional values given by the 90% confidence range of the mean shifts shown in Fig 5.3, meaning $\Delta M/M = 0.117 \pm 0.056$ at $z = 1$ and 0.162 ± 0.035 at $z = 0$. We apply these shifts at mass scales probed by the CSF halos, $M_{500} > 2 \times 10^{14}\ h^{-1}\ \mathrm{M}_{\odot}$. At $z = 0$, the positive shift in halo mass implies upward deviations in number density from the TMF expectation, at levels ranging from 10% to 60%.

5.4 Discussion and Conclusion

Calibrations of the halo space density from ensembles of N-body and dissipationless gas dynamic simulations now have very small statistical uncertainties, $\sim 5\%$ in number (Tinker et al., 2008). At the high-mass end, this level of precision in number is equivalent to a precision in halo mass at the 2% level. Since baryons represent 17% of the matter density, complex gas dynamics associated with galaxy formation physics could plausibly lead to effects on halo masses of more than a few percent. In this letter, we demonstrate that shifts approaching 10% in mass are possible, and that the sign of this effect is not yet understood.

We use two extreme treatments of gas physics that are likely to bracket the range of behavior due to astrophysical processes in galaxy clusters. A simple assumption of preheating reduces the local baryon fraction in halos, thereby suppressing their mass at levels ranging from 15% at $10^{14}\ h^{-1}\ \mathrm{M}_{\odot}$ to 5% at $10^{15}\ h^{-1}\ \mathrm{M}_{\odot}$. A more complete

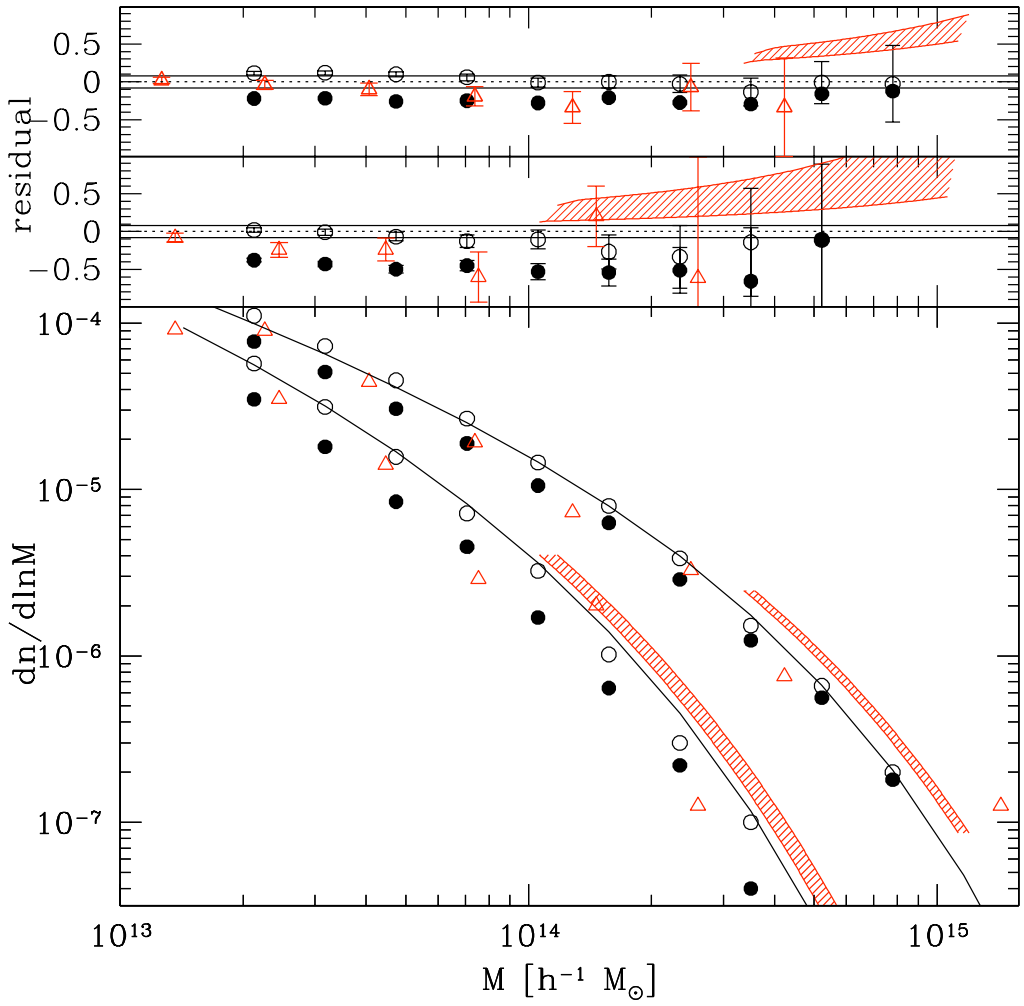

Figure 5.4. The lower panel shows the halo mass functions for the PH (solid circles) and GO (open circles) versions of the MGS and the ART–GO model (open triangles) at redshifts $z = 0$ (upper) and $z = 1$ (lower). The solid black lines are the TMF expectations at these redshifts. Red bands shows the 90% confidence regions anticipated by the shifts in halo mass for the ART–CSF treatment. The panels above show the fractional difference in number counts between the measured mass functions and the TMF, at $z = 0$ (top) and $z = 1$ (middle). We plot 90% jackknife errors for the ART–GO model, and Poisson errors for the MGS. Note that we have used the TMF for scaling the ART mass functions to match the MGS cosmology.

physics treatment with cooling and star formation increases the local baryon fraction and deepens the halo potential, thus enhancing halo mass, by an average of 12% at $10^{14.5}h^{-1}$ $M_\odot$. The effects of cooling and star formation on halo mass are qualitatively consistent with the systematic enhancement in small-scale power seen in previous simulations (Jing et al., 2006; Rudd et al., 2008). In both of the complex physical treatments we consider, the shifts in mass lead to statistically significant offsets in cluster counts from the TMF expectations. These shifts in mass depend on the choice of scale used in defining halos: in both treatments, the mass shifts are larger when identifying halos via higher density contrasts.

Although both the `PH` and `CSF` simulations provide fair matches to the mean observed $L - T$ relation, implying the structure of the hot gas phase is nearly correct, neither describes well the stellar content of clusters. The `PH` simulation ignores galaxies while the `CSF` simulation converts nearly $\sim 50\%$ of baryons into a large stellar component. This is significantly larger than the $\sim 14\%$ observed by Lin et al. (2003), and the $\sim 15 - 20\%$ observed by Gonzalez et al. (2007) when including intracluster light. However, the observational uncertainties on these measurements are still quite large. Although it is tempting to dismiss the `PH` model due to its lack of detailed physics, a growing body of observations, particularly the ubiquity of strong winds in moderate redshift DEEP2 galaxies (Weiner et al., 2008) and the remarkably simple evolution to $z = 1.4$ of the color of red sequence galaxies seen in the Spiter/IRAC Shallow Survey (Eisenhardt et al., 2008), provide supporting evidence for a scenario in which the fireworks associated with galaxy formation in clusters is both rapid and effective.

Improvements in the physical and computational modeling of cooling and star formation are needed to match the full set of observational constraints on the baryonic mass components of cluster halos. We have shown here that varying these treatments can affect total halo masses at levels up to ten percent. Improving the accuracy of the halo mass function calibration will therefore entail a suite of sophisticated gas dynamic simulations, not more or larger N-body simulations.

CHAPTER 6

Future Work and Conclusions

6.1 Introduction

In this chapter I discuss the prospects for future work with the Millennium Gas Simulations (MGS). I focus on expanding the work from Chapter 4 with the merger tree histories from the PH halos, which will provide an understanding on how halo mergers affect the observed X-ray and SZ signals. I also discuss the prospects for including galaxies in the covariance matrix, in preparation for future multiwaveband surveys.

6.2 Merger Trees and Covariance

In Chapter 4, I presented an empirical covariance matrix for the MGS. I will be extending this work to describing how halo evolution affects the multivariate statistics of a cluster sample. Understanding how the properties of merging halos compare to quiescent halos is important for understanding biases in the cluster sample selected by a survey. With over 4000 halos at redshift zero in the PH sample, I will be able to present the mean behavior of a merging cluster. A main goal of this work is to see if the evolution of an individual halo fills the covariance plane in an ergodic fashion.

6.2.1 Merger Tree Algorithm

I constructed the merger trees in two steps. First, for each halo at time t_1, I identified its unique direct descendent at time $t_1 + dt$. The direct descendent is determined by the halo membership of the majority of the mass at time $t_1 + dt$. Each halo at time t_1 has only one direct descendent, although halos at time $t_1 + dt$ may have more than

one ancestor. For instance, in the case of a merger between times t_1 and $t_1 + dt$, two halos at time t_1 will have the same direct descendent at time $t_1 + dt$. Some halos at $t_1 + dt$ will not have any ancestors: these are generally halos which did not make the mass cut of $M > 5 \times 10^{13}\, h^{-1}\, \mathrm{M}_\odot$. As I am most concerned with the behavior of primary halos, I also do not track satellite halos throughout a merger as they pass through a larger halo and re-emerge.

Once I have done this at every timestep, I start with each halo at redshift zero and work backwards to construct the merger tree. In doing so, for a given halo I identify its ancestors, and I also identify its most massive progenitor (MMP) at each redshift. For all of my analysis, when I talk about the evolution of a halo, I am referring to the properties of its MMP at each redshift. I identify merger events as happening between two timesteps when the number of ancestors of a given halo increases.

6.2.2 Halo Evolution During Merger Events

I will be presenting the evolution of halo properties during mergers, specifically temperature T, luminosity L, and Sunyaev-Zeldovich signal Y. I intend to measure the lag time between the increase in halo mass due to a merger, and increase in the X-ray and SZ signals. Furthermore, I would like to measure the duration of any temporary enhancement in the signals due to the merger. With the large number of halos in the `PH` simulation, I will also have statistics on the number of merger events as a function of redshift. Combining these results will contribute to an understanding of the source of the scatter in X-ray and SZ signals at fixed mass. I will also be able to predict the number of extreme outliers in a signal at fixed mass. For instance, after a merger the luminosity of a halo may be a $5-\sigma$ outlier from the median mass-luminosity relation. In a flux-limited survey, I will be able to identify what fraction of the high-luminosity halos are extreme outliers in luminosity given their mass. As the mass function is very steep, having these statistics will be important for measuring mass functions from cluster surveys.

6.2.3 Halo Evolution in the Covariance Plane

I also want to describe the behavior of a halo in the covariance plane. For a pair of signals x and y, I am defining the covariance plane as the $\delta_x - \delta_y$ plane. In this case, δ_x is the normalized deviation of signal x from the median mass-signal relationship: $\delta_x = \frac{x_i - \bar{x}}{\sigma_x}$. When tracking the evolution of a halo in the covariance plane, I will be tracking its most massive progenitor at each redshift, and calculating the deviation δ_x with respect to the median mass-signal relationship at that redshift. Figure 6.1 plots the evolution of a quiescent halo in the $\delta_L - \delta_T$ plane. Figure 6.1 also plots an ellipse representing the correlation coefficient as derived in Chapter 4. Movement in the $\delta_L - \delta_T$ plane parallel to the semi-major axis of this ellipse is analogous to the halo moving along the spine of the $L - T$ relation. Meanwhile, Figure 6.2 plots the evolution in the $\delta_L - \delta_T$ plane as it experiences infall from satellite halos.

I will also quantify how the evolutionary tracks of halos in a covariance plane match the full redshift zero population in the covariance plane. To demonstrate, I randomly selected 20 halos and plotted their MMPs in the $\delta_L - \delta_T$ plane at each redshift from formation until redshift zero. This is shown in figure 6.3, which also plots the ellipse corresponding to the redshift zero correlation coefficient between L and T as found in Chapter 4.

6.3 Extending the Covariance Matrix

In Chapter 4, I presented the covariance matrix for X-ray and SZ signals at fixed mass. As many multiwaveband surveys include optical data, the number of galaxies ($N_{\rm gal}$) at fixed mass is an important statistic to add to the covariance matrix. Including galaxy formation in a simulation on the scale of the MGS is not computationally feasible at this time. We must rely on semi-analytic models which predict $N_{\rm gal}$ in a halo given variables such as the halo mass, halo merger history, and local halo density.

A significant amount of work has characterized optically-detected galaxy clusters by the number of galaxies $N_{\rm gal}$ over some key luminosity $L_\star$. Becker et al. (2007) used the maxBCG cluster catalog from the Sloan Digital Sky Survey (SDSS) to measure the

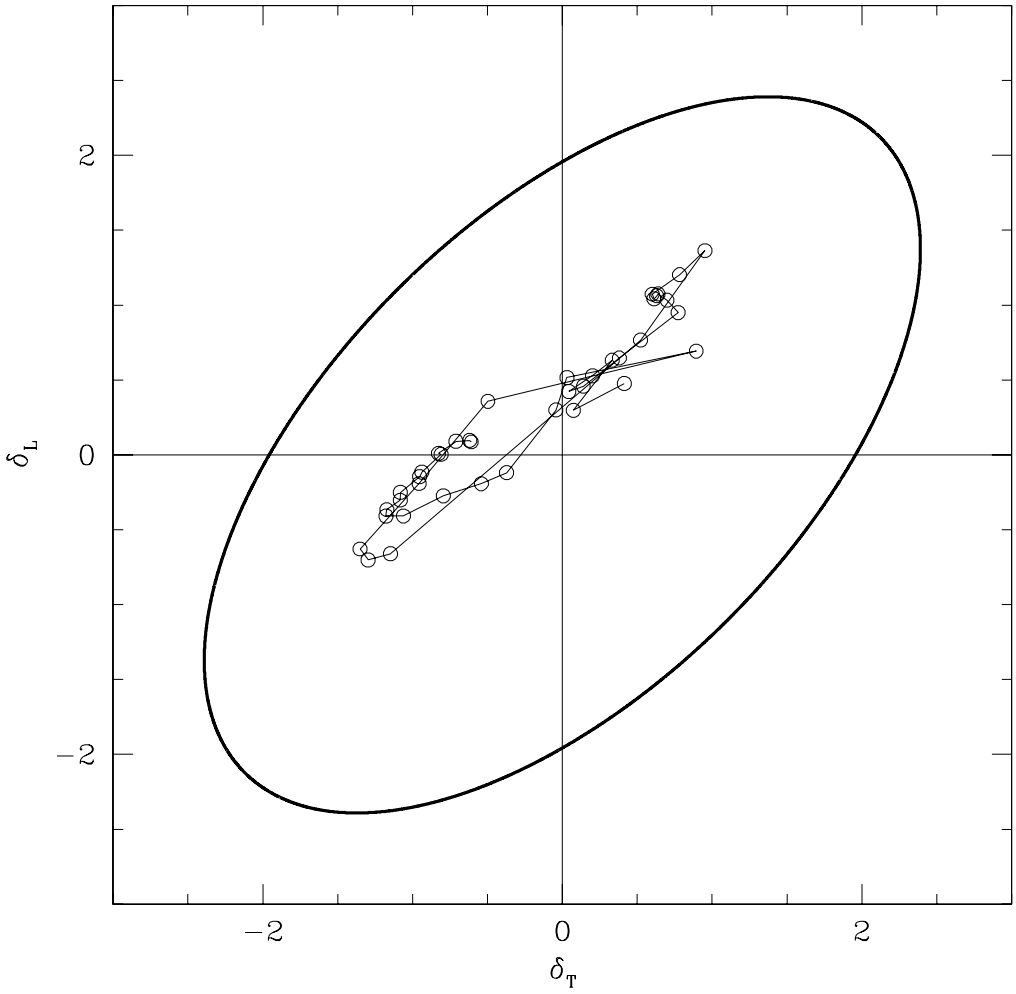

Figure 6.1. Evolution of a quiescent halo in the $\delta_L - \delta_T$ plane, from formation to the present. The ellipse denotes the correlation coefficient from Chapter 4.

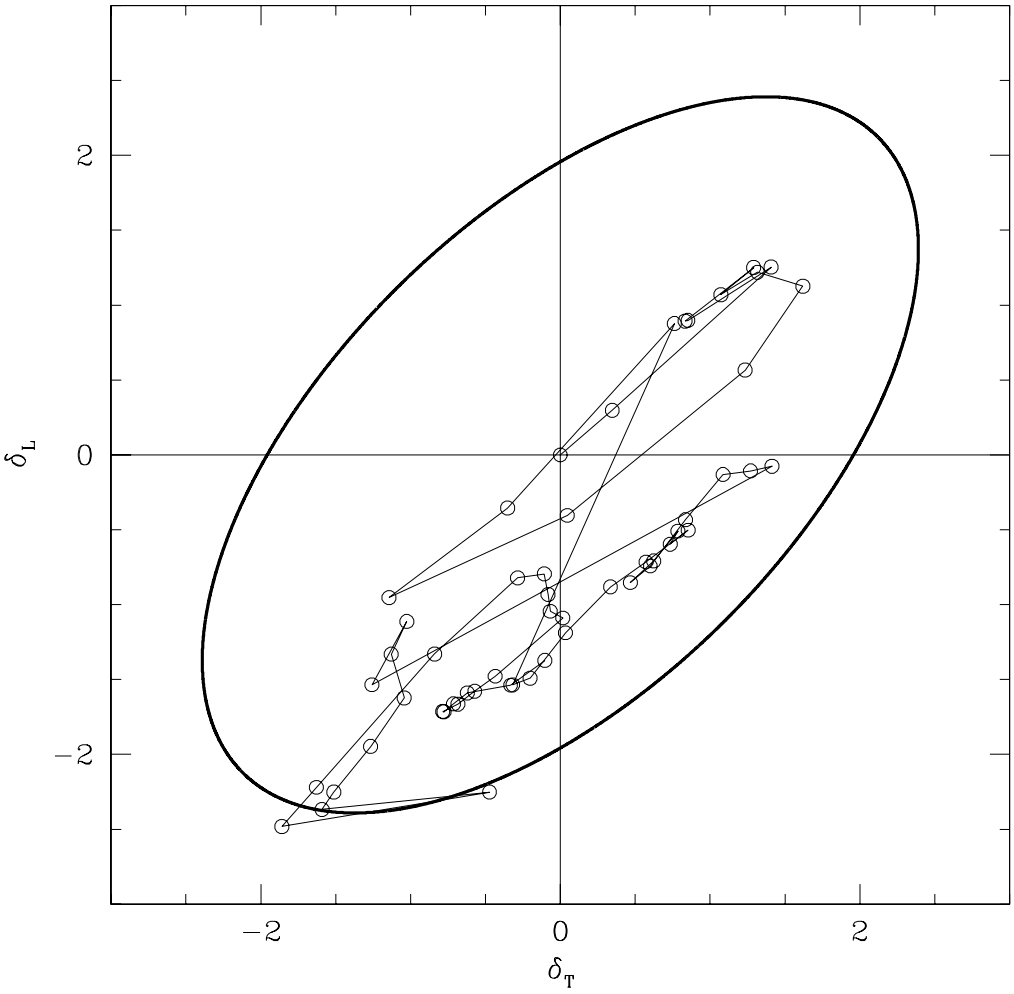

Figure 6.2. Evolution of a halo with satellite infall in the $\delta_L - \delta_T$ plane, from formation to the present. The ellipse denotes the correlation coefficient from Chapter 4.

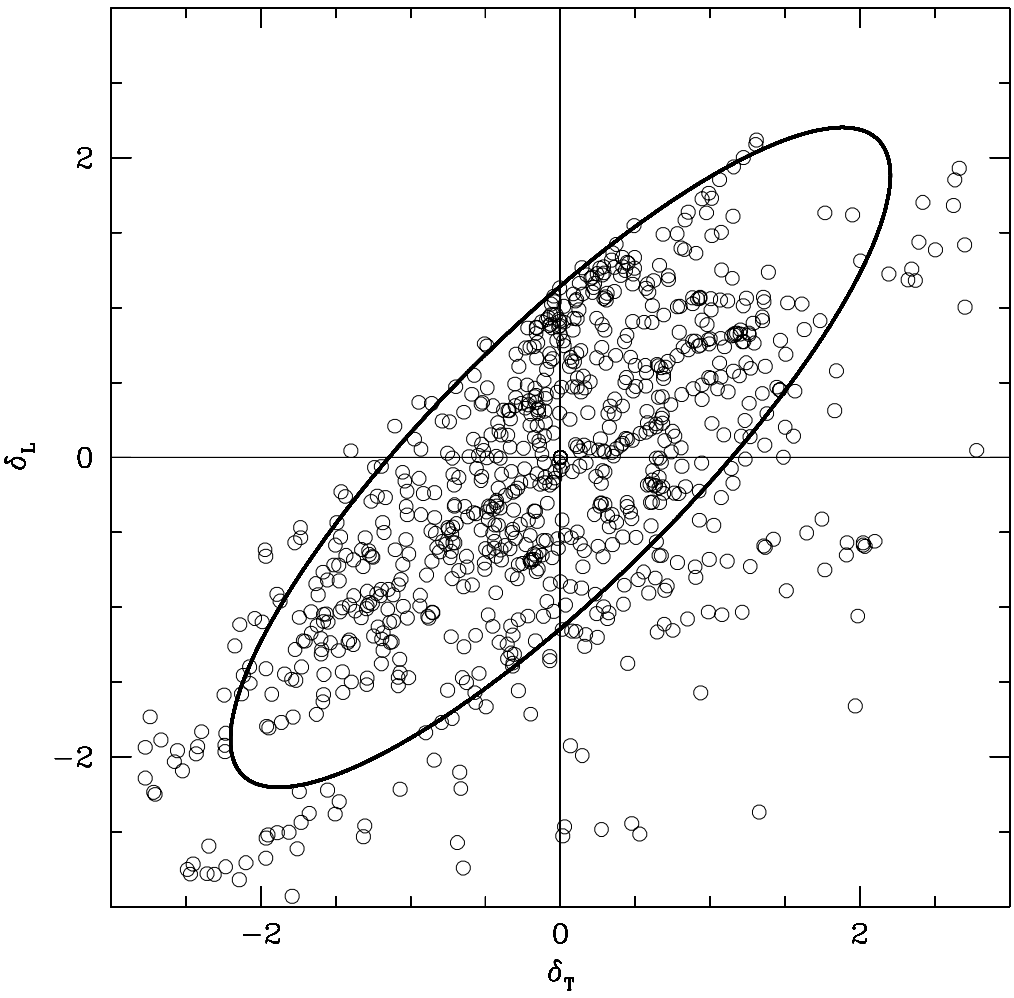

Figure 6.3. Positions in the $\delta_L - \delta_T$ plane for 20 halos over their lifetimes, with the ellipse marking the redshift correlation coefficient.

relationship between galaxy velocity dispersion and $N_{\rm gal}$. Galaxy velocity dispersion may be a good proxy for the dark matter velocity dispersion, which is a very low-scatter proxy for cluster mass (Evrard et al., 2008). At the high mass end, Becker et al. (2007) found that the scatter in the relationship was as low as $\sim 14\%$. Johnston et al. (2007) and Sheldon et al. (2007) used the SDSS data to directly measure the relationship between cluster mass and $N_{\rm gal}$. From this, Rykoff et al. (2008b) used the maxBCG cluster catalog from SDSS in conjunction with data from the ROSAT All Sky Survey to measure the relation between $N_{\rm gal}$ and X-ray luminosity. Although the $L_X - N_{\rm gal}$ relation was described by a simple power law, there was significant scatter, $\sigma_{\ln L_X} = 0.86 \pm 0.03$ at fixed $N_{\rm gal}$. Understanding the source of this large scatter, as well as the covariance between L_X and $N_{\rm gal}$ at fixed mass, is necessary for calibrating the mass selection function from future multiwaveband cluster surveys such as the Dark Energy Survey (DES).

As the dynamic range for cosmological simulations that resolve individual galaxies is prohibitively large, semi-analytic models must be used for inserting galaxies in large simulations. Semi-analytic models predict the galaxy population based on the mass and formation history of the host halo (Zentner et al., 2005; Wechsler et al., 2001). Springel et al. (2005) combine semi-analytic models with the halo formation histories of the Millennium Simulation. With this combination, Springel et al. (2005) present statistics on quasars and black holes in a volume matching that of the Millennium Simulation. Lemson & Virgo Consortium (2006) published a full catalog of galaxies from this semi-analytic modeling in the Millennium Simulation. With this catalog, Cohn et al. (2007) used a Red Cluster Sequence cluster-finding algorithm (Gladders & Yee, 2005b) to mimic observational results for a similar volume. The next step will then be to include these optical catalogs – both the intrinsic catalog from Lemson & Virgo Consortium (2006) and the projected catalog from Cohn et al. (2007) – into the multivariate analysis from Chapter 4. Including the galaxies will improve projected results from future multiwaveband surveys which include optical data.

6.4 Conclusion

In this thesis I have presented work which advances the use of galaxy clusters as cosmological probes. In Chapter 3, I combined observed cluster counts with predicted halo counts to derive the statistical relationship between cluster mass and X-ray luminosity. Halo counts alone did not uniquely constrain the three model parameters, but additional information from the observed luminosity-temperature relationship improved the constraints. For a WMAP3 cosmology (Spergel et al., 2006), I presented a measure of the log-normal scatter in mass at fixed luminosity: $\sigma_{\ln M} = 0.21 \pm 0.06$. With a measure of the scatter in the $L - M$ relation, I calibrated the bias in the observed population if the Malmquist bias due to the scatter is ignored. This bias is significant, on the order of $\sim 30\%$, and depends strongly on the degree of scatter in the $L - M$ relation. When comparing to observations of local clusters (Reiprich & Böhringer, 2002), this bias must be considered, as must the bias in hydrostatic mass estimates (Rasia et al., 2006). The uncertainties in both bias effects is the major limitation in calibrating the $L - M$ relation from X-ray observations. Independent calibration in the $L-M$ relation from gravitational lensing measurements will improve these uncertainties.

In Chapter 4 I presented statistical properties of halos from the pair of MGS: a `GO` model and a `PH` model. The `PH` model does not directly simulate the effects of AGN, star formation, and supernovae, but the effects of the heating from these astrophysical properties. In comparing the `GO` and `PH` models, I show how the preheating causes deviations from a scenario where only gravity and shock heating affect the gas. Comparing the `PH` model to observations can then place constraints on how much energy astrophysical properties must inject into the intracluster medium (ICM). I show that the `PH` model matches observations of cluster luminosity, temperature, and baryon fraction quite well, especially outside the core of the observed clusters. With the large volume of the MGS, I presented statistically significant multivariate scaling relations, including the mean relations and the second moment of the relations. In presenting the covariance matrix of the SZ and X-ray signals, I discussed the stability of these

signals and their evolution to the underlying cluster physics. Finally, I discussed the implications of the covariance measures for future cluster surveys, particularly how covariance can be a tool for reducing the scatter in mass of multiwaveband surveys.

Computer simulations of dark matter produce halo mass functions which agree at the $\sim 5\%$ level (Tinker et al., 2008). With this level of consistency, the additional bias due to baryonic physics must be considered. In Chapter 5 I used two extreme treatments of the gas physics to investigate the possible range of bias from baryonic physics. One treatment was the `PH` model from the MGS, which has a strong blast of preheating at redshift $z = 4$. The result of this preheating is to heat the gas and reduce the baryon fraction of the halos. The other treatment was the `CSF` model from the ART simulation by Rudd et al. (2008). The `CSF` model included the effects of AGN activity, star formation, and supernovae. Due to the excessive amount of star formation in the `CSF` model, nearly half of the baryons in the halos were in stars, and the total baryon fraction of the halos was enhanced with respect to the mean baryon fraction of the universe. However, while the two models had different baryon fractions, they had very similar hot gas fractions, and thus both approximately matched the observed $L - T$ relation. With a large sample of halos, at fixed number density I measured the mean mass offset from the `GO` models, and found $\Delta M = -15 \pm 1$ percent for the `PH` model, and $\Delta M = +16 \pm 2$ percent for the `CSF` model. These mean mass offsets lead to deviations on the order of $\sim 30\%$ in number density from the Tinker function. While these cases are likely extreme, they are significantly larger than the 5% statistical uncertainty in the Tinker function. Improved observational constraints on the baryon census, and simulations which match the observed star formation rate, are needed to produce a theoretically calibrated halo mass function which includes baryons.

The work in this thesis has contributed to the possibilities of "precision cosmology", and future work with the MGS simulations will expand our understanding of cluster physics.

APPENDIX

APPENDIX A

Degeneracy in Power-Law Normalization and Scatter

Consider the case of a power-law mass function at some epoch

$$n(M)\, d\ln M \;=\; n_{15}\; M^{-\gamma}\, d\ln M, \tag{A.1}$$

where M is halo mass in units of $10^{15}\; h^{-1}\; \mathrm{M}_{\odot}$ and n_{15} is the space density at that mass. We show here that convolving the mass function with a log-normal kernel of the form, equation (3.8), has an effect that is degenerate in normalization and scatter.

For compactness, let $x = \ln M$, $y = \ln L$, $a = \ln L_{15}$, then $\bar{y}(x) = a + p\, x$ and the mass associated with a luminosity y is $\hat{x}(y) = (y - a)/p$. The luminosity function is the convolution

$$n(y)\, dy \;= \int dx\, n(x)\, p(y|x)\, dy, \tag{A.2}$$

with the kernel a Gaussian of fixed width $\sigma_{\ln L}$

$$p(y|x)\, dy \;=\; \frac{1}{\sqrt{2\pi}\sigma_{\ln L}}\; \exp\left(-(y - \bar{y}(x))^2 / 2{\sigma_{\ln L}}^2\right) dy. \tag{A.3}$$

Linearly transforming the kernel, and using $\sigma_{\ln M} = \sigma_{\ln L}/p$, the luminosity function is

$$n(y)\, dy \;=\; \frac{n_{15}}{\sqrt{2\pi}\, p\, \sigma_{\ln M}} \int dx \exp\left(-\gamma x - (x - \hat{x})^2 / 2{\sigma_{\ln M}}^2\right) dy \tag{A.4}$$

Completing the square leads to the result

$$n(y)\, dy \;=\; \frac{n_{15}}{p} \exp\left(-\gamma/p[y - (a + \gamma p {\sigma_{\ln M}}^2/2)]\right) dy \tag{A.5}$$

which in original notation is

$$n(L)\ d\ln L \ = \ \frac{n_{15}}{p}\ (L/\tilde{L}_{15})^{-\gamma/p}\ d\ln L. \tag{A.6}$$

The result is a power-law with slope $-\gamma/p$ and with intercept

$$\ln \tilde{L}_{15} \ = \ \ln L_{15} \ + \ \gamma\, p\, {\sigma_{\ln M}}^2/2. \tag{A.7}$$

Since $\tilde{L}_{15}$ is the measurable quantity (call it C), then the observed luminosity function constrains the combination of intercept and scatter

$$\ln L_{15} = C - \frac{\gamma\, p\, {\sigma_{\ln M}}^2}{2} \tag{A.8}$$

For values of $\gamma = 3.1$, the local slope of the mass function at $10^{15}\ h^{-1}\ \mathrm{M}_\odot$ for a concordance model, and $p = 1.6$, this expectation is shown as the bold line in the lower right panel of Figure 3.2.

BIBLIOGRAPHY

BIBLIOGRAPHY

Abell, G. O. 1958, ApJS, 3, 211

Alpher, R. A., Bethe, H., & Gamow, G. 1948, Physical Review, 73, 803

Arnaud, M. & Evrard, A. E. 1999, MNRAS, 305, 631

Arnaud, M., Pointecouteau, E., & Pratt, G. W. 2007, A&A, 474, L37

Böhringer, H., et al. 2002, ApJ, 566, 93

Böhringer, H., et al. 2004, A&A, 425, 367

Böhringer, H., et al. 2001, A&A, 369, 826

Bahcall, N. A., Cen, R., Davé, R., Ostriker, J. P., & Yu, Q. 2000, ApJ, 541, 1

Bahcall, N. A., et al. 2003, ApJS, 148, 243

Barnes, J. & Hut, P. 1986, Nature, 324, 446

Bartelmann, M. & Steinmetz, M. 1996, MNRAS, 283, 431

Bartlett, J. G., Chamballu, A., Melin, J.-B., Arnaud, M., & Members of the Planck Working Group 5. 2008, Astronomische Nachrichten, 329, 147

Battye, R. A. & Weller, J. 2003a, Phys. Rev. D, 68, 083506

Battye, R. A. & Weller, J. 2003b, Phys. Rev. D, 68, 083506

Becker, M. R., et al. 2007, ArXiv e-prints, 704

Bialek, J. & Evrard, A. E. 2006, in prep

Bialek, J. J., Evrard, A. E., & Mohr, J. J. 2001, ApJ, 555, 597

Bonamente, M., Joy, M., LaRoque, S. J., Carlstrom, J. E., Nagai, D., & Marrone, D. P. 2008, ApJ, 675, 106

Bond, J. R., Cole, S., Efstathiou, G., & Kaiser, N. 1991, ApJ, 379, 440

Borgani, S., et al. 2006, MNRAS, 367, 1641

Borgani, S., Governato, F., Wadsley, J., Menci, N., Tozzi, P., Lake, G., Quinn, T., & Stadel, J. 2001, ApJ, 559, L71

Borgani, S., Murante, G., Springel, V., Diaferio, A., Dolag, K., Moscardini, L., Tormen, G., Tornatore, L., & Tozzi, P. 2004, MNRAS, 348, 1078

Bryan, G. L. & Norman, M. L. 1998, ApJ, 495, 80

Busha, M. T., Evrard, A. E., & Adams, F. C. 2007, ApJ, 665, 1

Carlberg, R. G., Yee, H. K. C., & Ellingson, E. 1997, ApJ, 478, 462

Carlstrom, J. 2004, in Proceedings of the 22nd Texas Symposium on Relativistic Astrophysics at Stanford. Stanford California, December 13-17, 2004. ditors: Pisin Chen, Elliott Bloom, Greg Madejski (SLAC), Vahe Patrosian (Stanford University)., p.24, ed. P. Chen, E. Bloom, G. Madejski, & V. Patrosian, 24–+

Carlstrom, J. E., Holder, G. P., & Reese, E. D. 2002, ARA&A, 40, 643

Cavaliere, A. & Fusco-Femiano, R. 1976, A&A, 49, 137

Clowe, D., Bradač, M., Gonzalez, A. H., Markevitch, M., Randall, S. W., Jones, C., & Zaritsky, D. 2006, ApJ, 648, L109

Cohn, J. D., Evrard, A. E., White, M., Croton, D., & Ellingson, E. 2007, MNRAS, 382, 1738

Cole, S., et al. 2005, submitted, astro-ph/0501174

Couchman, H. M. P. 1991, ApJ, 368, L23

Crain, R. A., Eke, V. R., Frenk, C. S., Jenkins, A., McCarthy, I. G., Navarro, J. F., & Pearce, F. R. 2007, MNRAS, 377, 41

Crommelin, A. C. D. 1918, JRASC, 12, 33

Cunha, C. 2008, ArXiv e-prints

Cunha, C. 2009, Phys. Rev. D, 79, 063009

Cunha, C., Huterer, D., & Frieman, J. A. 2009, ArXiv e-prints

de Putter, R. & White, M. 2005, New Astronomy, 10, 676

Del Popolo, A., Hiotelis, N., & Peñarrubia, J. 2005, ApJ, 628, 76

Dolag, K., Vazza, F., Brunetti, G., & Tormen, G. 2005, MNRAS, 364, 753

Donahue, M., Voit, G. M., Gioia, I., Lupino, G., Hughes, J. P., & Stocke, J. T. 1998, ApJ, 502, 550

Ebeling, H., Voges, W., Bohringer, H., & Edge, A. C. 1993, A&A, 275, 360

Efstathiou, G. & Eastwood, J. W. 1981, MNRAS, 194, 503

Efstathiou, G., Sutherland, W. J., & Maddox, S. J. 1990, Nature, 348, 705

Eisenhardt, P. R. M., et al. 2008, ArXiv e-prints, 804

Eisenstein, D. J., et al. 2005, ApJ, 633, 560

Ettori, S., Dolag, K., Borgani, S., & Murante, G. 2006, MNRAS, 365, 1021

Ettori, S., Tozzi, P., Borgani, S., & Rosati, P. 2004, A&A, 417, 13

Evrard, A. E. 1990, ApJ, 363, 349

Evrard, A. E. 2004, in Carnegie Observatories Astrophysics Series, Vol. 3: Clusters of Galaxies: Probes of Cosmological Structure and Galaxy Evolution, ed. J. S. Mulchaey, A. Dressler, and A. Oemler (Cambridge: Cambridge Univ. Press)

Evrard, A. E., et al. 2008, ApJ, 672, 122

Evrard, A. E. & Henry, J. P. 1991, ApJ, 383, 95

Evrard, A. E., et al. 2002, ApJ, 573, 7

Evrard, A. E., Metzler, C. A., & Navarro, J. F. 1996, ApJ, 469, 494

Fabian, A. C., Sanders, J. S., Taylor, G. B., Allen, S. W., Crawford, C. S., Johnstone, R. M., & Iwasawa, K. 2006, MNRAS, 366, 417

Fairley, B. W., Jones, L. R., Scharf, C., Ebeling, H., Perlman, E., Horner, D., Wegner, G., & Malkan, M. 2000, MNRAS, 315, 669

Fan, X., et al. 2006, AJ, 132, 117

Frenk, C. S., et al. 1999, ApJ, 525, 554

Gao, L., Navarro, J. F., Cole, S., Frenk, C. S., White, S. D. M., Springel, V., Jenkins, A., & Neto, A. F. 2008, MNRAS, 387, 536

Gingold, R. A. & Monaghan, J. J. 1977, MNRAS, 181, 375

Gladders, M. D. & Yee, H. K. C. 2005a, ApJS, 157, 1

Gladders, M. D. & Yee, H. K. C. 2005b, ApJS, 157, 1

Gnedin, O. Y., Kravtsov, A. V., Klypin, A. A., & Nagai, D. 2004, ApJ, 616, 16

Gonzalez, A. H., Zaritsky, D., & Zabludoff, A. I. 2007, ApJ, 666, 147

Gorenstein, P., Fabricant, D., Topka, K., Harnden, F. R., & Tucker, W. H. 1978, ApJ, 224, 718

Gottlöber, S. & Yepes, G. 2007, ApJ, 664, 117

Haiman, Z., Mohr, J. J., & Holder, G. P. 2001, ApJ, 553, 545

Hallman, E. J., Motl, P. M., Burns, J. O., & Norman, M. L. 2006, ApJ, 648, 852

Hartley, W. G., Gazzola, L., Pearce, F. R., Kay, S. T., & Thomas, P. A. 2008, MNRAS, 519

Heitmann, K., Ricker, P. M., Warren, M. S., & Habib, S. 2005, ApJS, 160, 28

Hennawi, J. F. & Spergel, D. N. 2005, ApJ, 624, 59

Henry, J. P. 2004, ApJ, 609, 603

Hernquist, L. 1987, ApJS, 64, 715

Herschel, W. 1785, Royal Society of London Philosophical Transactions Series I, 75, 213

Hilton, M., et al. 2009, ArXiv e-prints

Hoekstra, H. 2003, MNRAS, 339, 1155

Holder, G., Haiman, Z., & Mohr, J. J. 2001, ApJ, 560, L111

Holder, G. P., Mohr, J. J., Carlstrom, J. E., Evrard, A. E., & Leitch, E. M. 2000, ApJ, 544, 629

Holmberg, E. 1941, ApJ, 94, 385

Horner, D. J. 2001, PhD thesis, University of Maryland, College Park

Hu, W. & Kravtsov, A. V. 2003a, ApJ, 584, 702

Hu, W. & Kravtsov, A. V. 2003b, ApJ, 584, 702

Hubble, E. 1929, Proceedings of the National Academy of Science, 15, 168

Hubble, E. P. 1925, The Observatory, 48, 139

Huterer, D. & Takada, M. 2005, Astroparticle Physics, 23, 369

Ikebe, Y., Reiprich, T. H., Böhringer, H., Tanaka, Y., & Kitayama, T. 2002, A&A, 383, 773

Jeltema, T. E., Hallman, E. J., Burns, J. O., & Motl, P. M. 2008, ApJ, 681, 167

Jenkins, A., Frenk, C. S., White, S. D. M., Colberg, J. M., Cole, S., Evrard, A. E., Couchman, H. M. P., & Yoshida, N. 2001, MNRAS, 321, 372

Jing, Y. P., Zhang, P., Lin, W. P., Gao, L., & Springel, V. 2006, ApJ, 640, L119

Johnston, D. E., et al. 2007, ArXiv e-prints

Johnston, D. E. *et al.*. 2005, MNRAS, in press, astro-ph/0503282

Jurić, M., et al. 2008, ApJ, 673, 864

Kaiser, N. 1986, MNRAS, 222, 323

Kaiser, N. 1991, ApJ, 383, 104

Kay, S. T., da Silva, A. C., Aghanim, N., Blanchard, A., Liddle, A. R., Puget, J.-L., Sadat, R., & Thomas, P. A. 2007, MNRAS, 377, 317

Koester, B. *et al.*. 2006, in prep.

Koester, B. P., et al. 2007a, ApJ, 660, 239

Koester, B. P., McKay, T. A., Annis, J., Wechsler, R. H., Evrard, A. E., Rozo, E., Bleem, L., Sheldon, E. S., & Johnston, D. 2007b, ApJ, 660, 221

Koester, B. P., McKay, T. A., Annis, J., Wechsler, R. H., Evrard, A. E., Rozo, E., Bleem, L., Sheldon, E. S., & Johnston, D. 2007c, ApJ, 660, 221

Kosowsky, A. 2003, New Astronomy Review, 47, 939

Kravtsov, A. V., Klypin, A. A., & Khokhlov, A. M. 1997, ApJS, 111, 73

Kravtsov, A. V., Nagai, D., & Vikhlinin, A. A. 2005, ApJ, 625, 588

Kravtsov, A. V., Vikhlinin, A., & Nagai, D. 2006, ApJ, 650, 128

Lange, A., et al. 1995, Space Science Reviews, 74, 145

Lange, A. E., et al. 2001, Phys. Rev. D, 63, 042001

Lemson, G. & Virgo Consortium, t. 2006, ArXiv Astrophysics e-prints

Levine, E. S., Schulz, A. E., & White, M. 2002, ApJ, 577, 569

Lima, M. & Hu, W. 2004a, Phys. Rev. D, 70, 043504

Lima, M. & Hu, W. 2004b, Phys. Rev. D, 70, 043504

Lima, M. & Hu, W. 2005a, Phys. Rev. D, 72, 043006

Lima, M. & Hu, W. 2005b, Phys. Rev. D, 72, 043006

Lin, Y.-T., Mohr, J. J., & Stanford, S. A. 2003, ApJ, 591, 749

Loh, M., et al. 2005, American Astronomical Society Meeting Abstracts, 207,

Majumdar, S. & Mohr, J. J. 2003, ApJ, 585, 603

Malte Schäfer, B. & Bartelmann, M. 2007, MNRAS, 377, 253

Mathiesen, B. F. & Evrard, A. E. 2001a, ApJ, 546, 100

Mathiesen, B. F. & Evrard, A. E. 2001b, ApJ, 546, 100

Maughan, B., Jones, L., Ebeling, H., & Scharf, C. 2005, MNRAS, in press, astro-ph/0503455

Maughan, B. J. 2007, ArXiv Astrophysics e-prints

Maughan, B. J., Jones, L. R., Ebeling, H., & Scharf, C. 2006, MNRAS, 365, 509

Mazzotta, P., Edge, A. C., & Markevitch, M. 2003, ApJ, 596, 190

Mazzotta, P., Rasia, E., Moscardini, L., & Tormen, G. 2004, MNRAS, 354, 10

McCarthy, I. G., Bower, R. G., & Balogh, M. L. 2007, MNRAS, 377, 1457

Metzler, C. A., White, M., & Loken, C. 2001, ApJ, 547, 560

Miller, C. J., et al. 2005, AJ, 130, 968

Mitchell, N. L., McCarthy, I. G., Bower, R. G., Theuns, T., & Crain, R. A. 2008, ArXiv e-prints

Mohr, J. J., Mathiesen, B., & Evrard, A. E. 1999, ApJ, 517, 627

Monaghan, J. J. 1992, ARA&A, 30, 543

Mullis, C. R., Rosati, P., Lamer, G., Böhringer, H., Schwope, A., Schuecker, P., & Fassbender, R. 2005, ApJ, 623, L85

Mushotzky, R. F. & Scharf, C. A. 1997, ApJ, 482, L13+

Nagai, D. 2006, ApJ, 650, 538

Nagai, D., Vikhlinin, A., & Kravtsov, A. V. 2007, ApJ, 655, 98

Navarro, J. F., Frenk, C. S., & White, S. D. M. 1995, MNRAS, 275, 56

Navarro, J. F., Frenk, C. S., & White, S. D. M. 1996, ApJ, 462, 563

Navarro, J. F., Frenk, C. S., & White, S. D. M. 1997, ApJ, 490, 493

Nord, B., Stanek, R., Rasia, E., & Evrard, A. E. 2008, MNRAS, 383, L10

Novicki, M. C., Sornig, M., & Henry, J. P. 2002, AJ, 124, 2413

O'Hara, T. B., Mohr, J. J., Bialek, J. J., & Evrard, A. E. 2006, ApJ, 639, 64

O'Hara, T. B., Mohr, J. J., & Sanderson, A. J. R. 2007, ArXiv e-prints

Osmond, J. P. F. & Ponman, T. J. 2004, MNRAS, 350, 1511

Padilla, N. D., et al. 2004, MNRAS, 352, 211

Peacock, J. A. 1999, Cosmological Physics, ed. J. A. Peacock

Pearce, F. *et al.*. 2007, in prep.

Pedersen, K. & Dahle, H. 2006, arXiv:astro-ph/0603260

Peebles, P. J. E. 1970, AJ, 75, 13

Peebles, P. J. E. 1996, in Astronomical Society of the Pacific Conference Series, Vol. 88, Clusters, Lensing, and the Future of the Universe, ed. V. Trimble & A. Reisenegger, 1–+

Pen, U.-L. 1999, ApJS, 120, 49

Penzias, A. A. & Wilson, R. W. 1965, ApJ, 142, 419

Pettini, M., Zych, B. J., Murphy, M. T., Lewis, A., & Steidel, C. C. 2008, MNRAS, 391, 1499

Pierpaoli, E., Borgani, S., Scott, D., & White, M. 2003, MNRAS, 342, 163

Pierpaoli, E., Scott, D., & White, M. 2001, MNRAS, 325, 77

Pierre, M., Boehringer, H., Ebeling, H., Voges, W., Schuecker, P., Cruddace, R., & MacGillivray, H. 1994, A&A, 290, 725

Pratt, G. W., Croston, J. H., Arnaud, M., & Boehringer, H. 2008, ArXiv e-prints

Press, W. H. & Schechter, P. 1974, ApJ, 187, 425

Puchwein, E., Sijacki, D., & Springel, V. 2008, ApJ, 687, L53

Rasia, E., Ettori, S., Moscardini, L., Mazzotta, P., Borgani, S., Dolag, K., Tormen, G., Cheng, L. M., & Diaferio, A. 2006, MNRAS, 369, 2013

Rasia, E., Tormen, G., & Moscardini, L. 2004, MNRAS, 351, 237

Reed, D., Gardner, J., Quinn, T., Stadel, J., Fardal, M., Lake, G., & Governato, F. 2003, MNRAS, 346, 565

Reiprich, T. H. 2006, arXiv:astro-ph/0605009

Reiprich, T. H. & Böhringer, H. 2002, ApJ, 567, 716

Ricker, P. M. & Sarazin, C. L. 2001, ApJ, 561, 621

Riess, A. G., et al. 1998, AJ, 116, 1009

Romer, A. K., et al. 2000, ApJS, 126, 209

Romer, A. K., Viana, P. T. P., Liddle, A. R., & Mann, R. G. 2001, ApJ, 547, 594

Rosati, P., della Ceca, R., Norman, C., & Giacconi, R. 1998, ApJ, 492, L21+

Rowley, D. R., Thomas, P. A., & Kay, S. T. 2004, MNRAS, 352, 508

Rozo, E., et al. 2009, ArXiv e-prints

Rubin, V. C. & Ford, W. K. J. 1970, ApJ, 159, 379

Rudd, D. H. 2007, PhD thesis, The University of Chicago

Rudd, D. H., Zentner, A. R., & Kravtsov, A. V. 2008, ApJ, 672, 19

Ruhl, J., et al. 2004, in Presented at the Society of Photo-Optical Instrumentation Engineers (SPIE) Conference, Vol. 5498, Millimeter and Submillimeter Detectors for Astronomy II. Edited by Jonas Zmuidzinas, Wayne S. Holland and Stafford Withington Proceedings of the SPIE, Volume 5498, pp. 11-29 (2004)., ed. C. M. Bradford, P. A. R. Ade, J. E. Aguirre, J. J. Bock, M. Dragovan, L. Duband, L. Earle, J. Glenn, H. Matsuhara, B. J. Naylor, H. T. Nguyen, M. Yun, & J. Zmuidzinas, 11–29

Rykoff, E. S., et al. 2008a, MNRAS, 387, L28

Rykoff, E. S., McKay, T. A., Becker, M. R., Evrard, A., Johnston, D. E., Koester, B. P., Rozo, E., Sheldon, E. S., & Wechsler, R. H. 2008b, ApJ, 675, 1106

Sahlén, M., et al. 2008, ArXiv e-prints, 802

Schindler, S. 1996, A&A, 305, 756

Schuecker, P., et al. 2001, A&A, 368, 86

Schuecker, P., Böhringer, H., Collins, C. A., & Guzzo, L. 2003, A&A, 398, 867

Schwan, D., et al. 2003, New Astronomy Review, 47, 933

Sehgal, N., Trac, H., Huffenberger, K., & Bode, P. 2007, ApJ, 664, 149

Seljak, U. & Zaldarriaga, M. 1996, ApJ, 469, 437

Shapley, H. 1933, Proceedings of the National Academy of Science, 19, 591

Sheldon, E. S., et al. 2004, AJ, 127, 2544

Sheldon, E. S., et al. 2007, ArXiv e-prints

Sheth, R. K. & Tormen, G. 1999a, MNRAS, 308, 119

Sheth, R. K. & Tormen, G. 1999b, MNRAS, 308, 119

Sijacki, D., Pfrommer, C., Springel, V., & Enßlin, T. A. 2008, MNRAS, 387, 1403

Smoot, G. F., et al. 1992, ApJ, 396, L1

Spergel, D. N., et al. 2006, arXiv:astro-ph/0603449

Spergel, D. N., et al. 2003, ApJS, 148, 175

Springel, V. 2005a, MNRAS, 364, 1105

Springel, V. 2005b, MNRAS, 364, 1105

Springel, V., et al. 2005, Nature, 435, 629

Stanek, R., Evrard, A. E., Böhringer, H., Schuecker, P., & Nord, B. 2006, ApJ, 648, 956

Stanek, R., Rudd, D., & Evrard, A. E. 2009, MNRAS, L172+

Stanford, S. A., et al. 2005, ApJ, 634, L129

Stanford, S. A., et al. 2006, ApJ, 646, L13

Suginohara, T., Suto, Y., Bouchet, F. R., & Hernquist, L. 1991, ApJS, 75, 631

Sunyaev, R. A. & Zeldovich, Y. B. 1970, Comments on Astrophysics and Space Physics, 2, 66

Sunyaev, R. A. & Zeldovich, Y. B. 1972, Comments on Astrophysics and Space Physics, 4, 173

Sutherland, R. S. & Dopita, M. A. 1993, ApJS, 88, 253

Tasker, E. J., Brunino, R., Mitchell, N. L., Michielsen, D., Hopton, S., Pearce, F. R., Bryan, G. L., & Theuns, T. 2008, MNRAS, 390, 1267

Tauber, J. A. 2004, Advances in Space Research, 34, 491

Thomas, P. A. 1997, in Astronomical Society of the Pacific Conference Series, Vol. 115, Galactic Cluster Cooling Flows, ed. N. Soker, 202–+

Tinker, J. L., Kravtsov, A. V., Klypin, A., Abazajian, K., Warren, M. S., Yepes, G., Gottlober, S., & Holz, D. E. 2008, ArXiv e-prints, 803

Truelove, J. K., Klein, R. I., McKee, C. F., Holliman, J. H., Howell, L. H., Greenough, J. A., & Woods, D. T. 1998, ApJ, 495, 821

Trümper, J. 1984, MPE Rep., No. 184, p. 254 - 260, 184, 254

Vikhlinin, A. 2006, ApJ, 640, 710

Vikhlinin, A., et al. 2008, ArXiv e-prints, 805

Vikhlinin, A., et al. 2009, ApJ, 692, 1060

Vikhlinin, A., Markevitch, M., Murray, S. S., Jones, C., Forman, W., & Van Speybroeck, L. 2005, ApJ, 628, 655

Voit, G. M., Balogh, M. L., Bower, R. G., Lacey, C. G., & Bryan, G. L. 2003, ApJ, 593, 272

Wang, L. & Steinhardt, P. J. 1998, ApJ, 508, 483

Wang, S., Khoury, J., Haiman, Z., & May, M. 2004, Phys. Rev. D, 70, 123008

Warren, M. S., Abazajian, K., Holz, D. E., & Teodoro, L. 2005, arXiv:astro-ph/0506395

Warren, M. S., Abazajian, K., Holz, D. E., & Teodoro, L. 2006, ApJ, 646, 881

Warren, M. S., Quinn, P. J., Salmon, J. K., & Zurek, W. H. 1992, ApJ, 399, 405

Wechsler, R. H., Bullock, J. S., Primack, J. R., Kravtsov, A. V., & Dekel, A. 2002, ApJ, 568, 52

Wechsler, R. H., Somerville, R. S., Bullock, J. S., Kolatt, T. S., Primack, J. R., Blumenthal, G. R., & Dekel, A. 2001, ApJ, 554, 85

Weiner, B. J., et al. 2008, ArXiv e-prints, 804

White, M., Hernquist, L., & Springel, V. 2002, ApJ, 579, 16

White, S. D. M., Navarro, J. F., Evrard, A. E., & Frenk, C. S. 1993, Nature, 366, 429

White, S. D. M. & Rees, M. J. 1978, MNRAS, 183, 341

Xu, G. 1995, ApJS, 98, 355

Yepes, G., Sevilla, R., Gottlöber, S., & Silk, J. 2007, ApJ, 666, L61

York, D. G., et al. 2000, AJ, 120, 1579

Younger, J. D., Haiman, Z., Bryan, G. L., & Wang, S. 2006, ApJ, 653, 27

Zentner, A. R., Berlind, A. A., Bullock, J. S., Kravtsov, A. V., & Wechsler, R. H. 2005, ApJ, 624, 505

Zhang, Y.-Y., Finoguenov, A., Böhringer, H., Kneib, J.-P., Smith, G. P., Kneissl, R., Okabe, N., & Dahle, H. 2008, A&A, 482, 451

Zwicky, F. 1937, ApJ, 86, 217